The 2nd International Congress on

3DMS

3D Materials Science 2014

L'Impérial Palace • Annecy, France • June 29–July 2

Congress Proceedings

EDITORS:
Dominique Bernard | Jean-Yves Buffière
Tresa Pollock | Henning Friis Poulsen
Anthony Rollett | Michael Uchic

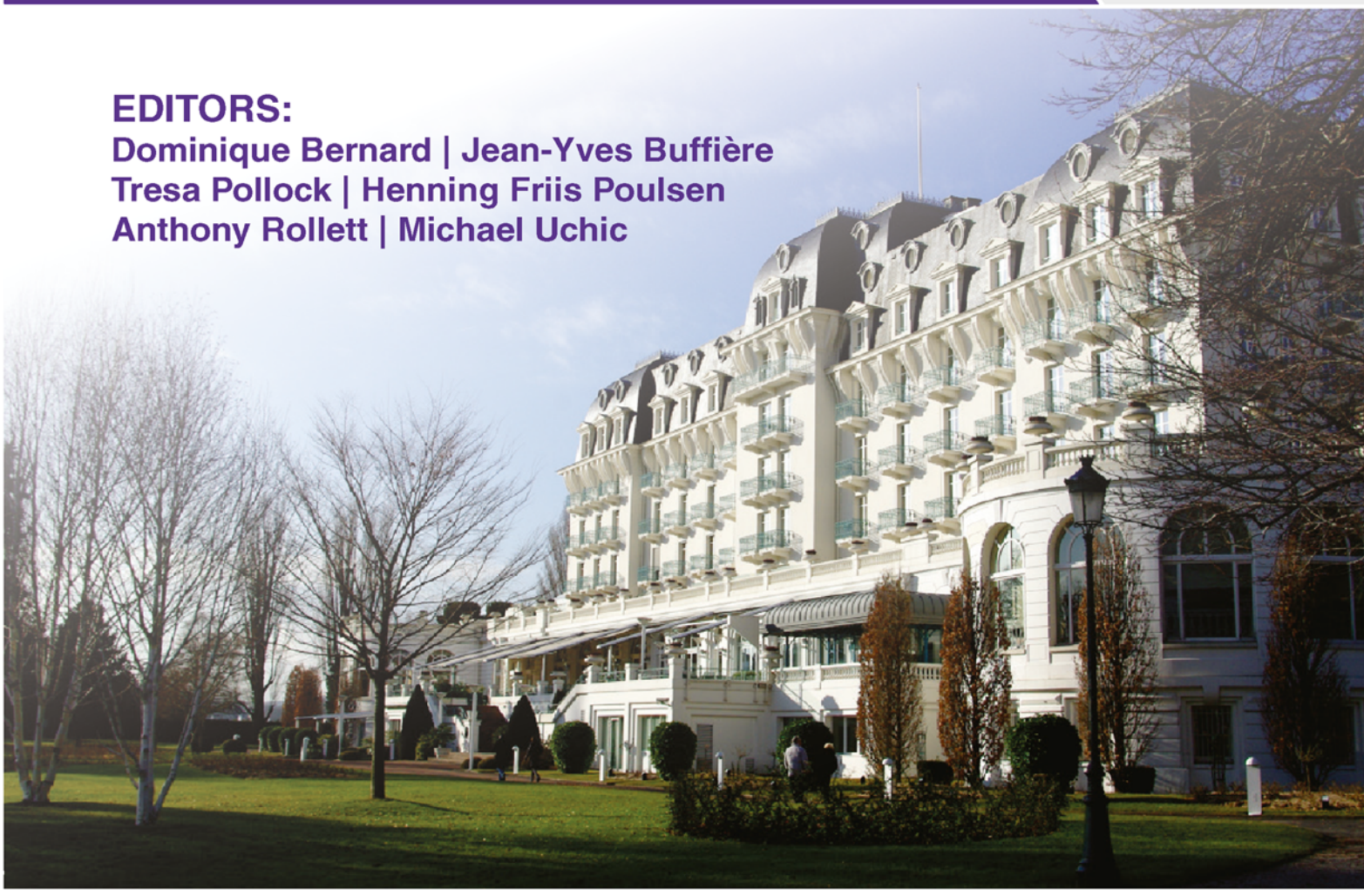

TMS

Springer

The 2nd International Congress on

3D Materials Science 2014

Proceedings of the

2nd International Congress on 3D Materials Science

Held

June 29–July 2, 2014

L'Impérial Palace | Annecy, France

Edited by

Dominique Bernard, Jean-Yves Buffière,
Tresa Pollock, Henning Friis Poulsen,
Anthony Rollett, Michael Uchic

Editors
Dominique Bernard
Jean-Yves Buffière
Tresa Pollock
Henning Friis Poulsen
Anthony Rollett
Michael Uchic

ISBN 978-3-319-48595-9
ISBN 978-3-319-48123-4 (eBook)
DOI 10.1007/978-3-319-48123-4

Chemistry and Materials Science: Professional

Published by Springer International Publishers, Switzerland, 2016
Reprint of the original edition published by John Wiley & Sons, Inc., 2014, 978-1-118-94545-2

Printed on acid-free paper

This Springer imprint is published by Springer Nature
The registered company is Springer International Publishing AG
The registered company address is: Gewerbestrasse 11, 6330 Cham, Switzerland

TABLE OF CONTENTS
2nd International Congress on 3D Materials Science 2014

Acquisition and Handling of 3D Data

Microstructure/Property Relationship in 3D: Characterization and Simulation

Microstructure/Property Relationship in 3D: Deformation and Damage

New Experimental Techniques

Analysis at the Nanoscale

Dynamic Processes

PREFACE

This is a collection of manuscripts presented at the 2nd International Congress on 3D Materials Science, a conference organized by The Minerals, Metals & Materials Society (TMS), the Advanced Characterization, Testing and Simulation Committee, and the six congress organizers, and held in Annecy, France, on June 29–July 2, 2014.

Building on the great success of the first event in 2012, the 2nd Congress on 3D Materials Science convened researchers and engineers to assess the state-of-the-art in 3D materials science and determine paths to further the global advancement of this field. More than 150 presenters and attendees from all over the world contributed to this congress in the form of presentations, lively discussions, and manuscripts presented in this volume. The international advisory committee members, representing 11 different countries, actively participated in selecting the contributions, reviewing the manuscripts, and promoting the congress.

The congress consisted of 2 keynote presentations from international experts, 96 contributed presentations (in two parallel sessions), 75 poster presentations, and 1 panel discussion. From the poster sessions, outstanding posters were selected for awards, which were presented to the authors at the congress dinner. The event concluded with a closing panel of experts focusing the discussion on the evolution of 3D materials science in the period between the two congresses and the future directions.

The 20 papers presented in this proceedings publication are divided into 6 sections: (1) Acquisition and Handling of 3D Data; (2) Microstructure/Property Relationship in 3D: Characterization and Simulation; (3) Microstructure/Property Relationship in 3D: Deformation and Damage; (4) New Experimental Techniques; (5) Analysis at the Nanoscale; (6) Dynamic Processes. It is our hope that the 2nd International Congress on 3D Materials Science and these proceedings will further the implementation of three-dimensional materials science and broaden its variety of applications.

ACKNOWLEDGMENTS

The organizers/editors would like to acknowledge the contributions of a number of people without whom this 2nd congress, and the proceedings, would not have been possible.

First, we would like to offer many thanks to the TMS staff who worked very efficiently to organize the event and produce this proceedings publication.

Second, we want to thank the international advisory committee for their input in the selection of the papers, their promotion of the congress, and their participation. This international advisory committee included:

- Hamish Fraser, The Ohio State University, USA
- Steve Hall, Lund University, Sweden
- Dorte Juul Jensen, DTU Riso Campus, Denmark
- Milo Kral, University of Canterbury, New Zealand
- Ricardo Lebensohn, Los Alamos National Laboratory, USA
- Ulrich Lienert, Deutsches Elektronen-Synchrotron, Germany
- Qing Liu, Chongqing University, China
- Javier Llorca, IMDEA, Spain
- Eric Maire, INSA, France
- Dierk Rabbe, Max-Planck-Institute, Germany
- Simon Ringer, The University of Sydney, Australia
- Greg Rohrer, Carnegie Mellon University, USA
- Luc Salvo, INP Grenoble, France
- Robert Suter, Carnegie Mellon University, USA
- Hiroyuki Toda, Kyushu University, Japan
- Cnudde Veerle, Ghent University, Belgium

Finally, we would especially like to acknowledge the financial support of our sponsors, especially Carl Zeiss X-ray Microscopy, Inc., FEI and UES, Inc. We are also grateful for the participation and contributions of all the attendees.

EDITORS/ORGANIZERS

DOMINIQUE BERNARD

Dominique Bernard is a CNRS senior researcher. He received his degree in mechanical engineering in 1979 (ENSAM Paris), and his Ph.D. in 1981 (Bordeaux). After a post-doc in Venezuela (1982-1984) in the R&D Institute for the Venezuelan oil industry, he joined the CNRS in 1985. At the Institute of Condensed Matter Chemistry of Bordeaux, Dr. Bernard is leading a team using X-ray computed micro tomography (XCMT) to characterize 3D microstructure of multi materials, to understand and quantify their modifications in time, and to perform realistic numerical simulations of the coupled phenomenon occurring during those modifications. The team's expertise covers a domain going from data acquisition (using synchrotron or micro focus laboratory micro tomograph), data processing (artefacts correction, filtering, 3D reconstruction, 3D registration) and data analysis (3D visualization, 3D image analysis) to numerical modelling and numerical models development (change of scale methods, effective properties calculation, direct numerical modelling at the pore scale). Through a large number of industrial and academic projects, a great variety of materials have been studied: polymer foams under dynamic loading, aluminum alloys during solidification, ceramics during sintering, concrete during leaching, and carbonate rocks during reactive percolation.

JEAN-YVES BUFFIÈRE

Jean-Yves Buffière was appointed as Lecturer at INSA Lyon in September 1994. Since then he has been working on the characterization of damage in advanced materials under load. Through collaboration with the ESRF he has developed the use of high resolution x-ray tomography for the non-destructive 3D characterization of materials. He organized the first European workshop on that topic in 1999. He has supervised or co-supervised several Ph.D. projects and post-doctoral research programs and is the co-author of more than 100 papers in this field. In September 2003, he was appointed a Professor at INSA Lyon.

TRESA POLLOCK

Tresa Pollock is the Alcoa Professor of Materials at the University of California, Santa Barbara. She graduated with a B.S. from Purdue University in 1984, and a Ph.D. from MIT in 1989. Dr. Pollock was employed at General Electric Aircraft Engines from 1989 to 1991, where she conducted research and development on high temperature alloys for aircraft turbine engines. She was a professor in the Department of Materials Science and Engineering at Carnegie Mellon University from 1991 to 1999 and the University of Michigan from 2000 to 2010. Her current research focuses on the processing and properties of structural materials and coatings and on the use of ultrafast lasers for microfabrication and materials diagnostics. Dr. Pollock was elected to the U.S. National Academy of Engineering in 2005, is a Fellow of TMS and ASM International, Editor of *Metallurgical and Materials Transactions* and was the 2005-2006 President of The Minerals, Metals & Materials Society.

HENNING FRIIS POULSEN

Henning Friis Poulsen has been a Professor of X-ray Physics at the Physics Department at the Technical University of Copenhagen (DTU) since 2011. During the years 2000-2011, he worked as first a senior researcher and later a Professor at the Risø National Laboratory in the "Centre of Excellence: metal structures in four dimensions." During the last five years he was head of the group. His research interest is x-ray imaging and microscopy and its application to materials science, in particular within sustainable energy and structural materials. Dr. Henning is chairing the community of Danish synchroton and neutron users, heading efforts to establish a 3D imaging center at DTU and member of advisory panels and boards of ESFRI and a number of large scale research facilities. He received an ERC Advanced grant in 2011 and is responsible for a number of programs funded by EU and Danish Science agencies. In addition he is involved in two start-up companies.

ANTHONY ROLLETT

Anthony Rollett has been a Professor of Materials Science and Engineering at Carnegie Mellon University (CMU) since 1995. He has been Professeur Invité at the LEM3 laboratory in Metz since 2005 and has visited every year. He teaches courses in microstructure-property relationships, transport in materials, materials for nuclear energy, and texture and anisotropy. Previously, he worked for the University of California at the Los Alamos National Laboratory from 1979 to 1995. During this period, Dr. Rollett spent ten years in management with five years as a Group Leader (and then Deputy Division Director) at Los Alamos, followed by five years as Department Head at CMU (1995-2000). He has been a Fellow of ASM since 1996, Fellow of the Institute of Physics (UK) since 2004, Fellow of TMS since 2011, and received the Cyril Stanley Smith Award from TMS in 2014. He has a research group of about ten students and is responsible for a number of programs funded by the NSF, AFOSR, ONR, DOE, and other agencies. The main focus of his current research is on the measurement and prediction of microstructural evolution, along with the relationship between microstructure and properties, with a particular emphasis on three-dimensional simulations.

MICHAEL UCHIC

Michael Uchic is a Senior Materials Engineer in the Metals Branch of the Materials & Manufacturing Directorate, Air Force Research Laboratory. He graduated from Stanford University with a Ph.D. in Materials Science and Engineering, and for his thesis he characterized the low-temperature mechanical properties of the intermetallic alloy Ni_3Al. After joining the Directorate in 1998, he worked on the development of nanocrystalline aluminum alloys and the direct vapor synthesis of high temperature alloys. In 2001, he changed research focus with the start of DARPA Accelerated Insertion of Materials program, and since that time he has focused on the development of new experimental methods to rapidly assess the 3D microstructure and local mechanical properties of aerospace materials. In 2004, he was recognized for his research efforts in micro-mechanical testing with the AFRL/ML Charles J. Cleary Award for Scientific Achievement.

3DMS CONGRESS ORGANIZERS

Dominique Bernard	Institute of Condensed Matter Chemistry of Bordeaux-CNRS, France
Jean-Yves Buffière	INSA-Lyon, France
Tresa Pollock	University of California Santa Barbara, USA
Henning Friis Poulsen	Technical University of Denmark, Denmark
Anthony Rollett	Carnegie Mellon University, USA
Michael Uchic	U.S. Air Force Research Lab, USA

3DMS INTERNATIONAL ADVISORY COMMITTEE

Hamish Fraser	The Ohio State University, USA
Steve Hall	Lund University, Sweden
Dorte Juul Jensen	DTU Riso Campus, Denmark
Milo Kral	University of Canterbury, New Zealand
Ricardo Lebensohn	Los Alamos National Laboratory, USA
Ulrich Lienert	Deutsches Elektronen-Synchrotron, Germany
Qing Liu	Chongqing University, China
Javier Llorca	IMDEA, Spain
Eric Maire	INSA, France
Dierk Rabbe	Max-Planck-Institute, Germany
Simon Ringer	The University of Sydney, Australia
Greg Rohrer	Carnegie Mellon University, USA
Luc Salvo	INP Grenoble, France
Robert Suter	Carnegie Mellon University, USA
Hiroyuki Toda	Kyushu University, Japan
Cnudde Veerle	Ghent University, Belgium

Acquisition and Handling of 3D Data

2nd International Congress on 3D Materials Science
Edited by: Dominique Bernard, Jean-Yves Buffière, Tresa Pollock, Henning Friis Poulsen, Anthony Rollett, and Michael Uchic
TMS (The Minerals, Metals & Materials Society), 2014

EQUILIBRIUM GAP REGULARIZED RADIO-BASED DIGITAL VOLUME CORRELATION

T. Taillandier-Thomas[1], A. Bouterf[1], H. Leclerc[1], F. Hild[1] and S. Roux[1]

[1] LMT-Cachan (ENS Cachan/CNRS/PRES UniverSud Paris)
61 avenue du Président Wilson, F-94235 Cachan, France

Keywords: Digital Volume Correlation, Reconstruction, Tomography

Abstract

The measurement of 3D displacement fields experienced by a sample that has been reconstructed in its reference state can be achieved from much less projections than needed to image the sample itself. The principle of the approach is discussed together with proposed extensions.

Introduction

Tomography has grown to an impressive level of maturity, impacting many domains from medicine and biology to materials science. A sign of this maturity is the progressive shift from a qualitative imaging technique (already very precious) to what is now quantitative. Stressing this fantastic evolution, the very recent review by Maire and Withers [1] draws fascinating perspectives for the future.

Among those various directions, following the time evolution of samples, namely tackling 4D imaging, is a natural trend. This can already be achieved through Digital Volume Correlation (DVC) introduced 15 years ago [2]. This technique has been reviewed recently in Ref. [3]. It consists of estimating the displacement field from 3D image pairs acquired before and during a transformation to be characterized (e.g., mechanical loading, chemical reaction, setting, drying). DVC is based on the analysis of two successive 3D images that are reconstructed with the same resolution.

However, because DVC is by nature an ill-posed problem, the kinematic parameters used to quantify the transformation are much fewer than those needed to reconstruct a full 3D image. Therefore, the details of the microstructure that are generally weakly deformed (so as to be tracked from the reference image to the deformed one) are reconstructed in the deformed image as if they were unknown. The principle of the proposed approach is to avoid a second full reconstruction, and hence work with a limited number of projections. The difficulty is then to estimate the displacement field directly from these few projections (and the initially reconstructed volume).

Principle

Tomography consists of reconstructing a 3D image of a sample from a series of radiographs (projections) of the object rotated about a fixed axis (z). The cologarithm of the intensity reduction in the projection at position (r, z) for an angle of rotation θ, is called $p(r, \theta, z)$. Well-mastered algorithms exist to perform an inverse-Radon transform

and obtain the 3D image (of the X-ray absorbtion coefficient) of the sample, $f(x, y, z)$ (see Ref. [4] for a review). This linear reconstruction operator is denoted $\mathfrak{R}$, so that $f = \mathfrak{R}[p]$. The direct operator, i.e. the projection $\mathfrak{P}$, such that $p = \mathfrak{P}[f]$, is the inverse operator.

The situation that is considered is the following: a sample in its reference state has been imaged at full resolution and is denoted $f_0(x, y, z) = f_0(\boldsymbol{x})$ (where boldface characters such as $\boldsymbol{x}$ denote vectors (x, y, z)). After deformation, the same sample would be imaged as $f_1(\boldsymbol{x})$. Assuming that the only transformation is a mere displacement field (with no alteration of absorption), the two images are related by the (Eulerian) displacement field

$$f_1(\boldsymbol{x}) = f_0(\boldsymbol{x} - \boldsymbol{u}(\boldsymbol{x})) \tag{1}$$

Classical DVC consists of measuring $\boldsymbol{u}$ from f_0 and f_1. However because of the ill-posedness of the problem, $\boldsymbol{u}$ is regularized by limiting its spatial variability. A common way of reaching this goal is to look for a decomposition of the field $\boldsymbol{u}$ in a vector space generated by a library of chosen displacement fields $\boldsymbol{\phi}_i(\boldsymbol{x})$ for $i = 1, ..., N$. Hence, the unknowns are the amplitudes a_i such that

$$\boldsymbol{u}(\boldsymbol{x}) = a_i \boldsymbol{\phi}_i(\boldsymbol{x}) \tag{2}$$

and the number of these unknowns, N, is much lower than the number of voxels in the images f_0 or f_1. The spirit of DVC is thus to determine the unknown amplitudes, gathered in vector $\boldsymbol{a}$, from the minimization of the quadratic norm of the difference between the reference image convected by the displacement field and the deformed image

$$\boldsymbol{a} = \text{Argmin} \left[\| f_1(\boldsymbol{x}) - f_0(\boldsymbol{x} - a_i \boldsymbol{\phi}_i(\boldsymbol{x})) \|^2 \right] \tag{3}$$

Recently, an alternative strategy, referred to as projection-based DVC (or P-DVC) has been proposed [5], which formally only consists of choosing a different metric. Let us denote $\boldsymbol{r} = (r, \theta, z)$ the radiographs coordinates and $\mathfrak{P}[f_1(\boldsymbol{x})] = p_1(\boldsymbol{r})$ the projections of the deformed image. Using the fact that the reconstruction operator is linear, the principle of P-DVC is to evaluate $\boldsymbol{a}$ from

$$\begin{aligned} \boldsymbol{a} &= \text{Argmin} \left[\| \mathfrak{P}[f_1(\boldsymbol{x})] - \mathfrak{P}[f_0(\boldsymbol{x} - a_i \boldsymbol{\phi}_i(\boldsymbol{x}))] \|^2 \right] \\ &= \text{Argmin} \left[\| p_1(\boldsymbol{r}) - \mathfrak{P}[f_0(\boldsymbol{x} - a_i \boldsymbol{\phi}_i(\boldsymbol{x}))](\boldsymbol{r}) \|^2 \right] \end{aligned} \tag{4}$$

It is worth noting that $p_1(\boldsymbol{r})$ is a direct acquisition and does not involve the reconstruction processing. It is also important to stress that since f_0 is the texture of the sample the overall functional to be minimized is highly nonlinear in $\boldsymbol{a}$, both for standard and projection-based DVC. Therefore, it is not possible within this approach to avoid the reconstruction steps of the reference image f_0.

There are a number of advantages to use the latter formulation:

- First, as mentioned above, because the number of unknowns N is much less than the number of voxels, the determination of the unknowns $\boldsymbol{a}$ is much less demanding than the reconstruction of f_1. Therefore, in the above quadratic norm, a sub-sampling of the angles θ may be used. This sub-sampling constitutes a very

significant gain in acquisition time. Just to give an order of magnitude for the real case treated hereafter, where the data have been collected to perform a classical DVC analysis, the number of processed projections was 600 for reconstruction, and it could be cut down to 2 for the determination of a displacement field decomposed over a mesh made of tetrahedra. A gain by more than two orders of magnitude is quite remarkable.

- Second, because the projection $p_1(\boldsymbol{r})$ is a direct measurement, it is not affected by well-known reconstruction artifacts, and in particular noise, which is typically white in the images, can easily be processed, whereas after reconstruction, it displays long-range correlations and is not even stationary. Similarly, most of the long-range correlations introduced in f_0 are unscrambled when projecting back the warped $f_0(\boldsymbol{x}-\boldsymbol{u})$. Thus, although not strictly white, this colored noise is much less harmful than in the reconstruction step.

The limit to this approach is that it is much more demanding computation-wise in terms of the numerical solution to an inverse problem. The effect of each transformation parameter is distributed over the entire set of radiographs and thus has to be disentangled. Ironically, as the number of projections used in the minimization of the DVC functional (see Eq. (4)) is reduced, so does the computation time.

Test Case

To illustrate the proposed methodology, a test case has been carried out considering a tensile test on nodular graphite cast iron performed in situ at the European Synchrotron Radiation Facility, in Grenoble. More details on this example can be found in Ref. [5].

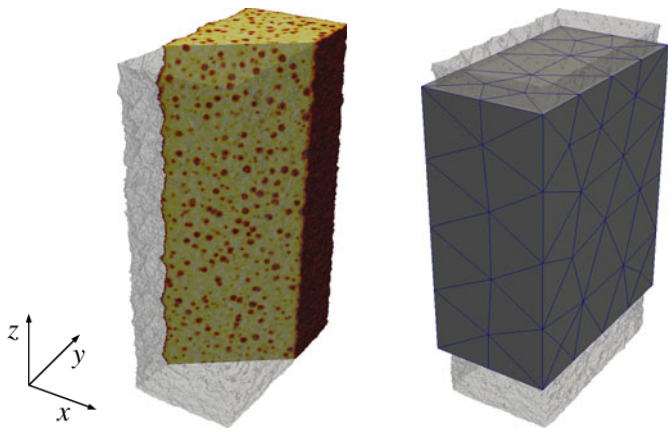

Figure 1: (a) Microstructure of nodular graphite cast iron as obtained from a full tomography, f_0. (b) Mesh composed of 303 T4 elements used to describe the kinematics

The sample was imaged from 600 projections, with a voxel size equal to 5.1 μm. Figure 1 illustrates the microstructure of the sample and shows the mesh being used to

capture its kinematics. Figure 2 shows the displacement field along the tensile axis (z) as obtained from T4-DVC (a) and from the proposed procedure based on only two projections (b).

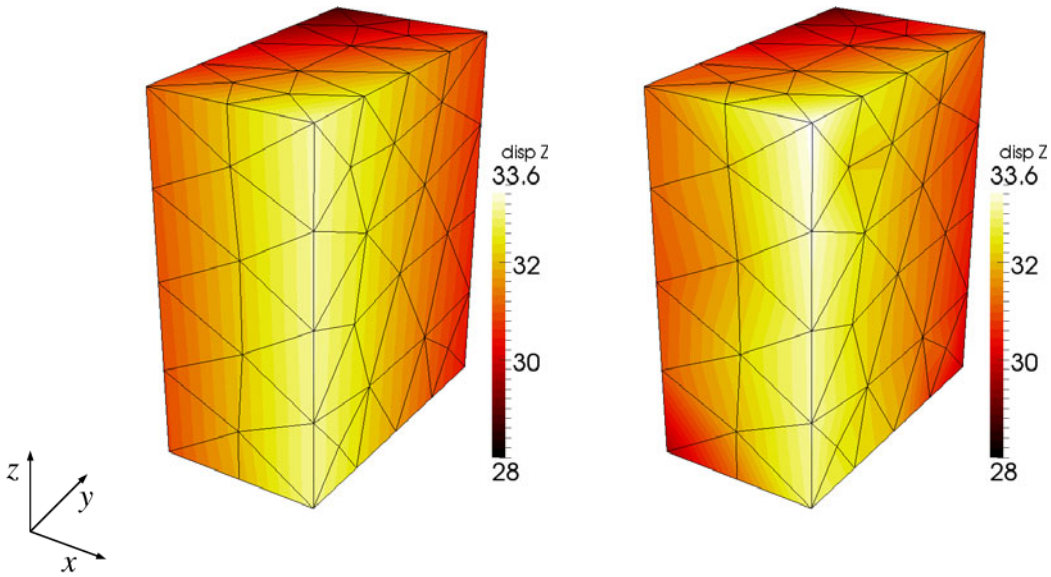

(a) Classical DVC (b) P-DVC using 2 projections

Figure 2: Displacement field along the tensile axis u_z expressed in voxels as estimated (a) from T4-DVC using the full reconstruction of f_1 based on 600 projections, (b) from the projection-based DVC algorithm using only 2 projections. The voxel size is equal to 5.1 μm

A GPU implementation of this algorithm has been performed [5]. For a $200 \times 340 \times 400$-voxel volume, a full reconstruction based on a classical filtered back-projection algorithm, implemented on the same GPU, requires 3.2 s. The proposed analysis depends very much on the number of projections used, but for two projections the displacement field is obtained in 31 s. A CPU (not GPU) version of global DVC computed over the same volume and mesh requires 37 s to compute the same displacement field.

Extensions

The present discussion focuses on two variants aiming at more robust and more accurate transformation determinations.

Mechanical regularization

Digital image or volume correlation may be regularized in the spirit of Tikhonov regularization [6] through the addition to the image registration functional (i.e. the norm used in Eq. (3)), $\mathcal{T}_{DVC}[\boldsymbol{u}] = \|f_1(\boldsymbol{x}) - f_0(\boldsymbol{x} - \boldsymbol{u}(\boldsymbol{x}))\|^2$ another functional, $\mathcal{T}_{Reg}[\boldsymbol{u}]$, the "equilibrium gap" that penalizes deviations from a solution to a linear elastic problem [7, 8]

$$\boldsymbol{a} = \text{Argmin}\left(\mathcal{T}_{DVC}[a_i\boldsymbol{\phi}_i(\boldsymbol{x})] + \alpha\mathcal{T}_{Reg}[a_i\boldsymbol{\phi}_i(\boldsymbol{x})]\right) \tag{5}$$

where α is a parameter discussed farther down. One advantage of this regularization is that it is physically relevant (for linearly elastic homogeneous materials). It describes both the bulk and traction-free boundaries. This feature is particularly attractive as the kinematics has to describe the entire sample volume (Figure 1(b)). Hence, when a finite element description is used to parameterize the displacement field, the mesh has to contain entirely the sample, and hence free surfaces have to be accounted for. These boundary elements are naturally fragile as they are the most prone de fluctuations (X-ray scattering close to interfaces, or phase contrast, presence of noise, lack of constraints from missing neighboring elements). Thus an extra regularization is welcome for those elements. It has been shown [5] that they exhibit higher uncertainties than inner nodes.

Moreover, the equilibrium gap is a quadratic form on the displacement field so that its introduction in Eq. (5) does not introduce any extra difficulty. It can be shown that through the weight α in Eq. (5), a characteristic regularization length scale ξ is introduced (proportional to $\alpha^{1/4}$) below which the regularization constraint is dominant and above which image registration is the most important criterion [5]. Thus regularization can be seen as a low pass filter whose cut-off frequency can be easily and continuously tuned. When a progressively decreasing regularization length scale is chosen, it is possible to control the number of relevant degrees of freedom in a continuous fashion and to benefit from prior determinations to speed up convergence and make it more robust.

Multiscale

One difficulty to be faced with in DVC is the initialization of the computations. When the initial displacement is close to the actual solution, relaxation is fast and efficient. However, when the displacement is too remote, there is a chance of getting trapped in (spurious) secondary minima of $\mathcal{T}_{DVC}[\boldsymbol{u}]$. Although this difficulty is reduced when using a mechanical regularization, it remains an issue.

To alleviate this danger, one useful implementation is to use a multiscale algorithm [9]. It consists of first solving for image registration on coarse images. The latter ones are deduced from f_0 and f_1 by averaging the gray levels of $2\times2\times2$ voxels to form a super-voxel. This coarsening step can be repeated as many times as needed. After achieving image match on the coarsest level, a robust but inaccurate estimate of the displacement field is obtained. It can thus be used as an initial starting point for performing registration on one step finer images, and this recursively performed down to the finest image definition. This multiscale procedure has revealed very convenient and powerful [10]. Moreover the small size of the coarsened images (as compared to original ones) makes them handy for DVC.

A nice property of tomographic reconstruction is that it can handle such multiresolution procedures. Reconstruction from a coarsened projection yields a "blurred" reconstructed image, and thus if enough microstructural details are present in the sample, the same strategy used for solving Eq. (3) can be used for Eq. (4).

Last, it is worth emphasizing that both approaches can be combined, so as to deal with arbitrary unstructured meshes for the displacement field representation. (It is important to rescale the regularization length as the voxel scale is changing, so that the same physical size of ξ is used if the same displacement field is expected. Otherwise a progressive decrease of the physical size of ξ as one tackles finer scales may also be a

convenient convergence strategy.)

Conclusions

Projection-based digital volume correlation is a strategy that may save considerable amounts of tomographic acquisition time (several orders of magnitude) as shown in Ref. [5]. It is suggested herein that mechanical regularization and multiscale strategies could be used to further enhance the stability and robustness of such an algorithm. This saving can be reinvested to enhance time resolution.

References

[1] E. Maire and P.J. Withers, (2014), Quantitative X-ray tomography, Int. Mat. Rev. **59**, (1), 1-43

[2] B.K. Bay, T.S. Smith, D.P. Fyhrie and M. Saad, (1999), Digital volume correlation: three-dimensional strain mapping using X-ray tomography, Exp. Mech. **39**, 217-226.

[3] F. Hild and S. Roux, (2014), Corrélation d'images volumiques, *in* Imagerie 3D en mécanique des matériaux, J.Y. Buffière and E. Maire eds., (Hermès, Paris) Chap. 8, 205-244

[4] A.C. Kak and M. Slaney, (2001), Principles of computerized tomographic imaging, SIAM

[5] H. Leclerc, S. Roux and F. Hild, (2014), Projection savings in CT-based Digital Volume Correlation, Exp. Mech. in press (http://w3.lmt.ens-cachan.fr/PDFs/LECLERC.2014.1.pdf).

[6] A.N. Tikhonov and V.A. Arsenin, (1977), Solution of Ill-posed Problems, (Winston & Sons, Washington)

[7] J. Réthoré, S. Roux and F. Hild, (2009), An extended and integrated digital image correlation technique applied to the analysis fractured samples; The equilibrium gap method as a mechanical filter, Eur. J. Comput. Mech. **18**, 285-306

[8] H. Leclerc, J.N. Périé, S. Roux and F. Hild, (2011), Voxel-scale digital volume correlation, Exp. Mech. **51**, 479-490

[9] F. Hild, B. Raka, M. Baudequin, S. Roux and F. Cantelaube, (2002), Multi-scale displacement field measurements of compressed mineral wool samples by digital image correlation, Appl. Optics **41**, 6815-6828

[10] S. Roux, F. Hild, P. Viot, D. Bernard, (2008), Three dimensional image correlation from X-Ray computed tomography of solid foam, Composites Part A **39**, 1253-1265

2nd International Congress on 3D Materials Science
Edited by: Dominique Bernard, Jean-Yves Buffière, Tresa Pollock, Henning Friis Poulsen, Anthony Rollett, and Michael Uchic
TMS (The Minerals, Metals & Materials Society), 2014

IDENTIFICATION AND CHARACTERIZATION OF SUBGRAIN FEATURES IN 3D EBSD DATA

Andrew Loeb[1], Brian Soe[1], Cullen McMahon[1], Michael Ferry[2], Lori Bassman[1]

[1]Department of Engineering, Harvey Mudd College;
301 Platt Blvd., Claremont, CA 91711 USA
[2]School of Materials Science and Engineering, University of New South Wales;
Sydney NSW 2052, Australia

Keywords: Electron Backscatter Diffraction, 3D EBSD, Segmentation,
Fast Multiscale Clustering, Microbands, Low Angle Boundaries

Abstract

Plastic deformation generates cellular/subgrain structures in many types of metals, and these features have a pronounced influence on mechanical behavior as well as subsequent recovery and recrystallization processes. These features can be observed by electron backscatter diffraction (EBSD) but are challenging to identify automatically. For example, no threshold misorientation angle may adequately capture gradual orientation transitions without noise dominating the result. A more robust technique, fast multiscale clustering (FMC), partitions a data set with attention given to local and global patterns. With FMC, individual data points are combined iteratively into clusters. To determine similarity of clusters during the aggregation process, the method requires an appropriate distance metric. We have adapted FMC to EBSD data, quantifying distance with misorientation and using a novel variance function to accommodate quaternion data. This adaptation is capable of segmenting based on subtle and gradual variation as well as on sharp boundaries within the data, while maintaining linear run time. The method is useful for analysis of any EBSD data set for which the structure of grains or subgrain features is required, and it has been incorporated into the open-source quantitative texture analysis package MTEX. The sensitivity of a segmentation is controlled by a single parameter, analogous to the thresholding angle. To balance the desired identification of subtle boundaries with erroneous oversegmentation, a method to quantitatively optimize this free parameter has been developed. Since the FMC process does not depend on the spatial distribution of points, data can be in either 2D or 3D and organized with any geometry. In fact, the data points may have arbitrary placement, as is the case after correcting for instrument drift. Often investigation of the relationship between structure and formation mechanisms requires extraction of coherent surfaces from cluster volumes. FMC has been further modified to group closed 3D boundaries into distinct surfaces based on local normals of a triangulated surface. We demonstrate the capabilities of this technique with application to 3D EBSD data with subtle boundaries from a deformed Ni single crystal sample. In addition, a recrystallizing steel microstructure with three magnitudes of boundaries is analyzed to show how FMC can be used to characterize both sharp grain boundaries and more subtle features within the same data set.

Introduction

Motivation and Background

A study of the geometric and crystallographic features of microstructures generated by deformation, annealing and phase transformation can shed light on their mechanisms of formation and how they relate to key properties of the material. A significant feature of many types of deformed metals and alloys is its subgrain structure, which is regularly investigated by

electron backscatter diffraction (EBSD) based on local crystallographic orientation. Unlike high angle grain boundaries, the features of subgrain structures are more subtle in magnitude (low total variation in orientation) and spatially gradual (low point-to-point variation). This makes the identification of subgrain boundaries challenging and, hence, creates a significant challenge with generating reliable data of the spatial distribution of subgrains within the overall deformation substructure for understanding the mechanisms of subgrain formation.

The identification of features in a 3D EBSD data set may be done by grouping points that are not separated by a boundary with misorientation higher than a user-defined threshold. This is a common method in commercial software but fails when applied to subgrain data since there is no threshold angle that identifies the boundaries of interest without being dominated by noise. Figure 1a-c shows an artificially constructed volume of orientation data and thresholding with two angles that illustrate this problem. We present a robust solution to segmenting 3D EBSD data, which identifies the proper boundary geometry shown in Figure 1d.

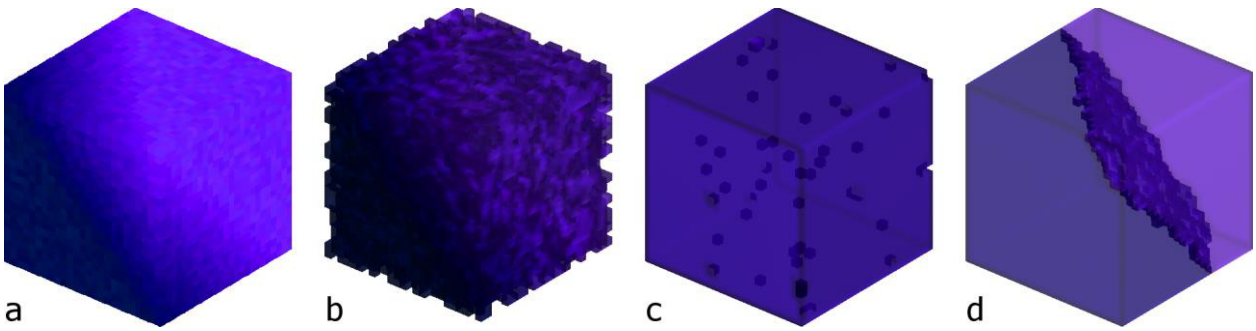

Figure 1: (a) A constructed data set with 25 voxels per side and 9° corner-to-corner misorientation, indicated by color change. The transition occurs linearly along the middle third of the cube diagonal. Noise with average misorientation of 0.5° is added to make the data more realistic. (b) A misorientation threshold angle of 0.5° finds many superfluous boundaries, and (c) a misorientation threshold angle of 0.9° finds very few boundaries. In both cases noise dominates. (d) Segmentation using fast multiscale clustering produces two clusters with a diagonal boundary. Coloring does not have physical significance, contrast shows noise and segmentation boundaries.

Fast Multiscale Clustering

Fast multiscale clustering (FMC) is a segmentation technique developed for 2D image processing [1]. The method creates a hierarchy of scales from groupings of data, starting with individual data points at the finest scale and iteratively coarsening to combine groups. At each scale in the hierarchy every group is then scored based on the similarity of points it contains and distinction from neighboring groups. The highest-scoring groups form the final segmentation of the data. Determining similarity of data requires a metric for measuring distance. For simple color images, this can be a scalar difference between colors, but for application to EBSD data, the metric is based on misorientation. Here, we adapt FMC to work with a quaternion representation for orientation data. A detailed description of FMC and its modifications for EBSD data is provided in [2]. A segmentation with FMC of the artificially constructed data set is shown in Figure 1d.

At each scale in the hierarchy, groups inherit properties from the finer scale below, down to the individual data points [3]. This allows FMC to segment an entire data set with awareness of local and global trends. Another advantage is the freedom to decide neighbors of points, since the

method does not depend on spatial distribution of the data. Thus FMC is not only applicable for 2D situations but is easily applied in 3D. Furthermore, since there are fewer groups at coarser scales, FMC has a runtime linear with the number of data points, a necessity for methods applied to large data sets with more than two dimensions.

Misorientation is not useful on its own when comparing coarse groups containing many data points. Thus, Mahalanobis distance, where the distance between the average aggregated values is divided by the group's variance, is used. This gives groups with low variation in orientation naturally less similarity to their neighbors than groups with high variance. A novel variance aggregation method was developed since the elements of quaternions are not linearly correlated. While this Mahalanobis distance lacks physical significance, it can be scaled at the aggregation step to give sense to closeness and farness, depending on the nature of the data set. The scaling parameter, C_{Maha}, determines the sensitivity of the segmentation [1]. FMC requires several other user-defined values, but fixed values for the rest have been effective for all data sets examined. Hence, FMC has the benefit that it is controlled with a single parameter for application to different data, analogous to the cutoff angle for a thresholding method.

Methods

Preprocessing

Some spatial preprocessing must be carried out since the data is taken in two-dimensional sections. Measurement skew and instrument drift are corrected with a bilinear interpolation on each slice [4]. The data are then globally realigned but points have arbitrary location. Points then may be interpolated to a regular grid for computational efficiency, but FMC can be performed with any data distribution.

Implementation of FMC

The sensitivity of the segmentation, controlled by C_{Maha}, should be different based on the nature of the data. Polycrystalline data should be clustered on the distinct grain boundaries without consideration for variation within grains, but subgrain features are only captured with a more sensitive segmentation. There is no ground truth available for such a segmentation, so the user is responsible for deciding which segmentation to use. Thus, an automated method for determining the optimal value of C_{Maha} has been developed, inspired by similar clustering problems in machine learning [5]. Oversegmentation is characterized by low marginal variance change from splitting existing clusters. Therefore, an 'elbow' in a plot of a global variance measure as a function of C_{Maha} indicates a shift from creating clusters that should be distinct towards erroneously breaking these clusters further. Once this elbow is identified, the segmentation created using the associated value of C_{Maha} is selected as optimal.

Surface Extraction

When analyzing grain or subgrain boundaries, it is often useful to isolate separate faces of an irregular feature. These faces may be defined as regions having similar normal vectors, and as the FMC method developed operates on orientations, only a small further modification is needed for application to normal vectors. With this modification, FMC has been used to extract faces from the set of points on the exterior of a cluster. A triangulation of the boundary surface is performed to estimate local normal vectors, and segmentation produces coherent boundaries. FMC is a powerful tool for this application since it can form a full surface from similar components that are separated by a sharp step in the estimated normal vectors. Two large surfaces from a subgrain feature are shown in Figure 2.

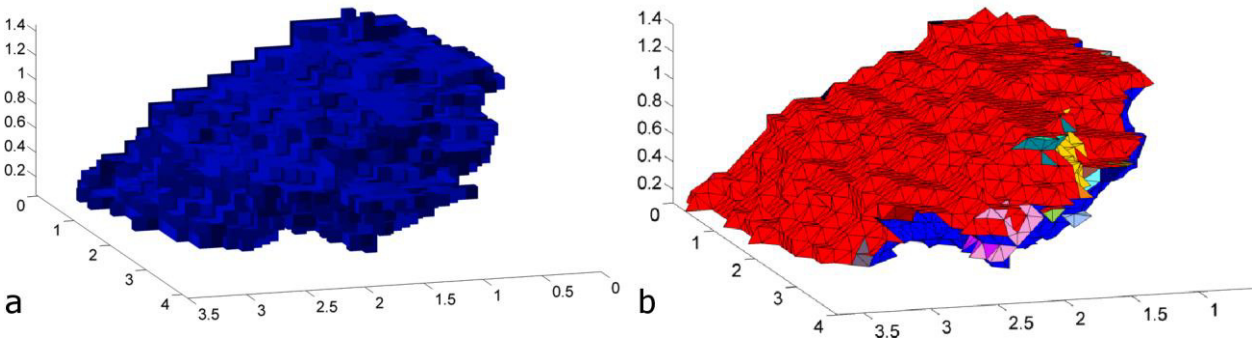

Figure 2: (a) A microband from a deformed nickel single crystal sample (discussed below), (b) with surfaces found with the second application of FMC. Two surfaces, red and blue, are extracted for further analysis, with smaller clusters in the irregular region joining them discarded. Scale is in microns. The colors do not have physical significance.

Results and Discussion

Microbands in Deformed Nickel Single Crystal

Microbands have been isolated in a 3D EBSD data set from a channel die compressed (35% strain) Goss-oriented nickel single crystal with more than 1.3 million data points [6]. The data have a standard deviation from the average orientation of only 0.7°. Figure 3 shows the segmented microbands. Identification of these subgrain features would not be attainable with thresholding

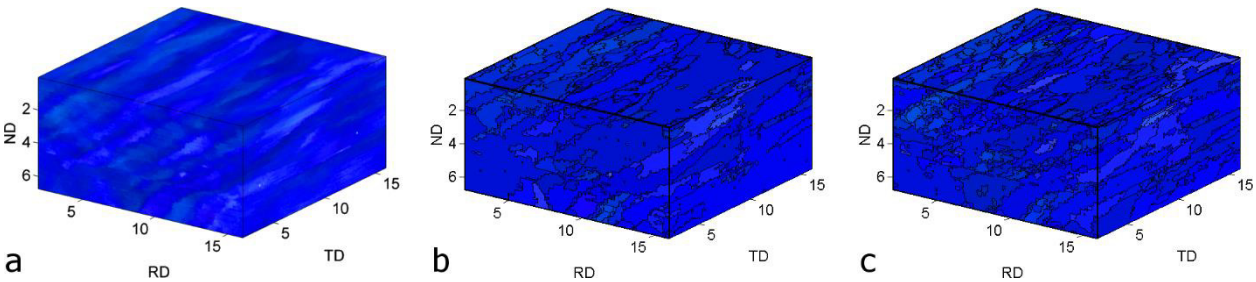

Figure 3: 3D view of the nickel data set (a) EBSD data with inverse pole figure (IPF) coloring, (b) segmentation with the optimal C_{Maha} value of 6, (c) segmentation with a C_{Maha} value of 7, showing the identification of more subtle features. Scale is microns. All orientations are near the original single crystal {110}<001> orientation.

Recrystallized Grains in Partly Recrystallized Steel

Segmentation of a partly recrystallized extra low carbon steel sample containing 350,000 data points [7] illustrates the ability of the FMC method to identify boundaries of different magnitude in the same data set (Figure 4). Here, there are subtle subgrain features, distinct grain boundaries, and a high angle boundary separating α- and γ-fiber regions. The presence of the high angle boundary separating the regions does not affect the detection of boundaries with smaller misorientation because variance comparisons are done with each neighboring segment, rather than globally.

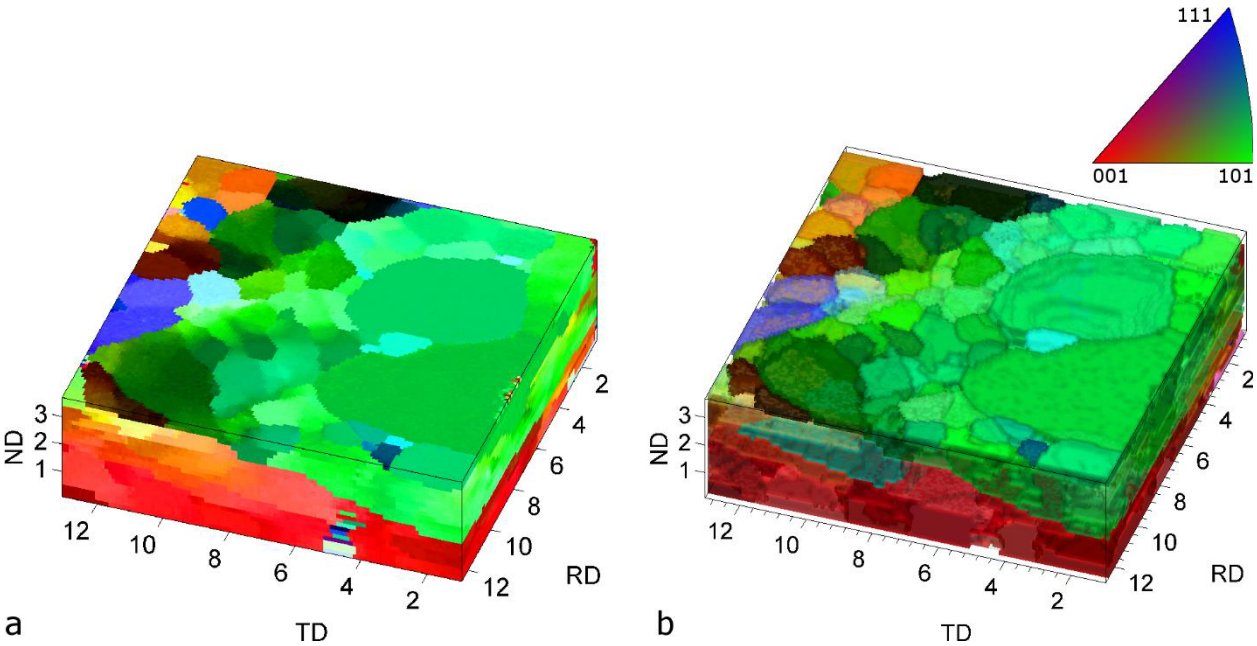

Figure 4: 3D view of the partly recrystallized ELC steel data set (a) EBSD data with IPF coloring and (b) FMC segmentation showing grains and subgrain features containing at least 50 points. Scale is microns.

Surface Analysis

As an example of a quantitative problem that can be solved with FMC segmentation, we investigated the hypothesis that local spatial irregularity in microband boundaries is associated with higher misorientation across the boundary. Figure 5 shows a surface of a microband from the nickel data set showing local curvature and pointwise misorientation. Indeed, some correlation can be seen and warrants further study.

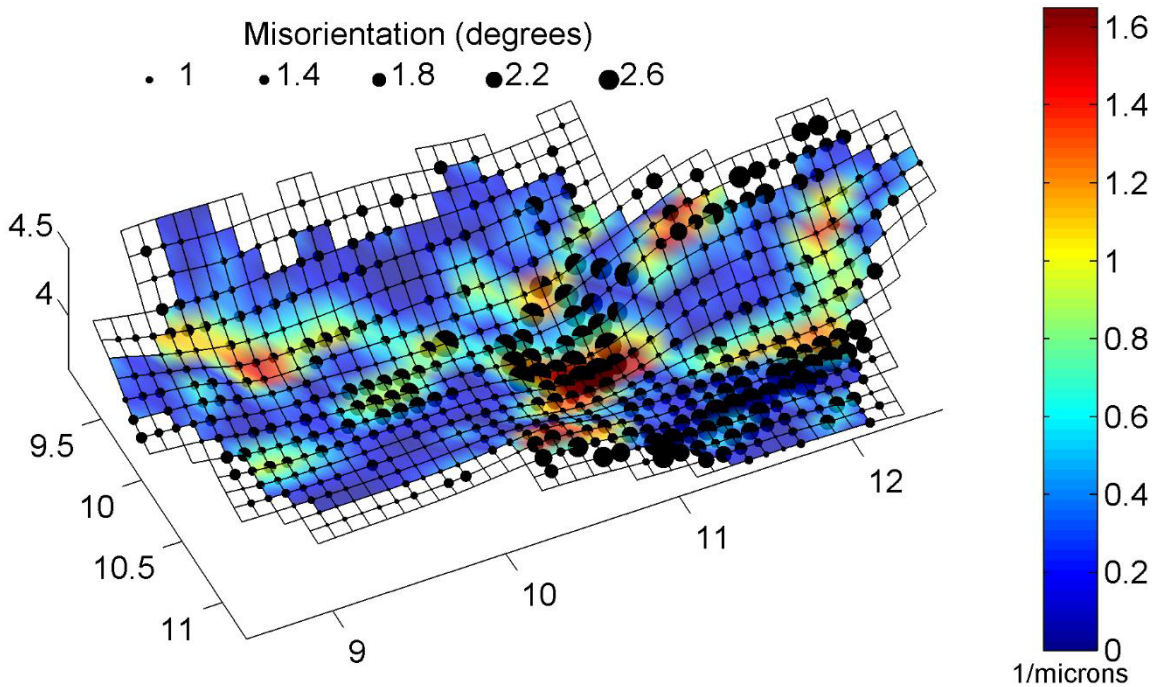

Figure 5: Subgrain surface in deformed nickel showing correlation between local curvature (coloring) and local misorientation across the boundary (dot size).

The foregoing examples illustrate that fast multiscale clustering is an effective tool for segmenting 3D EBSD data set containing subtle and gradual variations in orientation. To facilitate its use in the materials science community, we have incorporated FMC modified to operate on orientation data into the free open source texture analysis software package MTEX [8], thereby allowing users to take advantage of its existing methods for importing and manipulating data. All EBSD segmentation and plotting described herein have been done with this package. The ability of the method to segment data based on a wide range of boundary magnitudes with linear runtime make FMC a robust method for both 2D and 3D segmentations.

Acknowledgements

This work was supported by the Laspa Fellowship, the National Science Foundation (DMR-0907240 and DGE-1144153), the Australian Research Council Centre of Excellence for Design in Light Metals (CE05611574), the Harvey Mudd College Department of Engineering and the Electron Microscope Unit at the University of New South Wales. We thank Md. Zakaria Quadir and Nasima Afrin for discussion of the nickel data set and Wanqiang Xu for the steel data set.

References

[1] D. Kushnir, M. Galun, A. Brandt, "Fast multiscale clustering and manifold identification," *Pattern Recognition*, 39 (2006) 1876-1891.

[2] C. McMahon, B. Soe, A. Loeb, A. Vemulkar, M. Ferry, L. Bassman, "Boundary identification in EBSD data with a generalization of fast multiscale clustering," *Ultramicroscopy*, 133 (2013) 16-25.

[3] E. Sharon, M. Galun, D. Sharon, R. Basri, A. Brandt, "Hierarchy and adaptivity in segmenting visual scenes," *Nature*, 442 (2006) 810-813.

[4] B. Soe, C. McMahon, D. Golay, M.Z. Quadir, M. Ferry, L. Bassman, "Subgrain boundary identification in 3D EBSD data through fast multiscale clustering," *Proceedings First International Congress on 3D Materials Science* (2012) 189-194.

[5] C.A. Sugar, L.A. Lenert, R.A. Olshen, "An application of cluster analysis to health services research: empirically defined health states for depression from the sf-12," *Technical Report.* Stanford University (1999).

[6] N. Afrin, M.Z. Quadir, L. Bassman, J.H. Driver, A. Albou, M. Ferry, "The three-dimensional nature of microbands in a channel die compressed Goss-oriented Ni single crystal," *Scripta Materialia*, 64 (2011) 221-224.

[7] W. Xu, M.Z. Quadir, M. Ferry, "A high-resolution three-dimensional electron backscatter diffraction study of the nucleation of recrystallization in cold-rolled extra-low-carbon steel," Metallurgical *and Materials Transactions A*, 40A (2009) 1547-1556.

[8] F. Bachmann, R. Hielscher, H. Schaeben, "Texture analysis with MTEX – free and open source software toolbox," *Solid State Phenomena*, 160 (2010) 63-68.

Microstructure/Property Relationship in 3D: Characterization and Simulation

2nd International Congress on 3D Materials Science
Edited by: Dominique Bernard, Jean-Yves Buffière, Tresa Pollock, Henning Friis Poulsen, Anthony Rollett, and Michael Uchic
TMS (The Minerals, Metals & Materials Society), 2014

3D STOCHASTIC MODELING OF MICROSTRUCTURE EVOLUTION DURING THE SOLIDIFICATION OF DENDRITIC ALLOYS

L. Nastac and D. Zhang

The University of Alabama, Department of Metallurgical and Materials Engineering,
Box 870202, Tuscaloosa, AL, 35487, USA, email: lnastac@eng.ua.edu

Keywords: 3D stochastic mesoscopic modeling; Casting; Solidification processing; Dendritic microstructure evolution

Abstract

A comprehensive three-dimensional (3D) stochastic model for simulating the evolution of dendritic crystals during the solidification of binary alloys was developed. The model includes time-dependent computations for temperature distribution, solute redistribution in the liquid and solid phases, curvature, and growth anisotropy. 3D mesoscopic computations at the dendrite tip length scale were performed to simulate the evolution of columnar and equiaxed dendritic morphologies and compared then with predictions obtained with 2D mesoscopic computations.

Introduction

A two-dimensional (2D) stochastic model was developed for the modelling of the evolution of dendritic morphologies during solidification [l]. Favorable comparison of predictions with measured microstructures requires the 2D stochastic model to be extended to 3D. Several 3D models for simulating dendritic growth have been proposed in the literature including phase field approach [2, 3] and Lattice Boltzmann and Cellular Automaton approach [4]. To be efficient, these models require parallel computations and can be used only for relatively small domains. A 3D Cellular Automaton approach for modeling the evolution of dendritic grains has also been developed [5]. This 3D dendritic grain model is relatively fast but it cannot simulate the evolution of dendrites and of microsegregation patterns at the dendrite tip level. Thus, main goal of the current contribution is to develop an efficient 3D stochastic mesoscale dendritic growth model based on the previously developed 2D stochastic mesoscale dendritic growth model presented in [1]. Comparisons of 2D and the 3D predictions in terms of microstructure evolution are also provided.

Stochastic Dendritic Solidification Model

The mathematical representation of the dendritic solidification process of a binary alloy is considered in a restricted 3-D domain (Ω). A cross section of this 3D domain is shown in Fig. 1. Here, $\vec{n}$ is the interface normal vector, $\overline{K}$ is the mean curvature of the interface, and the curve Γ represents the solid/liquid (S/L) interface which evolves in time and has to be found as part of the solution. The solidification of binary alloys is governed by the evolution of the temperature ($T(x, y, z, t)$) and concentration ($C(x, y, z, t)$) fields that have to satisfy several boundary conditions at the moving S/L interface as well as the imposed initial and boundary conditions on

the computational domain. The equations that describe the physics of the solidification process in 3-D Cartesian coordinates are as follows (see the 2D equations in [1, 6-8]).

- Temperature (T) in Ω (heat transfer equation):

$$\rho\, c_p \frac{\partial T}{\partial t} = \frac{\partial}{\partial x}\left(K \frac{\partial T}{\partial x} \right) + \frac{\partial}{\partial y}\left(K \frac{\partial T}{\partial y} \right) + \frac{\partial}{\partial z}\left(K \frac{\partial T}{\partial z} \right) - \rho\, L \frac{\partial f_L}{\partial t} \text{ with } f_L = 1 - f_S \quad (1)$$

where t is time, ρ is the density, K is the thermal conductivity, c_p is the specific heat, L is the latent heat of solidification, f_L is the liquid fraction, f_S is the solid fraction, and x, y and z are the domain coordinates.

- Concentration (C) in Ω (solute diffusion equation):

In the liquid phase (C_L):
$$\frac{\partial C_L}{\partial t} = \frac{\partial}{\partial x}\left(D_L \frac{\partial C_L}{\partial x} \right) + \frac{\partial}{\partial y}\left(D_L \frac{\partial C_L}{\partial y} \right) + \frac{\partial}{\partial z}\left(D_L \frac{\partial C_L}{\partial z} \right) \quad (2)$$

In the solid phase (C_S):
$$\frac{\partial C_S}{\partial t} = \frac{\partial}{\partial x}\left(D_S \frac{\partial C_S}{\partial x} \right) + \frac{\partial}{\partial y}\left(D_S \frac{\partial C_S}{\partial y} \right) + \frac{\partial}{\partial z}\left(D_S \frac{\partial C_S}{\partial z} \right) \quad (3)$$

where D_L and D_S are the interdiffusion coefficients in the liquid and solid, respectively.

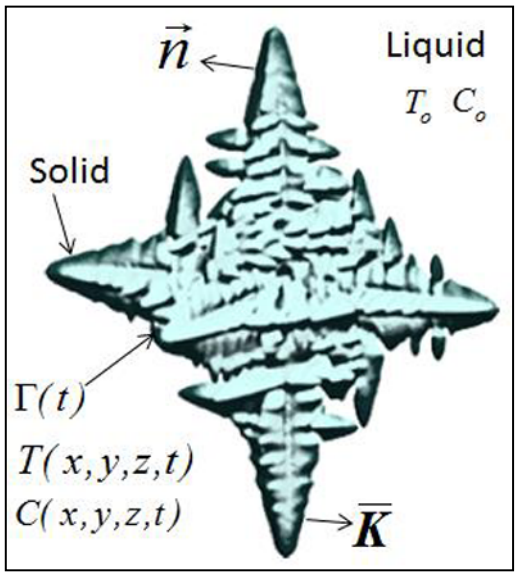

Figure 1. A 3D-domain for dendritic solidification.

Local equilibrium at the S/L interface on $\Gamma(t)$ (here, "*" means at interface):

$$C_S^* = k\, C_L^* \quad (4)$$

- Solute conservation at the S/L interface:

$$V_n^*\, C_L^*\, (k-1) = \left(-D_L \left(\frac{\partial C_L}{\partial x} + \frac{\partial C_L}{\partial y} + \frac{\partial C_L}{\partial z} \right) + D_S \left(\frac{\partial C_S}{\partial x} + \frac{\partial C_S}{\partial y} + \frac{\partial C_S}{\partial z} \right) \right) \cdot \vec{n} \quad (5)$$

where V_n^* is the normal velocity of the interface and $\vec{n}$ denotes the normal to the S/L interface that is pointing into the liquid (see Fig. 1).

- The interface temperature (T^*) is defined as (assuming local equilibrium with both phases):

$$T^* = T_L^{EQ} + \left(C_L^* - C_0 \right) m_L - \Gamma\, \overline{\kappa}\; f(\varphi, \theta) \quad (6)$$

where T_L^{EQ} is the equilibrium liquidus temperature of the alloy, m_L is the liquidus slope, $\overline{\boldsymbol{K}}$ is the mean curvature of the S/L interface, Γ is the Gibbs-Thomson coefficient, and $f(\varphi,\theta)$ is a coefficient that accounts for growth anisotropy, where φ is the growth angle (*i.e.*, the angle between the normal and the growth axis) and θ is the crystallographic orientation angle.

In Eq. (6), second term in the right side is the constitutional undercooling and the last term in the right side is the curvature undercooling (that reduces the total undercooling at the dendrite tip, that is, has a stabilizing effect on the S/L interface). The interface temperature is also affected by the kinetic undercooling. The kinetic undercooling is not accounted for in this model since its effect becomes significant only at very high solidification velocities (*i.e.*, in the rapid solidification regime). Also, the coefficient $f(\varphi,\theta)$ in Equation (6) assumes an axisymmetric approximation where the anisotropy and the interface shape are independent of the polar angle ϕ in the *x*-*y* plane perpendicular to the growth axis [2].

The solidification process is governed by Eqs. (1) to (6) and a stochastic model for nucleation and growth. The numerical procedures for calculating the nucleation and growth, temperature and concentration fields as well as the growth velocity of the S/L interface are described in details in [9]. It consists of a regular network of cells that resembles the geometry of interest. The model is characterized by (a) geometry of the cell; (b) state of the cell; (c) neighborhood configuration; and (d) several transition rules that determine the state of the cell. In this work, the geometry of the cell is a cube. Each cell has three possible states: "liquid", "interface", or "solid". The selected neighborhood configuration is based on the cubic von Neumann's definition of neighborhood, that is the first order configuration and it contains the first six nearest neighbors. Solidification behavior depends to a great extent on the transition rules. In this model, the change of state of the cells from "liquid" to "interface" to "solid" is initiated either by nucleation or by growth of the dendrites.

An explicit finite difference scheme is used for calculating the concentration fields in the liquid and solid phases. Zero-flux boundary conditions were used for cells located at the surface of the geometry. The solution algorithm includes the "interface" cells by multiplying the concentration in the liquid by the liquid fraction and the concentration in the solid by the solid fraction of the particular interface cell. Also, during each time-step calculation and for each "interface" cell, the previous values of the liquid and solid concentrations are updated to the current values of the interface liquid and solid concentrations calculated with Eqs. (4), (5) and (7). The calculation of the interface liquid concentration, C_L^* can be obtained from Eq. (6) as

$$C_L^* = C_O + \frac{\left(T^* - T_L^{EQ} + \Gamma\ \overline{K}\ f(\varphi,\theta)\right)}{m_L} \tag{7}$$

The procedures for calculating $\overline{K}$ and $f(\varphi,\theta)$ are described below.

The average interface curvature for a cell with the solid fraction f_S is calculated with the following expression:

$$\overline{K} = \frac{1}{a}\left(1 - 2\frac{f_S + \sum_{k=1}^{N} f_S(k)}{N+1}\right) \tag{8}$$

where N is the number of neighboring cells. In the present 3D calculations, $N = 26$, that contains all the first order neighboring cells (including the diagonal cells). Equation (8) is a simple

counting-cell technique that approximates the mean geometrical curvature (and not the local geometrical curvature). An improved curvature model is presented in [8]. A comparison of 2D simulations obtained with these curvature models was also provided in [8].

The anisotropy of the surface tension (see Eq. (6)) is calculated as [2]:

$$f(\varphi,\theta)=1+\frac{4\delta}{1-3\delta}\left(cos^4(\varphi-\theta)+\frac{3}{4}sin^4(\varphi-\theta)\right) \quad \text{with } \varphi=acos\left(\frac{V_z}{\left[(V_x)^2+(V_y)^2+(V_z)^2\right]^{1/2}}\right) \quad (9)$$

where φ is the angle between the normal direction to the solid-liquid interface and the [100] direction (growth axis), V is computed with Eq. [12] in [10], θ is calculated with Eq. (7) in [10] and δ accounts for the degree of anisotropy. For cubic symmetry, $\delta = 0.047$ [2].

The algorithm is presented in [10]. The simulation software was written in Visual Fortran 90. The output of the model consists of screen plotting at any chosen time of C, T, or color indexes of all cells. Also, the final values of C, T, and color indexes of all cells are saved at the end of computations on the computer disk.

Results and Discussion

Thermo-physical properties of the alloys used in simulations are presented in Table 1. The dimensions of the 2D and 3D simulation domains are 2 mm x 4 mm and 2 mm x 4 mm x 1 mm, respectively. The grid size is fine enough to approximately resolve the dendrite tip radius under the current solidification conditions. Newton cooling boundary condition was applied only to the bottom of the computational domain. All other boundaries were perfectly insulated.

The surface heat transfer coefficient used in the present simulations is $h = 10^3$ W m^{-2} K^{-1}. Zero-flux solute boundary conditions were applied at the boundaries of the computational domain (*i.e.*, a closed system was assumed). The initial melt temperature was 1400 °C. Also, an initial concentration equal to C_o was assumed everywhere on the computational domain.

Table 1. Thermophysical properties of IN718-5Nb used in simulations [9, 11].

Property	μ_N^C [m^{-2} K^{-2}]	μ_N^E [m^{-3} K^{-2}]	L [J/kg]	ρ [kg/m^3]	K [W/m/K]	c_p [J/kg/K]	T_L [°C]
Value	1x10^6	5x10^8	2.9x10^5	7620	30.1	720	1336
Property	C_o [wt.%]	C_{eut} [wt.%]	k_o -	D_L [m^2 s^{-1}]	D_S [m^2 s^{-1}]	m_L [°C %$^{-1}$]	Γ [K m]
Value	5.0	19.1	0.48	3x10^{-9}	1x10^{-12}	-10.5	3.65x10^{-7}

In Fig. 2, a comparison of 2D (a) and 3D (b) simulated microstructures (columnar dendritic morphologies) in unidirectional solidification of IN718-5 wt. % Nb alloy is presented. The 2D computations were done by using the 2D stochastic dendritic model presented in [1, 6-8]. The 3D simulation results are taken from the middle of the simulated sample (x-y plane with z = 0.5 mm). The competition between nucleation and growth of multiple columnar dendrites is evident in both 2D and 3D cases. The strong growth competition from the sample bottom (>20 dendrites) to 1/4 of the sample height (10 dendrites) to 1/2 of the sample height (5 dendrites in 2D and 7 dendrites in 3D) to 3/4 of the sample height (3 dendrites in 2D and 4 dendrites in 3D) can be observed. For 3D computations, more dendrites are observed toward the top of the sample

because more nucleation sites are available in 3D than in 2D and also because some dendrites that are visualized are cut from a different plane. Note also that the columnar morphologies look different in 3D than in 2D.

Figure 3 shows a comparison between 2D and 3D computations in terms of equiaxed dendritic morphologies. The legend in Figs. 2 and 3 shows the 256 color indexes (*CI*, illustrated here in 16 classes, where each class contains 16 different color indexes) that is used for displaying the preferential crystallographic orientation angle.

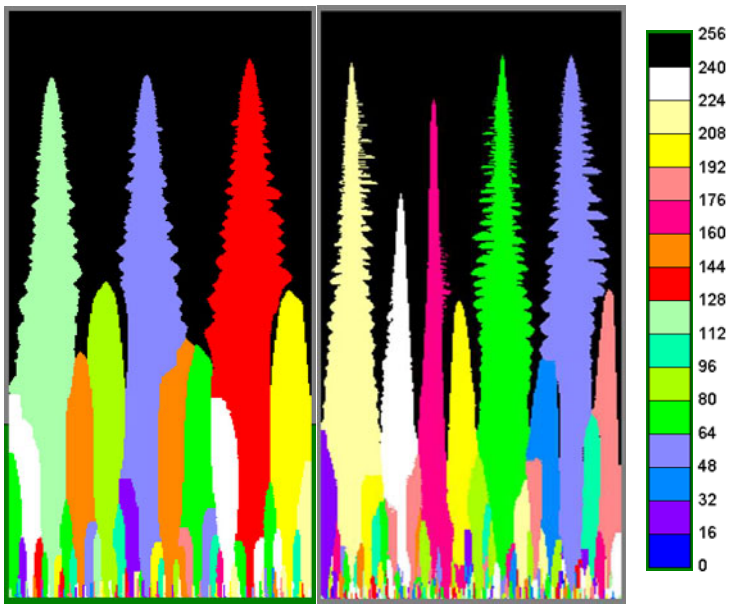

(a) (b) *CI*

Figure 2. Comparison of 2D (a) and 3D (b) simulated microstructures (columnar dendritic morphologies) in unidirectional solidification of IN718-5 wt.% Nb alloy.

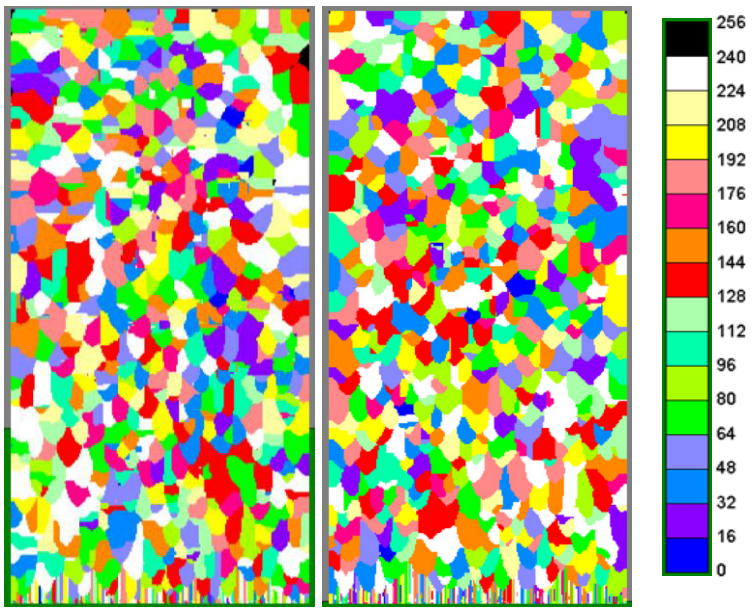

(a) (b) *CI*

Figure 3. Comparison of 2D (a) and 3D (b) simulated microstructures (equiaxed dendritic morphologies) in unidirectional solidification of IN718-5 wt.% Nb alloy

The orientation angles (θ) can be extracted from the legend in Figs, 2 and 3 by using the following equation: $\theta = \pi/2*(CI/255)-\pi/4$. Thus, when $CI/255$ varies from 0 to 1, θ ranges from $-\pi/4$to $\pi/4$.

The equiaxed grain density was $fx10^8$ nuclei/m^2 in 2D and 10^{12} nuclei/m^2 in 3D. The conversion factor $f = \pi/4$ [12]. Similar equiaxed morphologies can be observed from Fig. 3 for both 2D and 3D cases, implying that 2D computations can be used and then the grain size can be converted to 3D by using the "1/f" conversion factor.

A RAM memory size of 100 bytes/cell is needed in the present 3D computations. CPU-time is related to the domain size and the time-step and, for the simulation problems presented in Figs. 2 and 3, is of the order of few hours on a Dell Precision T7500 desktop.

Conclusions

An efficient 3D mesoscale stochastic model was developed. The model was applied to simulate 3D microstructures using PCs with reasonable amount of RAM and CPU time and therefore no parallel computations were needed.

It was observed that the 3D columnar dendritic morphologies look different than the 2D columnar dendritic morphologies. This is due to the fact that, for a 2D geometry, the grain growth is constrained in the x-y plane while for the 3D case it is free in the third (z) direction.

Nevertheless, the predicted 3D equiaxed dendritic morphologies look similar to the 2D equiaxed dendritic morphologies. A simple conversion factor ($4/\pi$) can be used to convert the 2D grain size to 3D grain size.

References

1. L. Nastac, *Acta Materialia*, Vol. 47, No. 17, pp. 4253-4262, 1999.
2. A. Karma and W. J. Rappel, *Phys. Rev. E*, vol. 57, No. 4, pp. 4323–4349, 1998.
3. J. H. Jeong,, N. Goldenfeld, and J. A. Dantzig, *Phys. Rev. E*, vol. 64, 041602. pp. 1-14, 2001.
4. M. Eshragi, S. D. Felicelli, and B. Jelinek, Journal of Crystal growth, vol. 354, issue 1, pp. 129–134, 2012.
5. C. A. Gandin, and M. Rappaz, Acta Met. Vol. 45, No. 5, pp. 2187-2195, 1997.
6. L. Nastac, *4th Pacific Rim International Conference on Modeling of Casting and Solidification Processes (MCSP-4)*, Ed. C. P. Hong, Yonsei University, Seoul, Korea, September 5-8, 1999.
7. L. Nastac, Proceedings of the *"Modelling of Casting, Welding, and Advanced Solidification Processes IX"*, Engineering Foundation, Aachen, Germany, August 20-25, 2000.
8. L. Nastac, Modeling and Simulation of Microstructure Evolution in Solidifying Alloys Springer, New York, 2004 (ISBN 978-1-4020-7831-6).
9. L. Nastac and D. M. Stefanescu, *Modelling and Simulation in Materials Science and Engineering*, *Institute of Physics Publishing*, Vol. 5, No. 4, pp. 391-420, 1997.
10. L. Nastac, A 3-D Stochastic Mesoscopic Model for Prediction of Microstructure Evolution during Solidification of Dendritic Alloys, accepted for publication in the journal of *Metallurgical Research & Technology*, EDP Sciences, March 20, 2014.
11. L. Nastac and D. M. Stefanescu, *Metallurgical Transactions*, Vol. 28A, pp. 1582-1587, 1997.
12. M. Kong, R. N. Bhattacharyal, C. James and A. Basu, Geological Society of America Bulletin, vol. 117, no 1-2, pp. 244-249, 2005.

2nd International Congress on 3D Materials Science
Edited by: Dominique Bernard, Jean-Yves Buffière, Tresa Pollock, Henning Friis Poulsen, Anthony Rollett, and Michael Uchic
TMS (The Minerals, Metals & Materials Society), 2014

ANALYZING MICROSTRUCTURE AND DAMAGE IN CONSTRUCTION MATERIALS WITH 3D MICRO CT

Dietmar Meinel[1], Andreas Staude[1], Karsten Ehrig[1]

[1]BAM, Federal Institute for Materials Research and Testing, Division 8.5 Micro NDE, Unter den Eichen 87, 12205 Berlin, Germany, e-mail: dietmar.meinel@bam.de

Keywords: X-ray computed tomography, concrete, asphalt, corrosion, crack detection, 3D visualization

Abstract

This poster presentation gives an overview of the great potential of X-ray micro computed tomography (CT) to cast light on the evolution of the microstructure in construction materials. Prevention of damage is of major economic and social importance in the development of suitable construction materials such as concrete and asphalt. Therefore a non-destructive testing method such as CT is an appropriate tool for visualization of the inner structure. Its combination with other test methods allows understanding the damage processes such as crack propagation or corrosion. We show examples of internal structure analyses on a wide range of materials: Automatic 3D crack detection and the visualization of corrosion products inside of steel reinforced concrete, pore and shape analysis of lightweight aggregates and the visualization of deformation of high-pressure loaded aerated concrete specimens, distribution of aggregates inside concrete, and determination of the surface of porous asphalt core samples. Segmented structures serve, e.g., as input data for simulation of transport phenomena or virtual load tests.

Introduction

In order to extend the lifetime of buildings and constructions at the macro scale it is necessary to understand the damage processes of building materials at the micro scale. The most commonly used measurement methods to assess the damage processes inside of building materials either provide information on only one property, or no depth information is generated. X-ray computed tomography allows us to analyze the whole volume of the measured specimen non-destructively. 3D image data of the inner structure can be generated after different damage levels or in-situ on the same test object. On the following pages we show a part of the extensive possibilities of CT on the basis of three different examples.

Measurement principle

The object to be examined is positioned on a turntable between X-ray tube and a flat panel detector. A series of radiographic images are recorded during a 360 degree turn of the object. From these 2000 or more X-ray projections a 3D image matrix is reconstructed. Each single volume element (voxel) in this data represents the linear absorption coefficient of the material.
All measurements presented here have been performed on a µCT device assembled at BAM with a 225 kV µ-focus X-ray tube and a 2kx2k flat panel detector (see Fig. 1). The CT data was reconstructed using the standard filtered-backprojection algorithm for cone-beam CT data.

Analysis of ASR-Induced Damage Processes in Concrete

Alkali-silica reaction (ASR) is the reaction between calcium hydroxide in the alkaline cement paste and reactive forms of silica in the aggregate. The resulting expanding gel of calcium silicate hydrate is one of the reasons for initiation and development of cracks in concrete.
The alkali-reactive potential of aggregates is assessed according to the German guidelines by two different test methods [1-2]. These are the 40°C fog chamber storage and as an alternative method the 60°C concrete prism test. In both tests, the discontinuously measured expansion of ASR-generating stored concrete prisms is used as criterion for the internal damage process. The crack formation was temporally and spatially visualized by discontinuously applied CT measurements, which were performed at the concrete sample with a diameter of 70 mm, placed inside the fog chamber storage, by using the CT scanner described above.

Figure 1: µCT setup for analysis of ASR-induced damage processes in concrete

According to the sample diameter of 70 mm a voxel size of 41.3 µm was realized under common µCT setup conditions which does allow visualizing larger ASR-induced cracks. For additional analysis of small cracks we therefore switched to a ROI-CT setup without the fog chamber storage by moving the sample as close as possible to the X-ray tube, resulting in a voxel size of 9.7 µm (see Fig. 2).

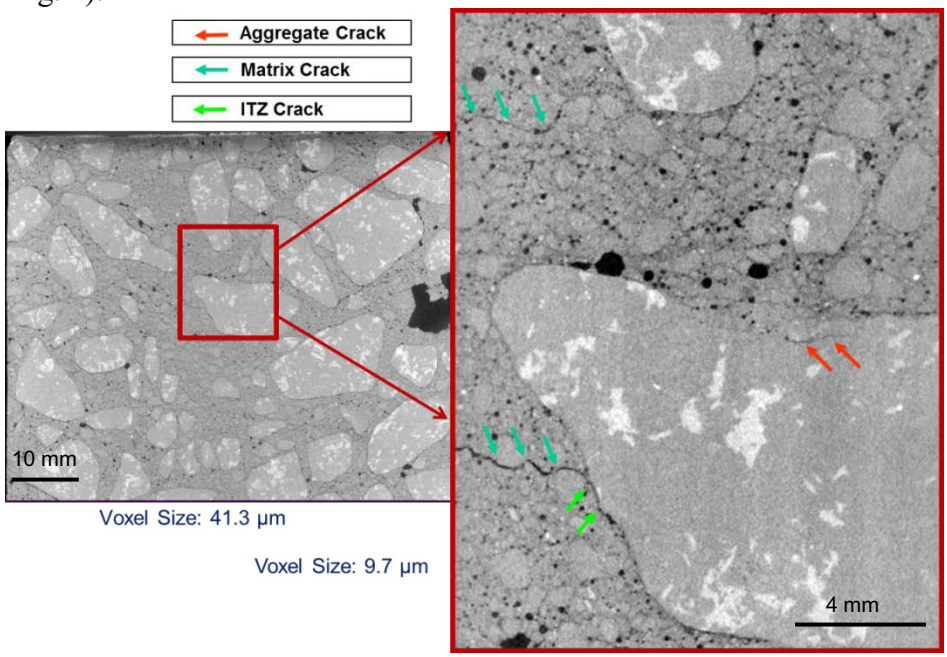

Figure 2: ASR-induced cracks in 2D vertical slices with common and ROI-CT setup

ROI-CT reconstruction has been performed using standard filtered back projection techniques with a constant value for the free beam.
Figure 3 shows a 3D view of the ASR-induced cracks with isosurface, center point, and bounding box together with a 2D orthoslice of the data set. A tool for automated crack detection in 3D-CT data was developed by the Zuse Institute Berlin (ZIB) in cooperation with BAM [3]. Different crack detection methods are available in this software tool (template maching, Hessian-driven percolation). Moreover, quantitative parameters are evaluated according to the crack size (3D voxel volume), crack surface, and crack orientation which will serve as a basis for further statistical evaluation and FEM analysis.

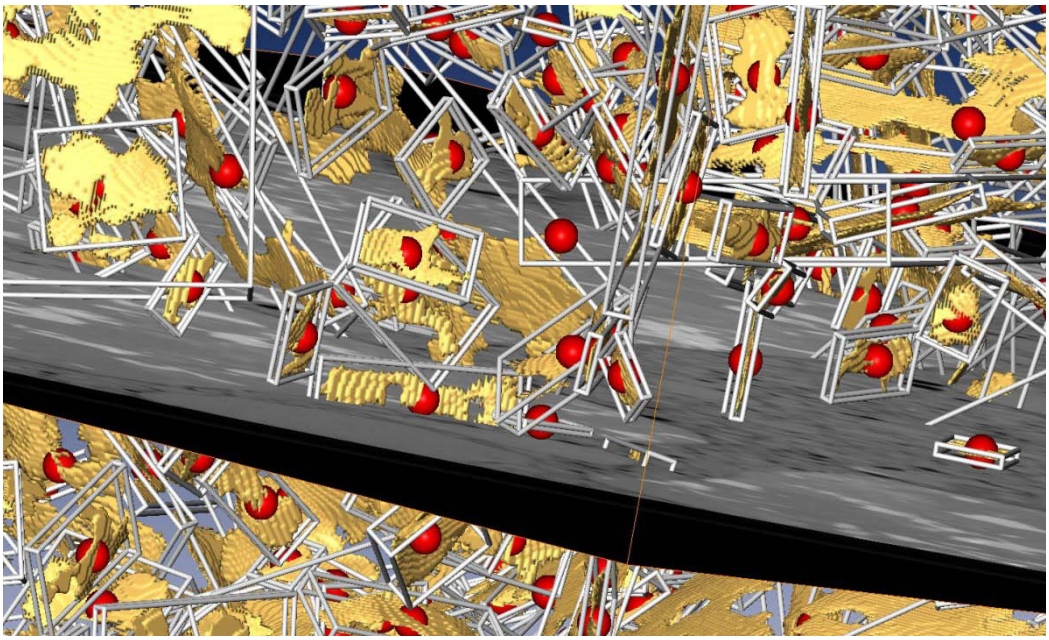

Figure 3: ASR-induced cracks in 3D view with isosurface (yellow), center point (red dot) and bounding box shown together with a 2D orthoslice of the data set

Corrosion Processes inside Steel Reinforced Concrete

The main reason for damages of steel reinforced concrete structures is corrosion. The structural steel, embedded in alkaline concrete, is normally protected against corrosion by a passivation layer. Carbon dioxide and chloride can destroy this protective layer and thus lead to corrosion. The damage process boosts itself due to the additional cracks which are induced by the greater volume of the corrosion products [4]. In order to develop suitable protective measures it is necessary to understand the entire mechanism of damage. CT is well-suited to study damage processes on a laboratory scale. Either drilling samples from old concrete buildings or test samples produced in concrete laboratories can be used.
Different drilling samples with a diameter of 40 mm were examined with CT to study the distribution of corrosion products induced by chlorides inside concrete (see Fig. 4 left). The X-ray tube was running at a voltage of 205 kV with a current of 110µA. For beam hardening reduction, 0.5 mm Cu and 0.5 mm Ag were used as pre-filter. Inside of the CT voxel data, the corrosion products can be segmented according to the density differences (see Fig. 4 right). Splitting the 3D voxel data into smaller evaluation areas allows analyzing the distribution of the corrosion products inside the concrete specimen.

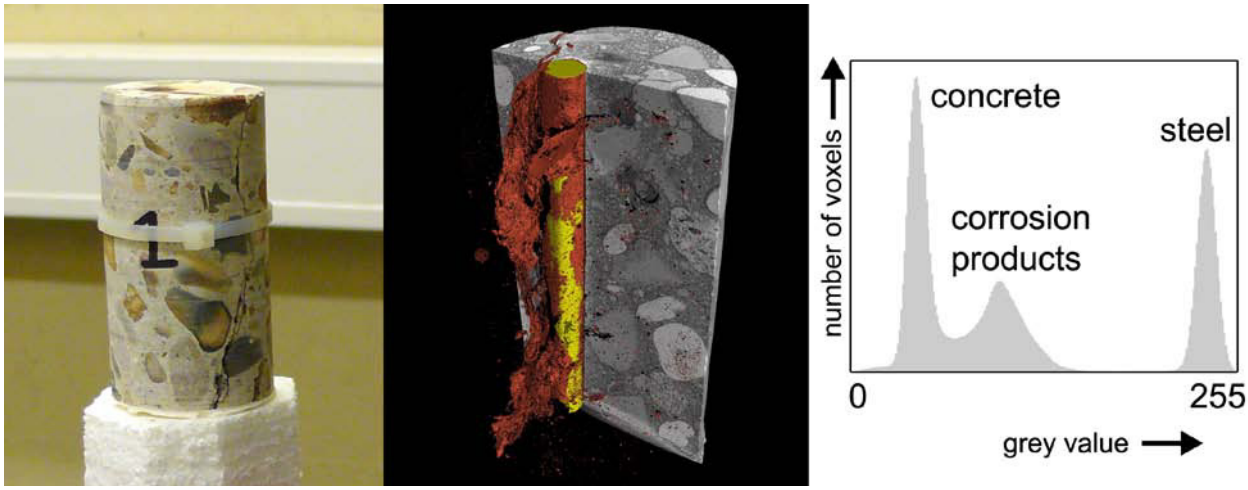

Figure 4: Concrete drilling sample (left: original, middle: 3D-CT with embedded steel bar (yellow) and rust (brown), right: histogram of the three phases)

Also the different damage stages of ongoing degradation processes can be analyzed. The mass loss of the steel bar and the surface, which is involved in the corrosion process, can be determined after each induced damage stage (see Fig. 5).

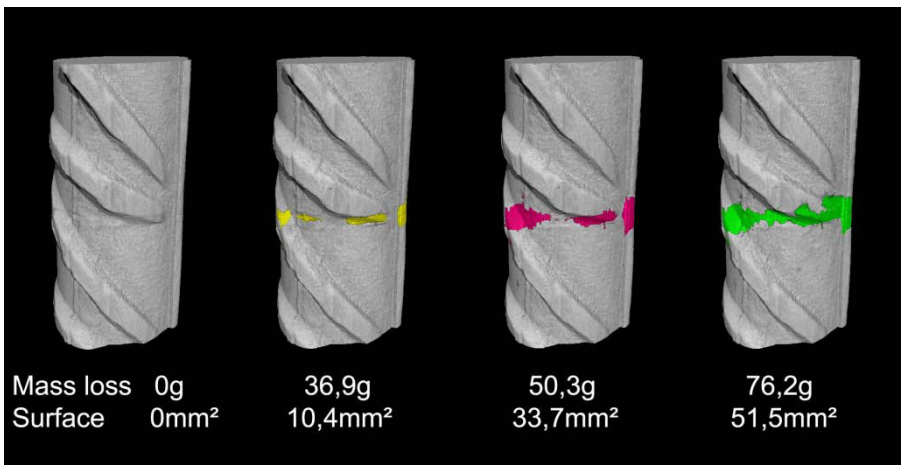

Figure 5: Increasing damage area of the same embedded steel bar (10 mm in diameter) at different stages after chloride induced corrosion

Asphalt

A focus in the development of modern road-building materials lies on the reduction of traffic noise. A typical asphalt road consists of multiple layers with differing mixtures and different properties. One possibility to influence the traffic noise is the creation of a top-layer with a well-defined void-space which is connected to the road-surface. For durability of the pavement, the porosity must not allow water to penetrate to the interface between top and binder layer.
The structure of real pavements is studied at drill cores. The shares of the different phases are traditionally determined by measuring the outer size of the drill core and afterwards decompose the specimen into its constituents. The missing volume is interpreted as the integral porosity.
With CT it is possible to get information from the core non-destructively and to measure the porosity spatially resolved [5].

Figure 6 shows an asphalt drill core of 70 mm diameter during the CT-measurement. The acceleration voltage was 210 kV, a pre-filter of 0.5 mm copper and 0.75 mm silver was used.

Figure 6: Asphalt drill core during CT measurement

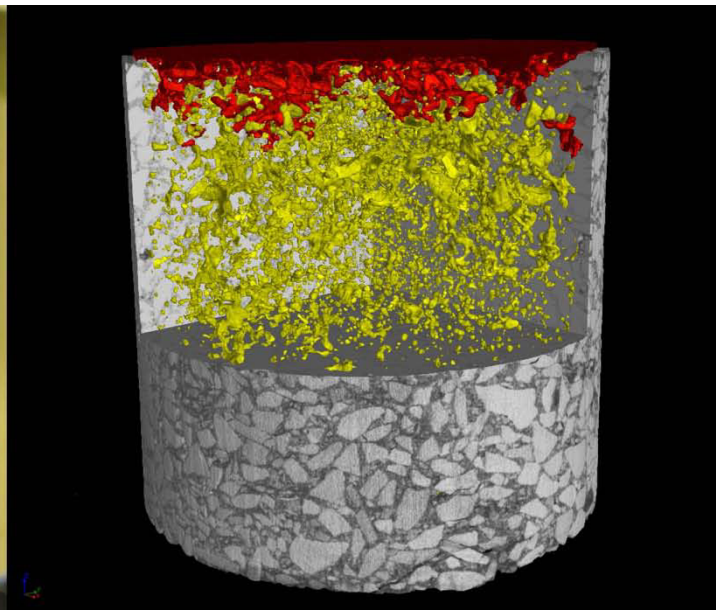

Figure 7: Volume rendering of the CT-data for the drill core: gray: drill core, red: voids connected to the surface, yellow: all remaining voids

The resulting voxel-size was ~60 µm. For a correct segmentation, the beam-hardening was corrected using a lookup-table described by a polynomial. As one is interested in the structure of the pavement with respect to the distance from its surface, the data-set was aligned to a plane fitted onto the surface of the pavement ("reference-plane") before further analysis. To get rid of disturbances of the structure by the specimen-preparation, a cylindrical region-of-interest (ROI) was defined in the data-set with a distance of a few millimeters to the specimen's surface at the sides and the bottom.

Inside this ROI the void fraction in each horizontal slice and the over-all porosity was determined (green in Fig. 8). The main interest of the analysis is focused on the structures relevant for the noise behavior. Thus the voids connected to the pavement's surface were segmented by region growing (red in Fig. 7). An evaluation of this void-fraction with respect to height is shown blue in Fig. 8. As can be seen, below ~15 mm from the surface the voids have no connections to the surface. Apart from the impact on the noise behavior, this property is crucial for the durability of the pavement, because the top-layer shall be watertight to prevent cracking by ice forming at the layer boundary.

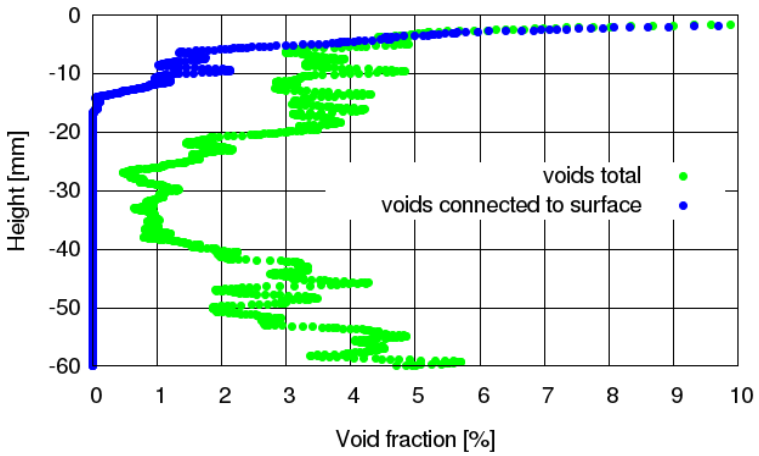

Figure 8: Height-dependent volume fraction of the voids in the drill-core

Conclusion

X-ray micro computed tomography supports the study of micro structure and damage processes in construction materials. It provides among other things information about cracks in concrete specimens induced by ASR or corrosion. Damage processes, like hidden corrosion of steel inside concrete, could be described at different stages. Additionally, CT data serves also as a basis for simulation models, for example numerical flow simulation of water in open porous asphalt.

Acknowledgments

This work was supported by BAM, Division 6.1 “Corrosion in Civil Engineering”, 7.1 “Building Materials”, 7.4 “Technology of Construction Materials”, CEA Saclay, CEA, DEN, DPC, SECR, Laboratoire d’Etude du Comportement des Bétons et des Argiles, F-91191 Gif-sur-Yvette, France, and Zuse Institut Berlin (ZIB), Takustr. 7, 14195 Berlin, Germany.
Parts of this work have been carried out within the DFG Research Unit: FOR 1498: “Alkali-Kieselsäure-Reaktionen in Betonbauteilen bei gleichzeitiger zyklischer Beanspruchung und externer Alkalizufuhr”.

References

[1] F. Weise, K. Voland, St. Pirskawetz, D. Meinel. Analysis of ASR-induced damage processes in concrete, Beton- und Stahlbetonbau 107 (12), pages 805-815, 2012.

[2] F. Weise, B. Maier, K. Ehrig. Analysis of damage processes in concrete induced by freeze thaw or freeze thaw salt cycles, Beton- und Stahlbetonbau 107 (12), pages 816-823, 2012.

[3] O. Paetsch, D. Baum, K. Ehrig, D. Meinel, S. Prohaska, Automated 3D Crack Detection for Analyzing Damage Processes in Concrete with Computed Tomography, Proceedings of ICT Conference Wels 2012, page 321-330.

[4] D. Neff, J. Harnisch, M. Beck, V. L’Hostis, J. Goebbels, D. Meinel, Combined examinations of iron oxides in the case of element corrosion and self - corrosion of steel in concrete, Materials and Corrosion , Vol 62, Issue 9, pages 861-871, 2011.

[5] C. Recknagel, J. Goebbels, D. Meinel. "Möglichkeiten der Strukturkennzeichnung von Asphalten mittels 3D-Computertomographie", Straße und Autobahn, Vol. 49. 2008, pp. 65-74.

2nd International Congress on 3D Materials Science
Edited by: Dominique Bernard, Jean-Yves Buffière, Tresa Pollock, Henning Friis Poulsen, Anthony Rollett, and Michael Uchic
TMS (The Minerals, Metals & Materials Society), 2014

3D MULTISCALE CHARACTERIZATION OF SILICA AEROGELS COMPOSITES

Anouk Perret[1]*, Geneviève Foray[1], Lucian Roiban[1], Karine Masenelli-Varlot[1], Eric Maire[1], Jérôme Adrien[1], Bernard Yrieix[2]

[1] MATEIS INSA de Lyon, UMR 5510, UCBL Lyon - 69621 VILLEURBANNE Cedex, France
[2] EDF R&D MMC Department, Avenue des Renardières - Ecuelles, 77818 MORET-SUR-LOING cedex, France

Keywords: silica aerogels, TEM, X-ray Tomography, characterization

Abstract

New composites based on a matrix of silica aerogel grains are currently being developed to answer the expectations of thermal renovation. One of the key parameters for their commercial use is the control of their porous network. In this study, we aim to propose a three-dimensional characterization from the nanometer to the millimeter scale of the silica aerogel particles themselves. Transmission electron microscopy (TEM) is used to characterize the mesoporous network within the aerogel grain. The arrangement in three dimensions of the grains and the voids within the aerogel grain pileup is investigated at the micron scale by X-ray tomography.

Introduction

The reduction of energy demand has become a global concern together with the development of green energies and the increase of energy efficiency. In France, to meet the national requirements on the reduction of the rejections of greenhouse gases, 75 % of the French buildings will need a thermal renovation. As the threshold stated for old and new buildings by standards keeps increasing, designing thinner and more efficient insulation materials is of great interest.

New insulating materials with thermal conductivities lower than the static dry air (25 mW / (m. K)), such as the recently developed silica aerogel-based products (15 mW / (m.K)) [1], are an interesting choice to answer those new functionalities. Indeed, silica aerogels exhibit simultaneously a high porosity (>80%) and small pores (<70nm). The Knudsen equation indicates that a material with pores smaller than the free path of molecules in the static air (70nm) will have smaller gas conductivity than air at ambient pressure:

$$\lambda g = \lambda g0 / (1+2A\ lm/\delta)$$

Where $\lambda g0$ is the thermal conductivity of the gas in molecular regime, A the gas characteristic constant, lm the mean free path of the molecules (air: lm = 70nm), and δ the material pore size.

Silica aerogels are available as granular materials. The grains have to be bound to each other, so that the material can be handled by professionals of thermal renovation. It has been previously shown that latex can be used as binder for the fabrication of stiff composite boards [2]. The binder used to design and shape the composite leads to a stronger mechanical behaviour (cohesion of the grains of silica aerogels between them). However, the binder has a tremendous conductivity and it will induce an unwanted increase of the overall thermal conductivity even at low volume fractions. An optimization of the proportions and the respective morphologies of both phases must thus be proposed to reach simultaneously the targeted thermal and mechanical

properties. The first step to reach the required low thermal conductivity lies in the control of the pore distribution of the silica aerogel grains. The second one is to finely tailor the porous network tortuosity so as to design an adequate fractal dimension. Once the grain itself is optimized, one has to ensure that the grain pileup is as dense as possible to reach the target thermal conductivity.

In this paper, we will study the pore distribution within the silica aerogel grains and pileups. First, Transmission Electron Microscopy (TEM) will provide information on the pores in an aerogel grain. Then, the grain pileup will be characterized by X-Ray Tomography.

Experimental

TEM

The transmission electron microscopy (TEM) analyses were performed on a Jeol 2010F microscope equipped with a field emission gun (FEG). Electron tomography was performed employing a JEOL 2100F microscope customized with a post-column GATAN Tridiem energy filter and a FEG. The sample under the form of a powder was dry deposited on a microscopy grid previously prepared for electron tomography. A droplet of suspension colloidal gold particles of 5 nm was previously played in the grid as fiducial markers. The tilt series were recorded automatically, using the GATAN tomography software in low dose bright field mode. Each tilt series were recorded in an angular range starting from -71° to +71° with an increment of 2.5° in Saxton scheme [3] during a total time of 45 minutes resulting in 81 images of 2048×2048 pixels with a pixel size about 0.16 nm. The alignment was performed whit IMOD software [4] and the volume was computed employing 15 iterations of algebraic reconstruction technique algorithm (ART) [5] implemented in TOMOJ/EFTETJ software [6] obtaining 512x512x512 pixels volumes. Finally the 3D visualization, surface rendering, pores size and silica particles quantification were performed combining different tools implemented in the software ImageJ, 3D Slicer and Chimera.

X-ray Tomography

Very detailed descriptions of this technique can be found in [7]. X-ray tomography is based on X-ray radiography, which allows the three-dimensional internal structure of a specimen to be determined non-destructively. When a X-ray beam passes through a sample, a radiograph can be formed, which is a projection of the absorption coefficients of the structures within the sample. Tomography involves rotating the sample about an axis perpendicular to the incident beam, and acquiring a series of radiographs at a sequence of angles. A filtered back-projection algorithm [8] can then be used to reconstruct the distribution of absorption coefficients within the volume of the sample. The result obtained after reconstruction is a regular array of the value of μ, the local attenuation coefficient of the X-rays measured for a cubic element of matter called a voxel (extension of the term pixel in 2D imaging). μ varies with the local composition and thus the internal structure of the sample can be determined without sectioning from this 3D regular map of μ. The resulting data can be analyzed to obtain 3D information about the microstructure.
As the final composite is composed of two grain sizes (D_{50} = 800 μm and 80 μm), in the first part of this paper, two grain sizes are considered (D50=800μm and d50 = 350μm) to be relevant

with the resolution of X-ray tomograph used. A Phoenix X-ray tomograph is used and the measurements are done on a stack of 1000 images.
Several parameters can be used to characterize a porous network and hence the quality of the pileup. Tortuosity can be defined as:

$$T = \frac{minimum\ path\ length\ from\ one\ side\ of\ the\ image\ to\ another\ side\ in\ the\ phase\ selected\ (\mu m)}{straight\ path\ length\ form\ one\ side\ to\ another\ side\ (\mu m)}$$

As two phase are of concern within a super-isolant material, we have to measure on the hand pore or static air network tortuosity, and on the other hand skeleton (i.e aerogel grain network) tortuosity.

Results and discussion

Porous network in a single aerogel grain

Figure 1a shows a projection at 0° extracted from the tilt series acquired in TEM. The silica particles appear in dark grey. It is noteworthy that, compared with the images acquired with X-ray tomography and shown in the next part, the contrast is reversed and silica grains are dark in TEM. The signal-to-noise ratio (SNR) is clearly poor. This is due to the fact that the silica aerogels are very beam sensitive and employing an intense electron beam would considerably damage the sample. Anyway the signal is strong enough to provide a good volume and a cross section trough the XY plane is showed in Figure 2b. By selecting the grey levels, the volume was segmented and a silica surface rendering is showed in the Figure 2c. The resolution, in the range of a few nanometers, allows the observation and quantification of the porous structure of the grain. A bimodal distribution is evidenced, with pores of 10 nm and 30 nm in diameter. Those sizes are in agreement with the results obtained from BET measurements. The tortuosity of the pore network was measured equal to 1.27.

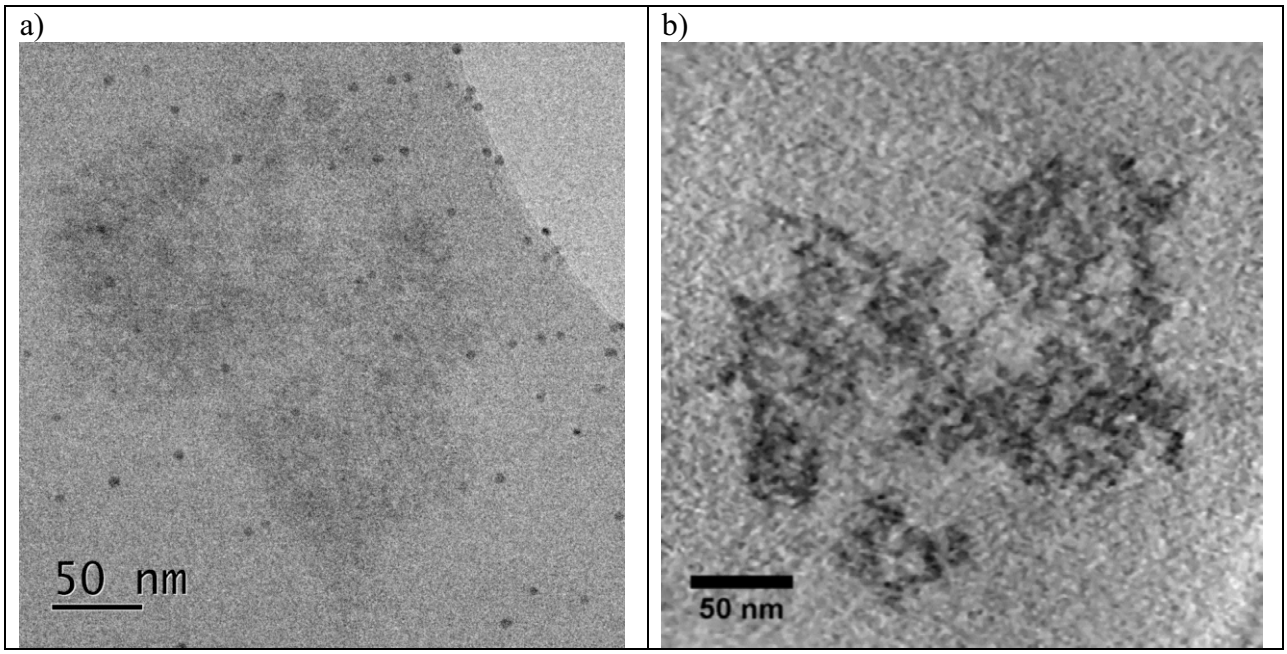

c)

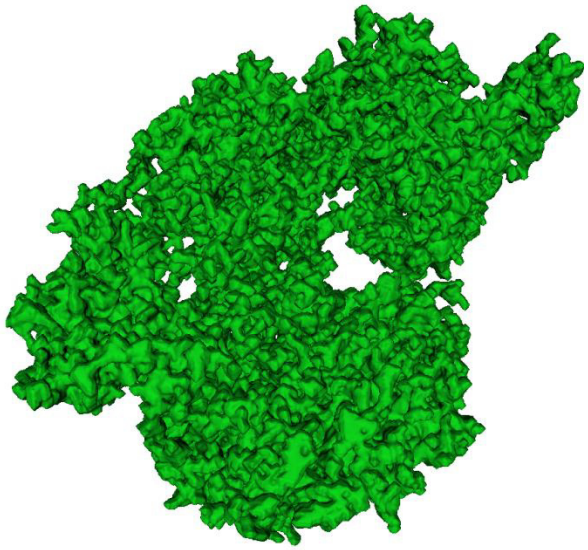

Figure 1: Silica particle a) Projection extracted from the tilt series at 0° ; b) Cross section extracted from the calculated trough the XY plane; c) 3D model of one silica aerogel particle

Characterization of the grain pileup

Figure 2 displays slices of the tomograms obtained on granular arrangements with different grain sizes. As the reconstructed image represent the absorption coefficient of the material observed, the aerogels grains are in light grey and the air is dark grey (small or no absorption). Some of the grains are lighter than others (white grains), which may due to various densities of the aerogels grains, caused in turn by the lack of hydrophobous particles on silica surfaces during synthesis. These different densities may arise from the quite complex sol-gel drying process. These different densities are confirmed with the naked eye also as most silica aerogel grains are transparent but some are white or translucent. As the volume fraction of those non porous grains was small (<10%), the properties of the whole pileup was not affected.

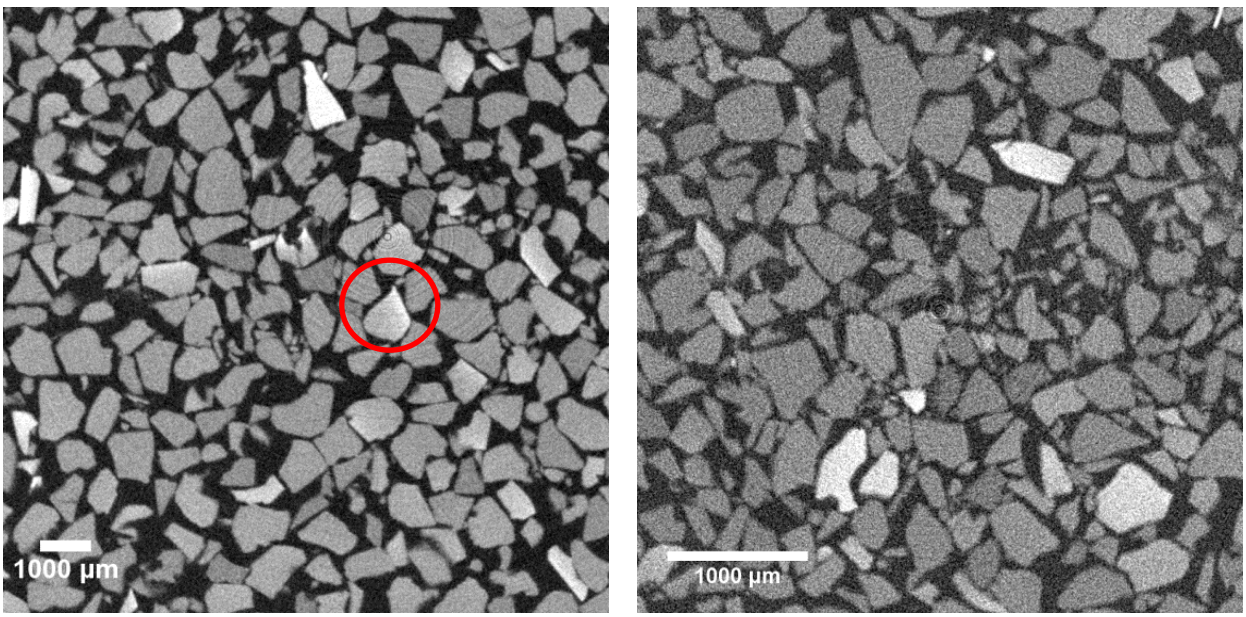

a) b)

Figure 2: tomographic slice for the two samples of silica aerogel grains
a) Aerogel grain size D_{50} = 800µm, resolution = 15µm image size=15 mm*15 mm
b) Aerogel grain size D_{50}=350µm, resolution = 4,3µm, image size = 4.3mm*4.3 mm

X-ray tomography allows observing the morphology and geometric features of the silica aerogel grains. As expected by the preparation process (sieving) they are not spherical but exhibit polyhedral shapes with sharp edges.
Static air tortuosity is measured on segmented 3D images. It is equal to 1.2 for the pileups composed of either small grains (figure 1b) or large grains (figure 1a). In such calculations, the aerogel grains themselves are considered as airtight since the tortuosity inside the grains has not be taken into account.

Moreover, considering the polyhedral shape, the compacity of the pileup – parameter defined as the volume ratio between silica and the air - cannot be as high as if the grains were spherical. The compacity measured on both images on figure 1 is around 60% and the thermal conductivity is 18mW/(m.K) (mean value). This compacity is not as high as expected. To increase this value, one could consider the addition of smaller silica aerogel grains with the biggest grains. The compacity of such pileup (not shown here) has been measured around 80%. This should undoubtedly increase the tortuosity of air as well since the thermal conductivity is lowered around 15 mW /(m.K).

Conclusions

In this study, tomography was used to characterize the porous structure of single silica aerogel grains and pileups. X-ray and electron tomography clearly give complementary pieces of information. The observation and quantification of the porous structure inside a single grain have been carried out by electron tomography. The grain pileup has been characterized by X-ray tomography and values of tortuosity and compacity have been deduced from the tomograms. Such methodology will permit a better modeling of the insulation properties of aerogel based materials.

Acknowledgments

The authors are grateful to CIFRE organism for the financial support of the Phd grant and thank the ADEME and EDF for being involved in this project.
The authors also acknowledge the METSA network for the financial support of the electron tomography experiments. We are also grateful to Prof. Ovidiu ERSEN for the access to the microscope and for fruitful discussions.

References

1. A. Bisson , A.R., D.Lecomte, P.Achard, *Effective thermal conductivity of divided silica xerogel beds.* non crystalline solids, 2004. **350**: p. 379-384.
2. B.Yrieix , B.M., G.Foray , A.Bogner, *Materiau super-isolant à pression atmospherique à base d'aerogel*. Patent FR 2975691 WO2012168617, 2011: france.
3. W. Saxton, W.B., M. Hahn, *Three dimensional reconstruction of imperfect two dimensional crystals* Ultramicroscopy, 1984. **13**: p. 57-70.
4. JAMES R. KREMER, D.N.M., AND J. RICHARD McINTOSH, *Computer Visualization of Three-Dimensional Image Data Using IMOD.* journal of structural biology, 1996. **116**: p. 71-76.
5. R. Gordon, R.Bender, G.T. Herman, *Algebraic reconstruction techniques (ART) for Three-dimensional Electron Microscopy and X-ray photography*, Journal of Theoretical Biology, 1970. **29**: p. 471−481.
6. Cédric MessaoudiI, T.B., Carlos Oscar Sanchez Sorzano and Sergio Marco, *TomoJ: tomography software for three-dimensional reconstruction in transmission electron microscopy.* BMC Bioinformatics, 2007. **8**: p. 288.
7. Eric Maire , P.C., Jerome Adrien , Laurent Babout , Lisa Biasetto, *Characterization of the morphology of cellular ceramics by 3D image processing of X-ray tomography.* european ceramic society, 2007. **27**: p. 1973-1981.
8. L. A. Feldkamp, L.C.D., J. W. Kress, *Practical cone beam algorithm* Journal of the optical Society Of America A, 1984: p. 612.

2nd International Congress on 3D Materials Science
Edited by: Dominique Bernard, Jean-Yves Buffière, Tresa Pollock, Henning Friis Poulsen, Anthony Rollett, and Michael Uchic
TMS (The Minerals, Metals & Materials Society), 2014

GEOMETRIC AND MECHANICAL MODELING OF FIBER-REINFORCED COMPOSITES

Heiko Andrä[1], Martin Gurka[2], Matthias Kabel[1], Sebastian Nissle[2], Claudia Redenbach[3], Katja Schladitz[1], Oliver Wirjadi[1,*]

[1]Fraunhofer ITWM, 67663 Kaiserslautern, Germany
[2]Institut für Verbundwerkstoffe IVW, 67663 Kaiserslautern, Germany
[3]University of Kaiserslautern, 67663 Kaiserslautern, Germany
[*]Corresponding author, e-mail: wirjadi@itwm.fraunhofer.de

Keywords: Composites, Glass fiber-reinforced polymer, image analysis, modeling, simulation, mechanical properties

Abstract

Micro-computed tomography (μCT) yields three dimensional reconstructions of the microstructures of materials down to a spatial resolution of about 1 μm. Based on the resulting image data, many mechanically relevant geometric parameters can be computed using three dimensional image analysis. These parameters include fiber density, orientation, homogeneity and thickness. We show how to fit stochastic fiber models to this image data. Such models take into account fiber densities, orientations, radii and inhomogeneities. These geometries can be realized, thus enabling numerical homogenization methods based on the Lippmann-Schwinger equations in elasticity. These yield the full elastic tensor and even nonlinear elastic behavior. With appropriate damage models, the material strength can be characterized. Such an approach has various advantages over mechanical testing. For example, it characterizes a material in every direction, instead of only the direction in which a tensile test was performed. Furthermore, material models open the path to virtual material design, where one can use computer experiments to identify the microstructural geometry which best fulfills the requirements in some given application. In this contribution, we demonstrate the entire chain consisting of image analysis, geometric and mechanical modeling for glass fiber-reinforced thermoplastics.

Introduction

Many modern materials possess complex microstructures, which can be characterized using various imaging techniques. Apart from classical sectioning techniques, especially the use of micro-computed X-ray tomography (μCT) has fostered the developed of highly specialized, three dimensional material characterization algorithms. These methods encompass the analysis of open and closed foams (e.g. [1, 2, 3]) and of fiber-reinforced materials (e.g. [2, 4, 5, 6, 7]) and are available for routine use in software packages such as MAVI (Fraunhofer ITWM, Germany). Based on these analysis tools, suitable models for microstructures are also available for many material classes like open and closed foams (e.g. [8]) and fiber-reinforced polymers (e.g. [9]). These are stochastic geometrical models which capture the essential properties of a microstructure using only few parameters, and which can be fit using results from image analysis based on tomographic reconstructions. Starting from realizations of such models, FFT-based methods can be used to predict e.g. macroscopic mechanical behavior depending on the geometrical model's parameters. We show how to combine these tools into one chain.

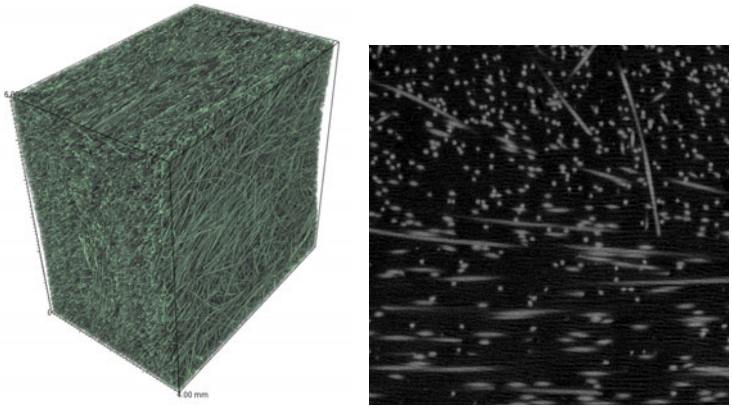

(a) Volume rendering (b) Slice at interface

Figure 1: Centrally in the investigated material, there exists an inner layer, where fibers are oriented away from the injection direction. Some fibers cross the interface between the regions.

Material

For the present paper, we focus on an injection molded specimen with 30 wt% glass fiber content in a polypropylene (PP) matrix, see Fig. 1. The average fiber length is 7 mm with a diameter of about 16 μm. The specimen was injection molded to a type 1A shouldered test bar with an injection rate of 10 mm/s. Mechanical tests have been performed in accordance with DIN EN ISO 527-1 to -5. Furthermore, a CT-reconstruction with 4 μm pixel distance was produced, which we have previously analyzed to describe the micostructure of this specimen, see [7] for details. The following table summarizes the main known properties of this specimen.

Fiber weight content	30 wt%	Mean fiber length	7 mm
Fiber volume content	13 vol%	Matrix	PP
Tensile modulus	6 GPa	Elongation at break	2.5 %

Image Analysis

The fiber directions were obtained from the CT-scan using MAVI 1.5 beta (Fraunhofer ITWM) as described in [7]. In brief, let $B \subset \mathbb{R}^3$ denote the set of pixels belonging to the fiber system, which can be estimated by a simple image binarization. For every point $x \in B$, the Hessian matrix of second partial derivatives was computed, and the eigenvector $v(x)$ to the smallest eigenvalue of that matrix was used as an estimate for the local fiber direction. This results in a three dimensional vector field on B. By averaging over these points, we can estimate the second order fiber orientation tensor [10] of the fiber system as

$$T = \sum_{x \in B} v(x) \otimes v(x). \tag{1}$$

In [7], we evaluated T for different regions of the specimen and found that the material consists of several regions with different fiber direction distributions. In the outer layers, the fibers are well aligned with the injection direction, but there also exists a misoriented fiber layer centrally in the specimen. This area has a thickness of 2 mm [7].

Stochastic geometric modeling

To model the fiber system in this material, we will use a stochastic process of non-overlapping cylinders. We will show how almost all parameters of this model (with the exception of the fiber length) can be fit either from the results of our image analysis outlined above, or from known material parameters. We start with the fiber directions. The direction distribution of the fibers is modelled by the parametric density

$$f(\theta, \phi) = \frac{1}{4\pi} \frac{\beta \sin \theta}{(1 + (\beta^2 - 1)\cos^2 \theta)^{3/2}},$$

where $(\theta, \phi) \in [0, \pi) \times [0, 2\pi)$ are the spherical coordinates of a unit vector in $\mathbb{R}^3$. The parameter $\beta > 0$ is an anisotropy parameter: $\beta = 1$ results in a uniform distribution on the sphere, $\beta > 1$ describes a girdle distribution with principal plane in the xy-plane, and $\beta < 1$ describes a bipolar axial model whose principal axis is the z-axis. Other principal directions can be obtained by suitable rotation of the direction vectors.

The parameter β can be estimated from a sample of unit vectors using a maximum likelihood (ML) approach. Since no closed form solution of the maximum of the likelihood function exists, the ML estimator has to be computed numerically, see [11] for details. As input to this ML estimator, we used the local fiber direction vectors $\{v(x)|x \in B\}$ as described above, and fit three different direction distributions for the two outer layers and for the inner, misoriented layer in the specimen. The estimated parameters are given in the following table.

Top layer	$(\hat{\beta}^{\text{top}}, \hat{\theta}^{\text{top}}, \hat{\phi}^{\text{top}})$	=	$(0.17, 1.68, 1.57)$
Central layer	$(\hat{\beta}^{\text{central}}, \hat{\theta}^{\text{central}}, \hat{\phi}^{\text{central}})$	=	$(0.34, 0.12, 0.13)$
Bottom layer	$(\hat{\beta}^{\text{bottom}}, \hat{\theta}^{\text{bottom}}, \hat{\phi}^{\text{bottom}})$	=	$(0.16, 1.64, 1.58)$

Random sequential adsorption (RSA) of cylinders has previously been proposed as a suitable model for fiber-reinforced polymers. Yet, the material investigated here is inhomogeneous, i.e., the fibers do not follow the same distribution everywhere in the specimen. Specifically, the fiber direction distribution changes in the inner layer of the material. Therefore, we propose a modification of the original RSA algorithm to account for such spatial inhomogeneities while still guaranteeing non-overlapping objects and an unbiased representation of the model's parameters. To this end, let $W_i \subset \mathbb{R}^3$ denote $i = 1, 2, \ldots, n$ non-overlapping regions. For our purpose, we use cuboidal regions. The region-RSA algorithm works as follows:

1. Choose a region k probability p_k according to the volume of the regions, i.e., $p_k = \text{vol}(W_k)/\sum_i \text{vol}(W_i)$.

2. Draw a direction $v \in S^2$ from the direction distribution fit to the region k as described above. Also, draw a fiber length l and fiber radius r from previously chosen distributions (which may differ between regions). Together, this defines a cylinder in the origin.

3. Independently draw a coordinate $x \in W_k$ from a uniform distribution in W_k. Shift the cylinder from step 2 to x.

4. Test if the shifted cylinder from step 3 intersects any previously inserted cylinder. Note that here, we test against all cylinders, not just those with center in W_k. If no overlap is detected, insert the cylinder into the model and proceed to step 1.

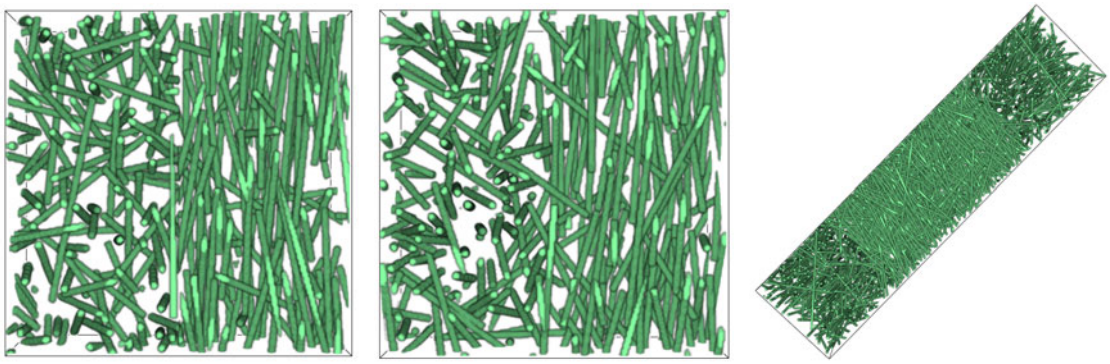

(a) Interface of two stacked RSA (b) Interface of region-RSA (c) 3-layered region-RSA model

Figure 2: In thin slices (200 μm), the advantages of our new region-RSA over stacking two conventional RSA realizations are visible. To model the material in this contribution, we modeled 3 layers, where each layer's parameters were fit to the results from image analysis.

5. Repeat steps 3 and 4 for a maximal number of $T > 0$ trials. If the cylinder from step 2 could not be inserted in W_k after T trials, stop.

In this variant, the algorithm runs until reaching the maximal filling limit for the given value of T. In practice, of course, we also add a check for the current volume density, which allows us to stop the modeling when reaching the desired density. Note that our region-RSA inherits all properties from the original RSA since once an object was realized in step 2, it will either insert it into the model, or terminate. Furthermore, since we test against all objects in the model, not only those in the current region W_k in step 4, this algorithm results in natural interfaces between adjacent regions, see Fig. 2.

Effective elastic properties

For the homogenization of a heterogeneous, periodic medium with local stiffness $C(x)$ we solve periodic boundary value problems (BVP) for the displacement fluctuations u^* on a rectangular cuboid $\mathbb{T}^d = \mathbb{R}/L_1\mathbb{Z} \times \cdots \times \mathbb{R}/L_d\mathbb{Z}$ which is often called unit-cell, statistic or representative volume element:

$$\begin{cases} \operatorname{div} \sigma(x) = 0, & x \in \mathbb{T}^d, \\ \sigma(x) = C(x) : \epsilon(x), & x \in \mathbb{T}^d, \\ 2\epsilon(x) = 2E + \operatorname{grad} u^*(x) + (\operatorname{grad} u^*(x))^T, & x \in \mathbb{T}^d, \\ u^*(x) \quad \text{periodic}, & x \in \partial\mathbb{T}^d, \\ \sigma \cdot n(x) \quad \text{anti} - \text{periodic}, & x \in \partial\mathbb{T}^d. \end{cases}$$

For all constant strains E, this problem is uniquely solvable in the space $[H^1_{\#}(\mathbb{T}^d)]^d$. With the use of the energy equivalence principle

$$\frac{1}{2} \langle \epsilon_i(x) : C(x) : \epsilon_j(x) \rangle_{\mathbb{T}^d} = \frac{1}{2} \langle \epsilon_i(x) \rangle_{\mathbb{T}^d} : C_{\mathit{eff}} : \langle \epsilon_j(x) \rangle_{\mathbb{T}^d} \tag{2}$$

it is possible to determine the effective (homogeneous) stiffness C_{eff} by solving the BVP for any basis of the six dimensional space of macroscopic strains E.

Lippmann-Schwinger equation By introducing a *reference material* of homogeneous stiffness C^0 and the *polarization* $\tau(x) = (C(x) - C^0) : \epsilon(x)$, the constitutive equation for the *stress* $\sigma(x) = C(x) : \epsilon(x)$ can be transformed as follows $\sigma(x) = C^0 : \epsilon(x) + \tau(x)$. For known residual stresses $\tau(x)$ the solution of $\operatorname{div} \sigma(x) = 0$ can be expressed by using the nonlocal elastic *Green operator* Γ^0 for strains associated with the reference material C^0, i.e. $\epsilon(x) = E - (\Gamma^0 * \tau)(x)$, where the convolution is defined by $(\Gamma^0 * \tau)(x) = \int_{\mathbb{T}^d} \Gamma^0(x - y) : \tau(y) dy$. By combining the previous equations we obtain the *Lippmann-Schwinger equation* [12]

$$\epsilon + \Gamma^0 * \left(\left(C - C^0 \right) : \epsilon \right) = E.$$

This equation is numerically solved by the so called *basic scheme* [13] which relies on fast Fourier transformations (FFT).

Results

In this section, we put together all tools introduced above to present a chain which we call "virtual material design". First, we verify our mechanical model using the CT image data: We binarized the CT-reconstruction such that the volume fraction of the foreground (fiber component) reached the specimen's theoretical fiber content of 13 vol%. There, we first compare Young's modulus in fiber injection direction (x_2) between results from mechanical testing and simulation as outlined above. Next, we studied a preliminary geometric model, which consisted of three layers of fibers oriented as in the CT-reconstruction and with approximately 13 vol% fiber fraction (Fig. 2(c)). As noted above, we cannot model the fibers at their original lengths, and therefore generated two models with 1 mm and 0.75 mm fiber length, respectively.

Mechanical test	$E_2 = 5.99$ GPa $\pm$ 0.19 GPa
Simuation (binarized μCT-image)	$E_2 = 5.68$ GPa
region-RSA model (3 layers, 0.75 mm fiber length)	$E_2 = 4.06$ GPa
region-RSA model (3 layers, 1.00 mm fiber length)	$E_2 = 4.09$ GPa

In contrast to the prediction based on the binarized CT-image, the mechanical properties of our region-RSA model are far off the true material's properties – for both tested fiber lengths.

Discussion

We have summarized tools from image analysis, stochastic modeling and mathematical homogenization, and we have proposed an extension of the random sequential adsporption (RSA) algorithm. This extension (region-RSA) allows to realize models of structures with different statistical properties in different areas. Based image analysis results, we were able to demonstrate how to fit such a region-RSA model to a μCT-reconstruction. The stiffness computed on this model realization was not close to results from mechanical testing. One possible reason is our simple three layer model: The true material has an inner core with a thickness of about 2 mm, just as the model realization. But, in the GF30-specimen, this inner misoriented layer does not span the entire width – in contrast to our model geometry, cf. Fig 2(c). Another possibility is that the anisotropy of the fiber system is under-estimated due to noise and missing resolution. A study using a larger model is currently under way.

Acknowledgment

This work was supported by "Innovationszentrum Applied System Modeling for Computational Engineering (ASM4CS)".

References

[1] C. Lautensack and T. Sych. 3d image analysis of open foams using random tessellations. *Image Analysis & Stereology*, 25(87-93), 2006.

[2] C. Redenbach, A. Rack, K. Schladitz, O. Wirjadi, and M. Godehardt. Beyond imaging: on the quantitative analysis of tomographic volume data. *International Journal of Materials Research*, 103(2):217–227, 2012.

[3] A. Liebscher and C. Redenbach. Statistical analysis of the local strut thickness of open cell foams. *Image Analysis & Stereology*, 32(1), 2013.

[4] H. Altendorf and D. Jeulin. 3d directional mathematical morphology for analysis of fiber orientations. *Image Analysis & Stereology*, 28(3), 2011.

[5] M. Krause, J. M. Hausherr, B. Burgeth, C. Herrmann, and W. Krenkel. Determination of the fibre orientation in composites using the structure tensor and local x-ray transform. *Journal of Materials Science*, 45(4):888–896, 2010.

[6] D. Salaberger, K. A. Kannappan, J. Kastner, J. Reussner, and T. Auinger. Evaluation of computed tomography data from fibre reinforced polymers to determine fibre length distribution. *International Polymer Processing*, 26(3):283–291, 2011.

[7] O. Wirjadi, M. Godehardt, K. Schladitz, B. Wagner, A. Rack, M. Gurka, S. Nissle, and A. Noll. Characterization of multilayer structures in fiber reinforced polymer employing synchrotron and laboratory x-ray ct. *International Journal of Materials Research*, accepted for publication, 2014.

[8] Claudia Redenbach. Microstructure models for cellular materials. *Computational Materials Science*, 44(4):1397–1407, 2009.

[9] Claudia Redenbach and Irene Vecchio. Statistical analysis and stochastic modelling of fibre composites. *Composites Science and Technology*, 71(2):107–112, 2011.

[10] Suresh G. Advani. The use of tensors to describe and predict fiber orientation in short fiber composites. *Journal of Rheology*, 31(8):751, 1987.

[11] J. Franke, C. Redenbach, and N. Zhang. On a mixture model for directional data on the sphere. *In preparation*.

[12] R. Zeller and P. H. Dederichs. Elastic constants of polycrystals. *Physica Status Solidi (b)*, 55(2):831–842, 1973.

[13] H. Moulinec and P. Suquet. A numerical method for computing the overall response of nonlinear composites with complex microstructure. *Computer Methods in Applied Mechanics and Engineering*, 157(1-2):69–94, 1998.

2nd International Congress on 3D Materials Science
Edited by: Dominique Bernard, Jean-Yves Buffière, Tresa Pollock, Henning Friis Poulsen, Anthony Rollett, and Michael Uchic
TMS (The Minerals, Metals & Materials Society), 2014

HIGH RESOLUTION MICRO CT IMAGING AND 3D IMAGE ANALYSIS OF PAPER PRODUCTS

Y. Sharma[1, 2], A.B. Phillion[2], M. Martinez[1, 3]
[1]Department of Mechanical Engineering, The University of British Columbia, Vancouver, Canada.
[2]Okanagan School of Engineering, The University of British Columbia, Kelowna, Canada.
[3]Department of Chemical and Biological Engineering, The University of British Columbia, Vancouver, Canada

Keywords: Micro CT, Fibre Segmentation, Paper microstructure

Abstract

Characterization of the internal microstructure of paper, consisting of a dense network of wood fibres, is an important tool for determining the properties of paper and for optimizing the papermaking process. A novel two step approach for segmentation of wood fibres in high resolution micro CT images of paper has been developed that is able to isolate the individual wood fibres even with cracks and openings in their fibre walls, and is thus a first step in quantifying the fibrous microstructure of paper. The approach uses an extended 2D connected components method to track the lumen or hollow within the fibre in a fully automated manner, followed by labeling of the fibre walls using a distance transform. The result is a robust 3D fibre segmentation that preserves the surface topology of the papermaking fibres.

1. Introduction

Paper, consisting of cellulose pulp derived from wood, is one of the most common natural materials used in daily life. A key step in papermaking is the refining process, which modifies the fibre morphology. During processing, the fibres are refined to increase their specific surface area and flexibility through the imposition of a cyclical force in rotary devices called refiners. The resulting fibre network and the inter-fibre void spacing constitute the paper architecture and determine its final properties. Most end-use properties of paper, including tensile strength, opacity, and printability, depend on the uniformity of the paper structure described by the mass distribution in the range 1 μm to 10 mm [1]. At present, relatively few studies of paper structure have been carried out at the micro-scale on material in the post-refined state. This is because the measurement techniques are limited and tedious. Much of the previous work (e.g. [2]-[4]) has involved the use of optical microscopy, scanning-electron microscopy, or confocal microscopy. The results have demonstrated the benefits of characterizing the structure of paper, such as measurement of the surface profile, porosity, mass, and coating thickness (in the case of coated papers). Confocal microscopy has been particularly revealing to show the connectivity and entanglement between fibres, although the work has been limited to a depth of ~ 50 μm below the surface [4]. Unfortunately, these techniques are either not capable of viewing the entire 3D structure, or they change the structure during sample preparation and/or visualization.

X-ray tomographic microscopy is a novel direct and non-invasive visualization technique for acquiring high-resolution 3D images in order to precisely characterize the internal microstructure

of a wide range of materials. At present, only a few limited studies have been carried out using μCT to investigate paper structure [5-11]. These works have illustrated the need for good post-processing capabilities owing to the complexity of the paper structure. Advanced image analysis techniques are required to characterize the dense network of wood fibres, i.e. fibre orientation, length, and connectivity, in μCT images of paper. One of the major tasks is the segmentation of individual fibres. Papermaking fibres are thin, hollow structures with varying cross sections and the fibres have holes in the walls to enable fluid transport. Moreover, the fibres may be kinked, curled, twisted, and/or otherwise damaged, making segmentation extremely difficult. Segmentation of papermaking fibres has been previously attempted [7-11] using manual or semi-automatic methods including Gradient Vector Flow (GVF) snakes [12], 3D vector path estimation [7], and Ordered Region Growing [13]. While these methods have shown an ability to segment individual paper fibres, they all require the user to initiate the segmentation by selecting seed points in one or more slices. The sheer size of data makes such semi-automatic techniques impractical for identifying the thousands of fibres within a paper specimen. In this work, a new approach for automated segmentation of wood fibres in μCT images is presented.

2. Image Acquisition

3D images of paper samples known as handsheets have been acquired using an Xradia MicroXCT-400 X-ray tomographic microscope at a spatial resolution (voxel size) of 0.58 μm. Unlike many other engineering materials, cellulose fibres offer extremely low attenuation to X-rays, resulting in poor contrast at the fibre-air interface. To offset the poor contrast, an exposure time of 30 s for each of the 2500 radiographs was utilized, leading to high signal-to-noise ratio. The total scan time was 24 hours. In initial scans, sample instability was observed, due to either fluttering caused by the stage rotation and/or fibre expansion due to temperature and humidity changes, resulting in streaking artifacts. Flutter was minimized by imaging only a tiny cross-section of paper (~1 mm^2) resulting in a dataset of 1932x1946x364 voxels. Thermal and humidity stability were achieved by placing the sample inside the chamber a few hours prior to the scan.

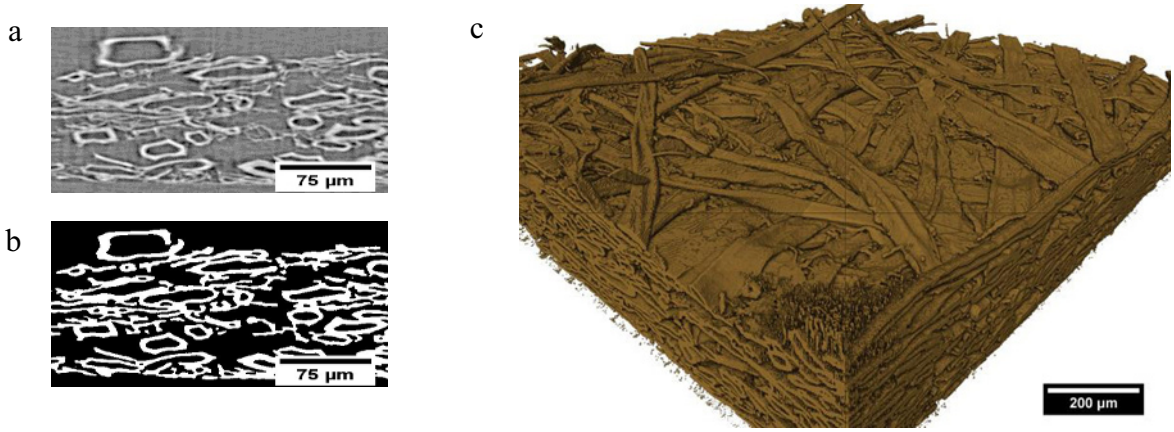

Fig.1: Initial Segmentation (a) 2D Cross-section view of a handsheet; (b) Binarised slice with white pixels corresponding to the fibre walls; (c) Volume rendering of the binarised data.

3. Image Analysis

3.1 Initial Segmentation

A typical cross-sectional slice of as-scanned data is shown in Figure 1(a). It can be seen that the image is characterized by poor contrast and streaking artefacts. The ring shaped objects are the fibre walls, the hollows inside are called lumens, and the rest of the space is filled with air. There is no intensity difference between the lumen and air and the fibre walls also have only a slightly higher gray scale value. Poor contrast makes de-noising challenging, as there is a high risk of smoothing and joining of individual fibres. Thus, only a simple non-linear diffusion filter [14] was applied to efficiently reduce noise while maintaining the fibre boundaries.

To segment individual fibres, the 3D images must first be segmented into two phases- fibre and pore; known as binarisation or initial segmentation. Although the diffusion filter sharpens the histogram as shown in Figure 2(a), selecting a hard threshold for binarisation is challenging due to poor contrast at the fibre-pore interface. Statistical methods cannot be relied upon for calculation of the fibre wall thickness, a critical parameter of study, since it is highly sensitive to the value of the threshold. Instead, the physical basis weight (i.e. the weight of fibres per unit surface area) was used as a measure of the best estimate for a hard threshold. This eliminates the need for complex statistical analysis and also provides a reliable estimate of the fibre wall thickness. The threshold T is estimated by comparing the calculated basis weight of the 3D image for a given value of T against the measured experimental value of ~70 g/m^2. As can be seen in Figure 2(b), a low (high) value of *T* leads to an over (under) estimation of fibre wall thickness and in turn the basis weight. A cross-section view of the best-case binarisation is shown in Figure 1(b) and a volume rendering of the binarised data is shown in Figure 1(c).

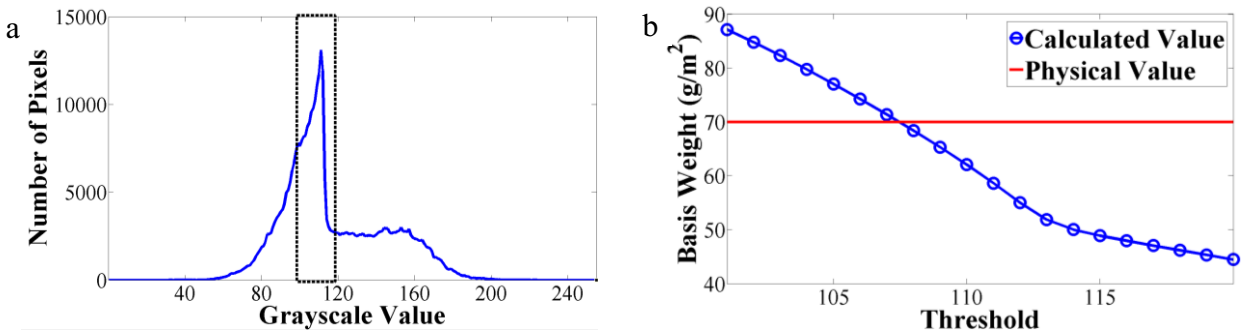

Fig. 2: (a) Histogram after Anisotropic Diffusion Filtering. Basis weight is calculated for each value of T within the range denoted by the rectangle; (b) Plot of calculated basis weight as a function of T.

3.2 Fibre Segmentation

Lumens are used as markers for fibre segmentation since direct segmentation of the fibre walls appears impractical due to the considerable fibre-fibre contacts. Axelsson [11] presented a novel method for segmentation through tracking of the lumen by growing them in the direction of their local orientation. Although efficient, this method required user initiated seeding points. Given the enormity of data (~20,000 fibres per image), there is a need for a segmentation technique that

has low computational complexity and autonomy. The major challenges relate to the fibre wall discontinuities, since standard methods will fail by merging the lumens with the background. The new fibre segmentation process is divided into two steps: lumen tracking followed by fibre wall extraction.

Lumen Tracking: The lumen tracking algorithm is an extension of the standard Connected Component (CC) labeling technique. CC labeling is a low-level segmentation technique that groups regions in an N-dimensional image on the basis of their connectivity. Given a binary image, CC labeling groups the white region into disjoint blobs such as there is no path of connecting white elements between any two blobs. Ideally, 3D CC labeling on the volume should be able to isolate the lumens; however, even a single pore throughout the length of a lumen will merge it with the background. Moreover, fibres are open at the beginning and termination, also allowing for merging with the background. A 3D CC labeling on the volumetric data is thus only able to segment those lumens that have no pores and run the length of the volume. This renders the 3D CC labeling impractical for the purpose of segmenting papermaking fibres.

The proposed methodology takes advantage of the fact that although the 3D lumen geometry is not closed, the lumen cross-sections are closed 2D shapes in most of the slices; the lumen will only merge with the background on slices where pores are located. A 2D CC labeling process is applied to each slice, individually labeling all the lumen cross sections separately except for those lumens which have a pore in the fibre wall in that slice. The labels from adjacent slices are then connected together based on their location in order to create the 3D structure of the lumen. The major challenges are in defining the end point of a lumen and preventing leakage through the pores. This is realized by using information from adjacent slices as follows. While tracking the lumen, if the size of its cross section appears to have increased significantly and suddenly in one of the slices, the lumen may either have a pore in that slice or may have ended in the preceding slice. If, after a few slices, the cross section regains its shape, it was a pore and the slices in between are filled through averaging. If the cross section does not regain its shape within a few slices, the lumen is deemed to have ended. The algorithm is thus able to track lumens despite discontinuities in their fibre walls, providing a significant advantage over 3D CC.

Fibre Wall Extraction: The lumen-tracking algorithm presented in the previous section provides a complete three-dimensional segmentation of the lumens in the volume. These segmented lumens are then used as markers for extracting the fibre walls. The fibre wall surrounding each segmented lumen is assigned the same label as the internal lumen. A distance transform (DT) [15] is used to separate fibre walls from two adjoining fibres that are in contact. Since DT automatically finds the lumen closest to each pixel, the boundary between touching fibres can be easily defined. Through use of this methodology, a robust segmentation of the fibre walls is achieved while preserving the surface topology of the papermaking fibres.

4. Results and Validation

The segmentation algorithm has been implemented in MATLAB, and the output is a structured array containing the coordinate information of all the segmented fibres. Visualization of the structure has utilized the tools available within the Avizo. An example result is shown in Figure

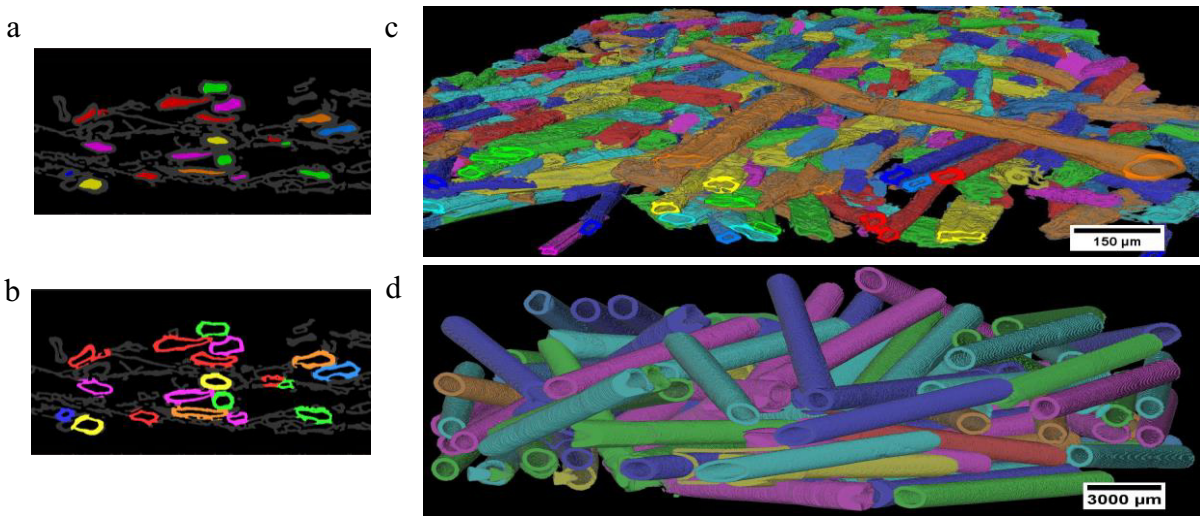

Fig.3 (a) 2D section showing segmented lumen (colored regions) overlaid on the original slice (grey); (b) Segmented Fibres overlaid on the original slice; (c) 3D image showing separate labels for each fibre; (d) Validation of the code via segmented aluminum tubes.

3. Segmented lumens and fibre walls are overlaid on top of the original data in Fig. 3(a) and (b) respectively while Fig. 3(c) is a volume rendering of the segmented fibres where each color represents a different lumen. As can be seen, the newly developed technique is able to individually identify large numbers of papermaking fibres that have variable lengths with holes, kinks and other features. This segmentation was performed in a fully automated process, taking approximately 3.5 hours for identifying ~1000 fibres in a 1 mm^2 paper specimen. However, as can be seen, not all fibres can be segmented. The fibre fragments that have been crushed and squeezed against each other during processing, resulting in their lumen becoming collapsed, are almost impossible to separate one from the other.

In comparison to previous lumen tracking methods (e.g. [10]), the new method is considerably faster. The technique has been validated by demonstrating successful segmentation of aluminum tubes in a pseudo paper like network structure. 136 hollow aluminum tubes (2 mm. in diameter and 10±0.5 mm. long) were embedded in epoxy and imaged using µCT to obtain 3D data similar to that of paper. The algorithm is able to successfully segment the tubes and calculate the length of each tube. The segmented data is shown in Fig. 3(d) where each color denotes a different tube. The average length of the segmented tubes is found to be 9.5 mm. (σ = 1 mm.), a value that is close to the true length of the tubes within limits of numerical error.

5. Conclusions

A method for fast, efficient and robust segmentation of hollow fibrous structures has been presented and successfully applied to high-resolution µCT images of papermaking fibres. The technique is extendable to any problem involving segmentation of complex, elongated shapes. The segmented fibres will be used for calculating fibre parameters such as their lengths, orientations, along with network parameters such as the coordination number of fibre-fibre intersections. The 3D geometry thus obtained can be directly used for numerical modeling.

Future work will involve validation of the algorithm by segmentation of aluminum tubes of known length with pores, cracks, and twists that approximate wood fibres.

Acknowledgements

The authors would like to thank Canfor Pulp Limited Partnership and NSERC for funding this work.

References

1. R. Allem, and T. Uesaka, “Characterization of paper microstructure: a new tool for assessing the effects of base sheet structure on paper properties” (Paper presented at Advanced coating fundamentals symposium, Toronto, Canada, 1999), 111-120.
2. D.H. Page, and H.W. Emerton, “The microscopic examination of paper, and wood – Improved methods for the study of surfaces,” Svensk Papperstidning, 62 (9) (1959), 318-332.
3. R. Allem, “Characterization of paper coatings by scanning electron microscopy and image analysis,” J. Pulp Paper Science, 24 (10) (1998), 329-336.
4. A. Goel, E.S. Tzanakakis et al., “Confocal Laser Scanning Microscopy to Visualize & Characterize the Structure of Paper,” AIChE Symp. Series, 96 (324) (2000), 75-79.
5. E.J. Samuelsen, P.J. Houen et al., “3D Imaging of Paper by use of Synchrotron X-ray Microtomography” (Paper presented at TAPPI International Paper Physics Conference, San Diego, California, 26-30 Sept 1999), 307.
6. A. Goel, M. Tzanakakis, et al., “Characterization of the Three-Dimensional Structure of Paper using X-Ray Microtomography,” Tappi J. 84 (5) (2001), 72-80.
7. M. Aronsson, “On 3D fibre measurements of digitized paper” (PhD thesis, Swedish University of Agricultural Sciences, 2002).
8. J. Lunden, “Image analysis methods for evaluation of fibre dimensions in paper cross-sections” (Master's thesis, The Swedish Royal Institute of Technology, 2002).
9. R. Holen, and M. Hagen, “Segmentation on absorption mode x-ray micro tomographic images of paper” (Master's thesis, Norwegian University of Science and Technology, 2004).
10. J. Bache-Wiig, and P.C. Henden, “Individual fiber segmentation of three dimensional microtomograms of paper and fiber-reinforced composite materials,” (Master’s thesis, Norwegian University of Science and Technology, 2005).
11. M. Axelsson, “3D Tracking of Cellulose Fibres in Volume Images” (Paper presented at IEEE International Conference on Image Processing, San Antonio, Texas, Oct. 2007), 309–312.
12. C. Xu, and J.L. Prince, “Gradient Vector Flow: A new external force for snakes” (Paper presented at IEEE Computer Society Conference on Computer Vision and Pattern Recognition, Los Alamitos, California, Jun. 1997), 66-71.
13. R. Adams, and L. Bischof, “Seeded region growing,” IEEE Trans. Pattern Anal. Mach. Intell., 16 (6) (1994), 641–647.
14. J. Weickert, B. Haar, and R. Viergever, “Efficient and reliable schemes for nonlinear diffusion filtering,” IEEE Trans. Image Proc., 7 (3) (1998), 398-410.
15. C. R. Maurer, R. Qi, and V. Raghavan, “A Linear Time Algorithm for Computing Exact Euclidean Distance Transforms of Binary Images in Arbitrary Dimensions," IEEE Trans. Pattern Anal. Mach. Intell., 25 (2) (2003), 265-270.

2nd International Congress on 3D Materials Science
Edited by: Dominique Bernard, Jean-Yves Buffière, Tresa Pollock, Henning Friis Poulsen, Anthony Rollett, and Michael Uchic
TMS (The Minerals, Metals & Materials Society), 2014

3D IMAGE SEGMENTATION AND CYLINDER RECOGNITION FOR COMPOSITE MATERIALS

Amaury Walbron[1,2], Sylvain Chupin[1], Denis Rochais[1], Romain Abraham[2], Maïtine Bergounioux[2]

[1]CEA Le Ripault, BP 16, 37260 Monts, France
[2]MAPMO, Université d'Orléans, BP 6759, Route de Chartres, 45067 Orléans cedex 2, France

Keywords: Image Processing, Segmentation, Markov Random Field, Straight Line Detection.

Abstract

The modelling of three-dimensional composite carbon fibers-resin materials for a multi-scale use requires the knowledge of the carbon fibers localization and orientation. We propose here a mathematical method exploiting tomographic data to determine carbon localization with a Markov Random Field (MRF) segmentation, identify carbon straight cylinders, and accurately determine fibers orientation.

Introduction

X-ray computed tomography is a powerful non-destructive technique allowing to see inside an object without destroying it. This method uses a series of two-dimensional radiographic images rotated around an axis of rotation to get a three-dimensional image of the object with reconstruction algorithms. In particular, this technique can be used to obtain three-dimensional views of composite materials to study their structure and properties.

Problem and Purpose

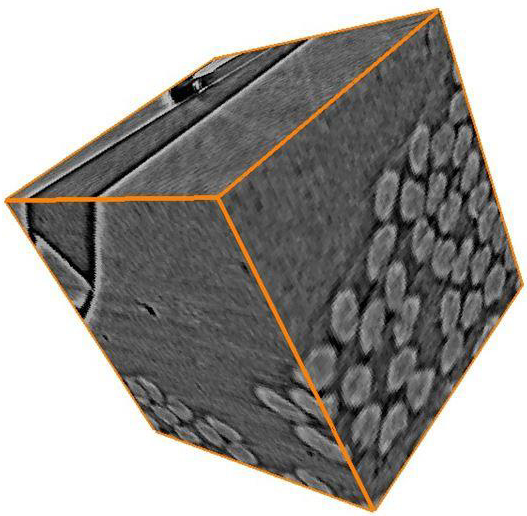

Figure 1. 3D rendering (ESRF synchrotron, voxel size: 0.7µm) of a fibers-resin composite X-tomography. Light-gray areas are carbon fibers (and a pore), and dark areas are resin.

In order to model macroscopic structures of composite materials with small characteristic dimensions, it is necessary to replace them by homogeneous materials with similar properties.

This allows to describe structures by fewer variables and leads to fast computation codes. We consider the case of a carbon fiber-resin composite (Figure 1.) and look for a well-scaled thermal equivalent homogeneous material. For that purpose, two different datasets are required namely properties of each component (experimentally measured) and their repartition (localization and orientation) in composite material. To get relevant structures of composite material, we use 3D X-tomographic images. However, the segmentation process for each component is not straightforward (as shown on Figure 3.).

Chosen Approach

We present here processing methods to obtain segmented images that we use next to search the orientation of carbon fibers. We use a homemade Markov Random Field (MRF) software [1,3] to perform segmentation with a global fitting data term and a local interaction term as well. We first use the Potts model [4] with and without parameter optimization. These methods have the advantage to be easily computable and parallelizable, with linear complexity, and provide good results.
The considered material is a carbon fiber/phenolic resin composite, whose fibers can be approximated by cylinders. Fibers are spatially connected in *yarns*, composed of fibers with the same orientation and separated by a resin zone. Yarns form a non-dense weaving into resin matrix.
We propose a method for lines recognition which consist in considering a closed surface section and gathering cylindrical sections comparing pixels between them with a component-connected labelling algorithm [2]. Finally, a method for reconstitute yarns is proposed with a K-means clustering algorithm [8] and a Delaunay triangulation [9,10].

Image Segmentation using Markov Random Fields

Markov Random Fields Model

Images spatial properties may be considered from global and local points of view. MRFs give a convenient way to model local informations such as pixels grey level and/or correlation between them. For that, MRF distributions are used to quantify contextual informations in images.

Let $\mathcal{L} = \{0,1\}$ be the considered label set for our problem, and $\mathcal{D}$ the set of voxels values for our image. Let $\boldsymbol{X} = (X_i)_{i\in S}$ be a family of random variables indexed by S, every variable X_i taking its value x_i in $\mathcal{D}$. Such a family $\boldsymbol{x} = (x_i)_{i\in S}$ is called a random field and is a configuration of $\boldsymbol{X}$. We similarly define $\boldsymbol{Y} = (Y_i)_{i\in S}$ with values in $\mathcal{L}$. Moreover, we consider a neighborhood system $\mathcal{N}: i \in S \to \mathcal{N}(i) \in \mathcal{P}(S)$ the power set of S, and we define a **clique** as a subset of sites for which every pair are neighbors. We assume that $\boldsymbol{Y}$ is a MRF if it satisfies:

- Positivity: $\forall \boldsymbol{y}, \mathbb{P}(\boldsymbol{Y} = \boldsymbol{y}) > 0$.
- Markovian condition: $\mathbb{P}\left(Y_s = y \middle| \boldsymbol{Y}_{S\setminus s} = \boldsymbol{y}_{S\setminus s}\right) = \mathbb{P}\left(Y_s = y \middle| \boldsymbol{Y}_{\mathcal{N}(s)} = \boldsymbol{y}_{\mathcal{N}(s)}\right)$ [3,5].

The Markov field associated probability density function is a Gibbs distribution according to Hammersley-Clifford theorem [1]. Thus

$$\mathbb{P}(\boldsymbol{Y} = \boldsymbol{y} | \boldsymbol{X} = \boldsymbol{x}) = \frac{e^{-U(\boldsymbol{y}|\boldsymbol{x})}}{Z(\boldsymbol{x})}$$

where $Z(\boldsymbol{x})$ is a normalizing constant called partition function, and $U(\boldsymbol{y}|\boldsymbol{x})$ is an energy of the form

$$U(\boldsymbol{y}|\boldsymbol{x}) = \sum_{c \in C} V_c(\boldsymbol{y}|\boldsymbol{x})$$

which is a sum of clique potentials over all possible cliques.

Potts Model

The Potts Model uses an energy function U with single-site and double-site cliques only. Single-site cliques contribution consists in data connection, which depends on a conditional probability density function associated to every label. These functions deal with the probability for a site with label $l \in \mathcal{L}$ to have a given voxel value $x \in \mathcal{D}$. Double-site cliques contribution expresses spatial correlation between labels, increasing energy if neighbors have different labels and decreasing it otherwise. The energy function with Potts model writes

$$U(\boldsymbol{y}|\boldsymbol{x}) = -\sum_{s \in S} \left(\ln\left(p(x_s|y_s)\right) + \beta \sum_{t \in \mathcal{N}(s)} (\delta(y_s, y_t) - 1) \right)$$

where δ the Kronecker function and β a weight parameter adjusting local contribution. It can be optimized with a pseudo-likelihood maximum method [6,7].
The goal of MRF method is to find the configuration $\boldsymbol{y}$ minimizing the energy for a known configuration $\boldsymbol{x}$.

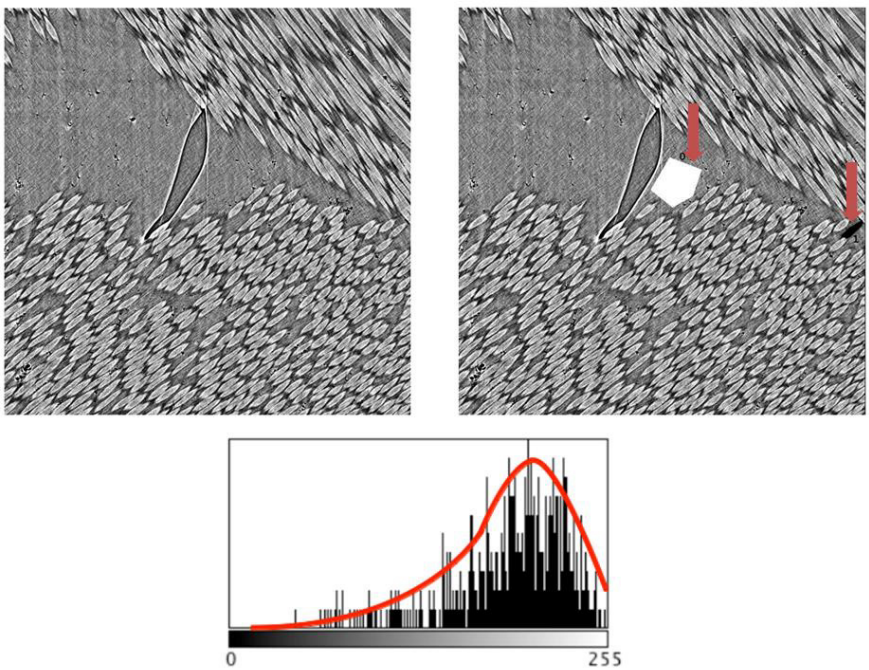

Figure 2. Base image (top left-side), image with initialization areas in black and white (top right-side, highlighted by arrows), black area histogram and approximate probability density in red (bottom).

We note that this method is supervised. Indeed, we have to know probability density functions $p(\cdot\,|l), l \in \mathcal{L}$ to reckon energy. For that, we search small "representative zones" for each label l in our image. In other words a zone whose sites have the same label l and voxel values histogram is close to expected histogram for the entire region of label l. Then the histogram is modelled with a density probability function (Figure 2.).

Straight Lines Detection and Orientation Search

Straight Lines Detection Method

Assume now that we have a binary image $\boldsymbol{y}$, resulting from the MRF method segmentation for a carbon fiber-resin image. To get fibers, we used their properties: fibers are straight cylinders whose cross section is a circle with same radius ρ. In addition, a straight line intersects two time cube boundaries if it is not included in them.
Moreover intersection centers between image boundaries and our cylinders are points on the cylinder generating line. Thus the proposed method is:

- Calculating $(E_i)_i$ the ensemble of intersections between extern boundaries and cylinders.
- Deducting the ensemble $(c_i)_i$ of associated centers.

For every pair c_i, c_j, a ρ-radius cylinder connects them if and only if every voxel inside the cylinder has the same label.

For defining $(E_i)_i$, we will use a component-connected labelling algorithm. Indeed, if a cylinder links c_i and c_j, then they belong to a connected region whose have the same value.
We give a tolerance δ to the cylinders research, i.e. for every pair c_i, c_j, a ρ-radius cylinder connects them if and only if more than $100 * (1 - \delta)$ % of the sites r verify the condition.
A fast method for calculating connected region on an image has been used in this algorithm [2].

Global orientations Search

Assume that we have now a set of cylinders characterized by a unique radius $\rho > 0$ and a triplet $(s, \theta, \varphi) \in S \times [0; \pi] \times [0; \pi]$ which describes the generating line in a given basis. We aim to cluster theses cylinders in different regions according to their angles (θ, φ) first, and to their spatial localization after. In this way we gather the cylinders of the same yarn, and then we obtain the localization of the yarn. For this, we assume that we know the yarns number n in the image.
We use a K-means clustering algorithm to gather cylinders according to angles (θ, φ) [8], and then a Delaunay triangulation [9,10] for spatial clustering.
Finally, to get yarns, we choose the orthogonal plane to the yarn mean direction and calculate its intersections with the yarn fibers. We compute this convex hull set assuming that associated straight lines constitute the convex hull of yarn. Then, if we suppose yarns are convex, we get the yarn itself [11].

Results

Markov Random Fields Segmentation

Figure 3. shows the difference between the MRF segmentation algorithm and a median-threshold filtering. The algorithm has a complexity of $O(w * h * l) = O(s)$ where w, l, h, s are respectively

the width, height, length and total size of the image. This algorithm is easily parallelizable thanks to the energy form, which depends only of neighbors. The maximal speedup obtained is around $s = 10$ (for a 400^3 image, the calculation time is t~600s for 1 processor, and t~60s for up to 10 processors)

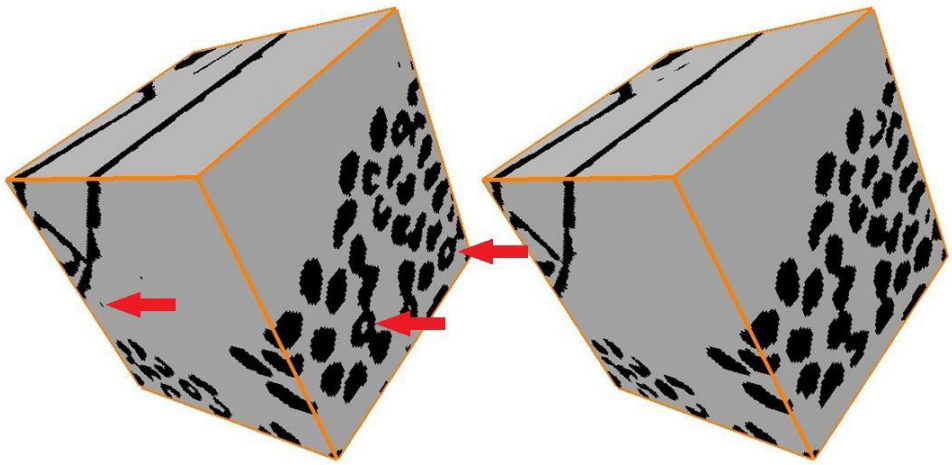

Figure 3. Difference between MRF segmentation (right-side) and "classic" median + threshold filtering (left-side). Arrows highlight defects for "classical" filtering.

Straight Lines Detection Algorithm

Figure 4. shows the result of the straight lines detection algorithm for the same 400^3 image. This algorithm has a complexity of $O(s)$ for a constant cylinders number, but $O(s^{5/3})$ for a constant cylinders density. Table I. summarizes the calculation time explosion with size (103 332s is around 28h). Table II. shows reliability of the method. This algorithm is parallelizable too, but calculation time is still very high for big data. Therefore we use methods to cut images, use algorithms on each part, and then gather the results with interpolation and matching method.

Table I. Time results of straight line recognition algorithm for different images size (for 10 processors).

Size	**100³**	**400³**	**1000³**
Calculation time (s)	1.4	637	103 332
Number of iterations	41	1464	7624

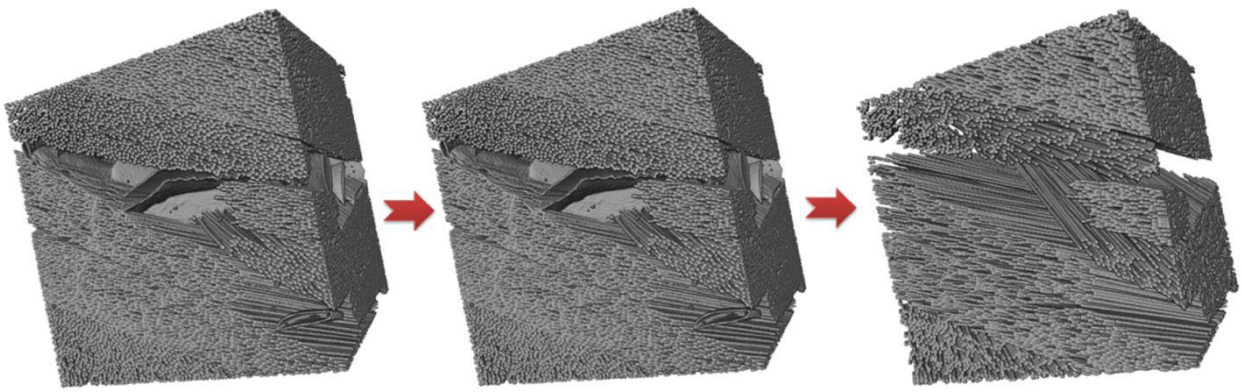

Figure 4. Base image (left-side), segmented image (center) and lines recognition algorithm result (right-side).

Table II. Method reliability for different tolerances (for a 400^3 image).

Tolerance	**0**	**0.25**	**0.3**
Percentage of detected straight lines	50 %	80 %	90 %
Number of aberrant lines	0	2	$\leq$ 10 (for 1600 lines)

Conclusions

We propose a fast method for lines recognition in some particular cases. The algorithm can provide a high number of cylinders, even if most of them are close one to another. We succeeded in identifying spatially close cylinders with similar orientation so that we may represent fibers packs by only one homogeneous area. Finally, we can recover the structure at a scale allowing thermal transfer simulation.

References

1. S. Geman and D. Geman, "Stochastic relaxation, Gibbs distributions and the Bayesian restoration", *IEEE Trans. Pattern Anal. Mach. Intell.*, PAMI-6 (6) (1984), 721-741.

2. L. He et al., "Fast connected-component labeling", *Pattern Recognit.*, 42 (2009), 1977-1987.

3. S. Li, *Markov Random Field Modeling in Image Analysis* (London, UK: Springer-Verlag, 2009).

4. R. Potts, "Some generalized order-disorder transformation", *Proc. of the Cambridge Philosophical Society*, 48 (106) (1952)

5.G. Celeux, F. Forbes, and N. Peyrand, "EM procedures using mean field-like approximations for Markov model-based image segmentation", *Pattern Recognit*., 36 (1) (2003), 131-144.

6. J. E. Besag, "Spatial interaction and the statistical analysis of lattice systems", *J. Roy. Stat. Soc. Ser. B*, 36 (2) (1974), 192-236.

7. L. Wang, J. Liu, and S. Z. Li, "MRF parameter estimation by MCMC method", *Pattern Recognit*., 33 (11) (1999), 1919-1925

8. J. B. MacQueen, "Some methods for classification and analysis of multivariate observations", *Proceedings of the Fifth Symposium on Math, Statistics, and Probability* (Berkeley, CA: University of California Press, 1967), 281-297

9. B. Delaunay, "Sur la sphere vide", *Izvestia Akad. Nauk SSSR, Otdelenie Math. i Estestvennykh Nauk* (1934)

10. D. T. Lee and B. J. Schachter, "Two Algorithms for contrasting a Delaunay triangulation", *International Journal of Computer and Information Science*, 9 (1980), 219-242

11. R. A. Jarvis, "On the identification of the convex hull of a finite set of points in the plane", *Information Processing Letters*, 2 (1) (1973), 18-21.

2nd International Congress on 3D Materials Science
Edited by: Dominique Bernard, Jean-Yves Buffière, Tresa Pollock, Henning Friis Poulsen, Anthony Rollett, and Michael Uchic
TMS (The Minerals, Metals & Materials Society), 2014

MICROSTRUCTURAL DATA FOR MODEL DEVELOPMENT AND VALIDATION

Veronica Livescu[1], Curt A. Bronkhorst[1], John F. Bingert[2]

[1]Los Alamos National Laboratory, Los Alamos, NM 87545, USA
[2]OUSD(AT&L)/TWS/LW&M, Washington, D.C. 20301, USA

Keywords: microstructure, shock loading, void damage, EBSD, damage models, tantalum

Abstract

The dynamic deformation of metallic polycrystalline materials leading to ductile damage and failure events involves a complex series of physical processes which are poorly understood. This lack of understanding prevents us from properly formulating and offering the appropriate physically based theories for accurate and robust representation of the ductile damage and failure response of ductile materials. This paper briefly describes and illustrates a coupled experimental and computational methodology to develop greater physical insight linking the structural details of the material to its formation of damage sites. Results from examinations of both tantalum and copper are presented to illustrate the types of methodologies that will be needed in the future to better understand the critical physical processes occurring in polycrystalline metallic materials leading to their catastrophic failure.

Introduction

The characterization and modeling of damage and failure of metallic materials under extreme loading conditions are important scientific and technological problems in a variety of practical applications such as high velocity impact, explosive working, and defense. Extensive previous work indicates that microstructure plays an important role in the damage and failure process, and this complex physical process is substantially affected by material anisotropy and the presence of both intrinsic and extrinsic defects and heterogeneities [1-5]. We are mainly considering high purity materials, therefore second-phase particles, impurities and initial porosity are virtually non-existent. However, the influence of crystallographic features such as grain size, preferred orientation, the formation, interaction, and ultimately the effect of deformation features on the material behavior occurs over many different length scales. This remains as a substantial computational challenge to predictively represent the ductile damage and failure process.

To add to the complexity of this problem, microstructure is an inherently three-dimensional (3D) construct and its complete description requires 3D characterization and analysis. This is especially important to advance the understanding of phenomena historically described in probabilistic terms, i.e. void damage. In particular, nucleation of damage is a statistical process where the distribution of sizes and strengths of defects in 3D, along with the basic physical mechanisms of damage nucleation, play a fundamental role. Within the context of our present macro-scale representation of ductile damage, based on experimental observations, void nucleation is where microstructural imprint can be best represented. Microstructure characterization of shocked tantalum samples indicates that voids nucleate at specific microstructural features. For example, in a soft recovered plate impact tantalum sample shocked

at 5.6 GPa with a square wave, voids nucleate at grain boundaries. The 3D reconstruction from serial sectioning of the kernel average misorientation maps (KAM) around the void network (Figure 1) reveals contiguous and complex plastic linkages in 3D. This process is extremely complex, stochastic and inherently dependent on loading path and rate. While crystal plasticity-based simulations have been successful in predicting the average crystallographic texture and development due to deformation, they generally fail to predict the nature and extent of the local intergranular misorientations due to deformation [6]. In general, it is unlikely that we will successfully predict damage and failure events in materials without mesoscale aware modeling tools.

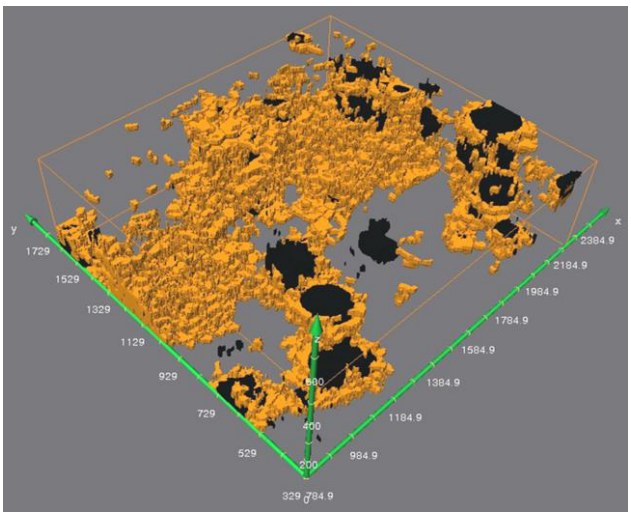

Figure 1. 3D reconstruction of KAM maps in tantalum shocked at 5.6GPa and 1.1μs pulse. Black and orange represent void damage and deformation affected material respectively.

The work presented here supports the developing of successful predictive damage capabilities by capturing real distributions of microstructural features from the starting material using emergent stereological methods and implementing them as digitally-generated microstructures in the damage model development. The interaction of these statistical distributions will determine where failure will occur in the 3D microstructure. On-going research is also concentrated on providing insight on the progression of deformation, validating critical deformation and damage mechanisms, and identifying those microstructural features that might initiate damage first.

Material

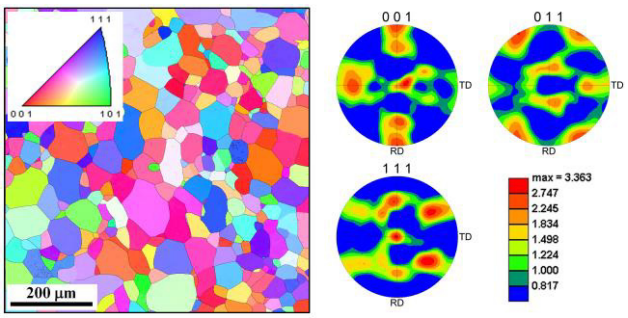

Figure 2. Grain structure and texture for the rolled and annealed tantalum material.

The material used for this study is rolled and annealed high-purity tantalum plate obtained from Cabot Corporation. The plate composition was high purity, with O, N, C, and H contents <50, 10, 10, and 5 ppm, respectively. Other impurities were below the resolution limits of 5 ppm, or 25 ppm in the case of W and Nb. The material's average grain size is approximately 33 μm as measured from crystallographic orientation data acquired by Electron Backscatter Diffraction (EBSD). The microstructure and texture of the tantalum are shown in Figure 2. Grains are equiaxed and the material exhibits a weak texture. A Philips XL30 SEM was used to acquire many 1 μm step-size orientation maps encompassing approximately 30,000 grains, which captured more than 70,000 boundary segments. Grain size, orientation distribution function (ODF) and grain boundary misorientation parameters were determined using the TSL Orientation Imaging Microscopy (OIM) software.

Statistically Equivalent Microstructures

The approach for the proposed work is to use the dream.3d software package (http://dream3d.bluequartz.net/) to incorporate relevant statistics in digitally generated microstructures for use in polycrystal calculations. Dream.3d is a novel open and modular software package that allows for the reconstruction, instantiation, quantification, meshing, and visualization of microstructures digitally. The tantalum microstructure studied here is equiaxed and the grain size distribution is similar in all three plate directions. The parameters of the matching normal distribution for the grain size, the mean μ and the standard deviation σ of the variables' natural logarithm, were 3.5 and 0.55 respectively. The ODF was extracted from the EBSD data and uploaded into the statistical generator. The statistics file exported from dream.3d was used to generate digital volumes of various sizes. A series of runs was performed, generating between 20 and 3000 grains each. For each run, the grain size data was fitted with a lognormal distribution and compared to the starting grain size distribution. Figure 3 presents a digitally generated tantalum microstructure containing about 1500 grains. Quantile-quantile (QQ) plots were used as an exploratory graphical device to check the validity of the grain size distributional assumption for each data set. Values for the resulting μ and σ were within 1-2% compared to μ and σ of the input distribution.

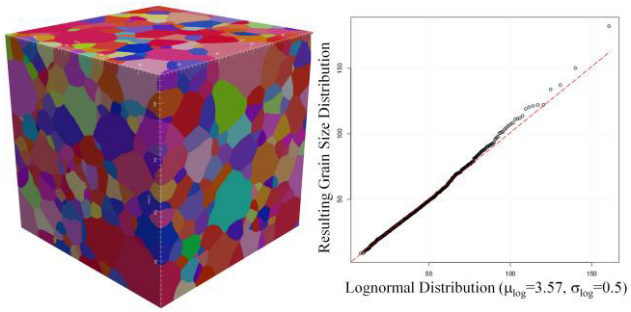

Figure 3. Digitally-generated tantalum microstructure: volumetric representation (left) and QQ plot for grain size distribution (right).

Connections to Damage Nucleation under Shock Loading

Grain boundaries play an important role in damage development. Grain boundary energies are anisotropic and relative energies determine the properties of a material. In addition, boundaries can be relatively more or less plastically accommodative based on their structure. Given the importance of the boundary plane in influencing properties, it is important to measure orientation distributions of boundary planes in polycrystals, not merely boundary misorientations. Aspects of the five-parameter distribution in tantalum were examined in detail via observation of the plane distributions for specific misorientations using the method described in [7]. The distribution of the grain boundary planes can be plotted on a stereographic projection at specific misorientations. Results for tantalum are shown in Figure 4. The plane distributions on the [110] misorientation axis indicate that, for the majority of the misorientations, the density distribution is clustered around the [110] zone, meaning that boundaries with a twist character are preferred. An exception is the case of low misorientations where [111] symmetric tilt boundaries also occur several times more than random. The peaks are broad, indicating that many boundaries have a mixed character. For misorientations around [111], boundaries with twist character are preferred at lower misorientations, while mixed boundaries are adopted for higher misorientations. For misorientations around [100], grain boundary plane orientations in the [111] zone are preferred for low angle boundaries, and mixed boundaries are adopted for higher angle misorientation. The

grain boundary plane distribution is important by providing real material information that we can introduce into the damage models. In addition, knowing the type of boundaries that exist in a material helps in interpreting materials' response to deformation. Boundary character distributions, such as the ones presented in Figure 4, are extracted from EBSD data in dream.3d and incorporated into the statistics file for synthetic microstructure generation. Work on connecting these highly occurring boundaries to damage nucleation will be presented elsewhere.

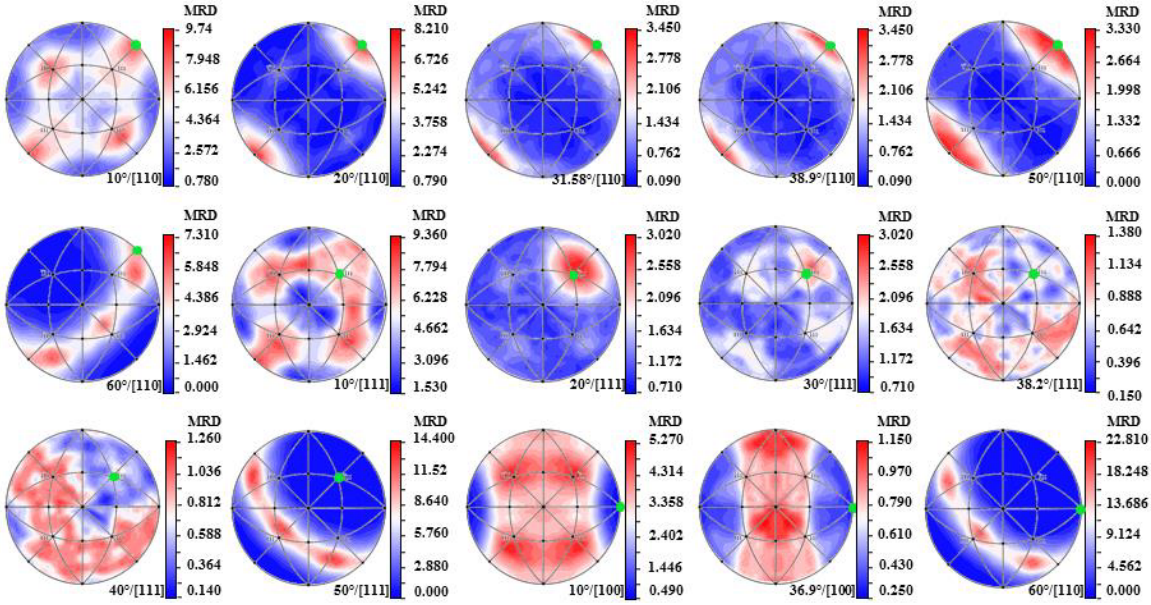

Figure 4. Grain boundary plane distribution for misorientations around the [110], [111], and [100] axes. The misorientation axis is indicated by a green dot.

Towards the Development of Dynamic Damage Models

As previously discussed, the challenges to understand and represent the complex physical processes involved with the ductile damage and failure process in polycrystalline metallic materials are many. Although we know in general that structural details of the material are a significant factor in determining how a material deforms, there is only limited physical experimental information available concerning the relevant physical processes for dynamic and shock loading conditions. There is a strong need to supplement the information which is available experimentally with computational studies on dynamic material response. In this section we outline a brief example of how structural information as presented above can be used in computational studies to lend greater insight into the dynamic ductile damage behavior of metallic materials. In general, simple plate impact experiments are conducted to study and quantify the shock loading response of metallic materials. The free surface velocity of the shock loaded sample measured during the experiment is the most readily available quantity for such an experiment, with the occasional recovered sample. The latter is less common since for all but mild loading conditions, there is little left of the sample to recover unless means of soft capture are utilized. The interpretation of physical behavior is then done by comparing experimental versus calculated free surface velocity responses by including hypothesized mechanisms within

the theoretical model used to conduct the simulations. We have done this for a high purity copper sample which was loading by a z-cut quartz flyer with an impact velocity of 110 m/s.

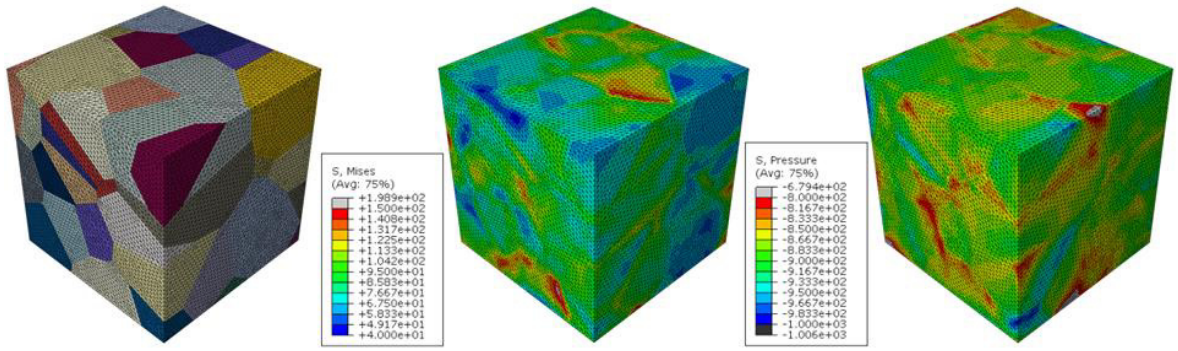

Figure 5. 64 grain Voronoi tessellated structure used to probe the micromechanical response to dynamic loading: Structural topology (left), von Mises stress (center), and pressure (right).

Through the use of a rate-dependent macro-scale damage model [8] we have calculated the time in the experiment at which the model suggested that the progression of pore growth begins. At that point in time we have extracted the calculated stress profile within the sample. This profile is non-uniform as can be expected with a peak stress near the center of the sample: 1.01 GPa in the axial loading direction, and 895 MPa in the radial and circumferential directions. We have applied this stress condition to the three principal faces of a 64 grain polycrystal cube shown in Figure 5 to probe the heterogeneous stress state which might drive the initiation of damage.

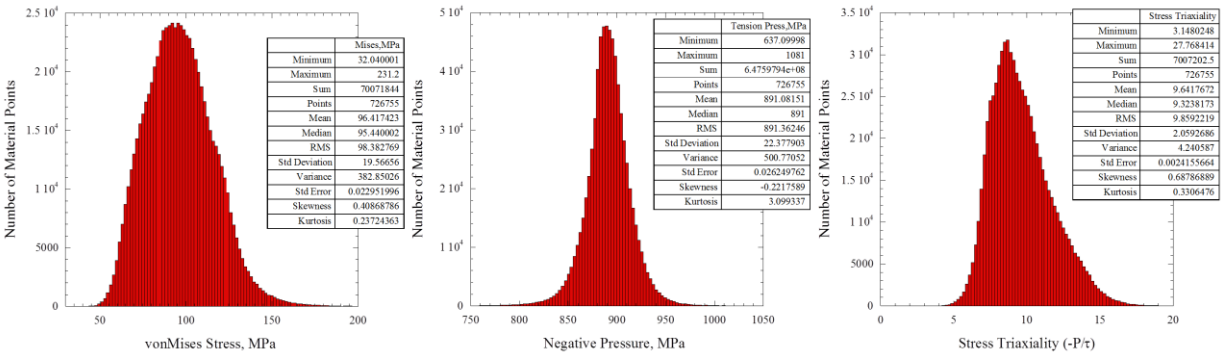

Figure 6. Stress distributions for the calculations shown in Figure 5. Left is the von Mises stress, center is negative pressure, and right is stress triaxiality.

The single crystal model used in these calculations is based upon thermally activated motion of dislocations [9]. The statistical distribution of von Mises stress, pressure, and stress triaxiality are shown in Figure 6 for the results shown in Figure 5. The results shown in Figures 5 and 6 are approximations to what one might expect the local stress state to be in polycrystalline metallic samples under realistic loading conditions leading to the initiation of void development. In the future we will use the coupling between experimental and computational results to develop a richer picture of the physical state of the material and also evolutionary processes involved in the ductile damage process. Clearly, statistically accurate 3D topologies of material structure will be critical to the accurate portrayal of material response in this computational methodology.

The statistics file generated in dream.3d is utilized to generate large polycrystalline volumes matching grain size and shape, grain orientations and grain boundary distributions. Reduced

volumes, such as the one shown in Figure 7a are cropped form larger 3D models and used for method development. The synthetic volumes are surface-meshed to allow the models to be moved into FEM or other simulations. In this case, we successfully imported the tantalum dream.3D geometry files into the ABAQUS pre-processor as shown in Figure 7b. The strategy is to mesh each grain independently, reconstruct the volume, and either fully tie the boundaries together or allow for grain boundary deformation or separation under loading conditions. This will in general enable detailed linkages between material structure and the available dynamic experimental data. Final computations will be performed on large statistically representative synthetic polycrystals and will use a model in which the defect density and dislocation motion are involved in the void nucleation process, and captures effects of interfaces, neighbor interactions and local fields.

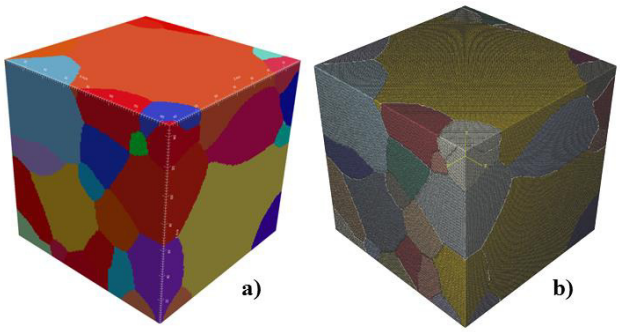

Figure 7. Tantalum virtual microstructures: (a) Virtual tantalum polycrystals generated in DREAM.3D, and (b) Tantalum grains reconstructed in the ABAQUS preprocessor.

Acknowledgement: This work was supported by the Joint DoD/DOE Munitions Technology Development Program and the DOE NNSA Science Campaign 2.

References

1. R. Vignjevic et al., “Effects of orientation on the strength of the aluminum alloy 7010-T6 during shock loading: Experiment and simulation”, *Journal of Applied Physics,* 92 (8) (2002), 4342-4348.
2. R.W. Minich et al., “Effect of microstructural length scales on spall behavior of copper”, *Metallurgical and Materials Transactions A: Physical Metallurgy and Materials Science,* 35a (9) (2004), 2663-2673.
3. X. Chen et al., “Spall behavior of aluminum with varying microstructures”, *Journal of Applied Physics,* 99 (2) (2006), no. 023528.
4. J. P. Escobedo et al., “Effects of Grain Size and Boundary Structure On the Dynamic Tensile Response of Copper”, *Journal of Applied Physics*, 110 (2011), no. 033513.
5. V. Livescu, J.F. Bingert, T.A. Mason, “Deformation twinning in explosively-driven tantalum”, *Materials Science and Engineering A- Structural Materials Properties Microstructure and Processing,* 556 (2012), 155-163.
6. B. M. Schroeter, D. L. McDowell, “Measurement of deformation fields in polycrystalline OFHC copper”, *International Journal of Plasticity*, 19 (2003), 1355-1376.
7. D.M. Saylor, A. Morawiec, and G.S. Rohrer, "Distribution of Grain boundaries in Magnesia as a Function of Five Macroscopic Parameters," *Acta Materialia*, 51 (2003) 3663-74.
8. C. A. Bronkhorst et al., “An experimental and numerical study of the localization behavior of tantalum and stainless steel”, *International Journal of Plasticity*, 22 (2006), 1304-1335.
9. C. A. Bronkhorst et al., “Modeling the microstructural evolution of metallic polycrystalline materials under localization conditions”, *Journal of the Mechanics and Physics of Solids*, 55 (2007), 2351-2383.

2nd International Congress on 3D Materials Science
Edited by: Dominique Bernard, Jean-Yves Buffière, Tresa Pollock, Henning Friis Poulsen, Anthony Rollett, and Michael Uchic
TMS (The Minerals, Metals & Materials Society), 2014

LARGE SCALE 3D MULTI-PHASE-FIELD SIMULATION OF MICROSTRUCTURE EVOLUTION USING TSUBAME2.5 GPU-SUPERCOMPUTER

Akinori Yamanaka[1], Masashi Okamoto[1], Takashi Shimokawabe[2] and Takayuki Aoki[2]

[1]Division of Advanced Mechanical Systems Engineering, Tokyo University of Agriculture and Technology, 2-24-16, Naka-cho, Kogane-shi, Tokyo 184-8588, Japan
[2]Global Scientific Information and Computing Center, Tokyo Institute of Technology, 2-12-1, O-okayama, Meguro-ku, Tokyo 152-8588, Japan

Keywords: Multi-Phase-Field Method, GPU Computing, Microstructure Evolution

Abstract

The multi-phase-field (MPF) method has attracted attention as a very promising tool for simulating microstructure evolutions in polycrystalline materials. However, because of the heavy computational cost incurred by three-dimensional (3D) MPF simulations, simulating realistic microstructure morphology in three dimensions has been difficult. In our research, we developed a multiple-GPU computing technique and an overlapping method that facilitate efficient 3D MPF simulations. Using the technique developed, we performed 3D MPF simulations of polycrystalline grain growth on a GPU-cluster and on the TSUBAME2.5 supercomputer at the Tokyo Institute of Technology. The results obtained indicate that our multiple-GPUs computing technique combined with the overlapping method significantly reduce the elapsed time of simulations and easily facilitate the performance of very large-scale 3D simulations with up to 1024^3 computational grids.

Introduction

The mechanical properties of metallic materials are strongly influenced by the distribution and morphology of their underlying microstructures. Therefore, it is essential that numerical tools that can predict microstructure evolutions in materials via numerical simulations be developed. Recently, the multi-phase-field (MPF) method has attracted much attention as a very promising technique for simulating microstructure evolutions in polycrystalline materials [1–3]. The MPF model has been widely employed in numerical simulations of microstructure evolutions during solidification, grain growth, recrystallization and phase transformation [4, 5]. However, as is well known, very small computational grids have to be used in order to obtain quantitative results from such MPF simulations because the simulation result depends on the size of the computational grid [6]. Consequently, performance of quantitative MPF simulations in realistic three-dimensional (3D) space incurs very heavy computational costs. In previous studies, parallel computing of 3D MPF simulations using various computing techniques, such as OpenMP and message passing interface (MPI), have been performed [7]. However, in order to evaluate more realistic microstructure evolutions using MPF, it is essential that the size of the computational domain be increased. We have accelerated MPF simulation using a graphics processing unit (GPU) that was originally developed for high-speed computer graphics processing [8]. However, although we previously demonstrated that GPU computing enables us to accelerate MPF simulation more than ten times faster than conventional CPU computing, unfortunately, the amount of memory on a conventional GPU is not enough to perform realistic large-scale 3D

simulations.

Thus, in our research, we consequently developed an efficient and high-speed computing technique that uses multiple-GPUs to perform efficient large-scale 3D MPF simulations. Using the developed computing technique, we evaluated the acceleration performance of 3D MPF simulation of polycrystalline grain growth on a GPU-cluster computer. Comparing the results obtained for multiple-GPUs and multiple-CPUs computing, we discovered that the multiple-GPUs computing technique is much more effective for acceleration of 3D MPF simulations than conventional parallel CPU computing. Further, we implemented the multiple-GPUs computing technique on the TSUBAME2.5 GPU-supercomputer at the Tokyo Institute of Technology, where we were able to perform very large-scale 3D MPF simulations.

Multi-Phase-Field Model

In order to simulate the polycrystalline grain growth driven by minimization of interfacial energy, the generalized MPF model proposed by Steinbach et al. [2] is predominantly employed. When we consider a system of N crystal grains, N phase-field variables, ϕ_i (i=1, 2, …, N), are defined. Here, ϕ_i describes the local volume fraction of the ith grain and varies smoothly across an interface from $\phi_i = 1$ in the ith grain to $\phi_i = 0$ in another grain. Using the phase-field variables, the total Gibbs free energy of the system, G, is defined as follows:

$$G = \int_V \left[\sum_{i=1}^{N} \sum_{j=i+1}^{N} \left(W_{ij} \phi_i \phi_j \right) + \sum_{i=1}^{N} \sum_{j=i+1}^{N} \left(-\frac{a_{ij}}{2} \nabla \phi_i \cdot \nabla \phi_j \right) \right] dV \tag{1}$$

where a_{ij} and W_{ij} are the gradient coefficient and the height of the energy barrier, respectively. These parameters are related to the interfacial energy between the ith grain and the jth grain, σ, and interfacial thickness, δ.

Assuming that the total free energy decreases monotonically with time, the evolution equation of the phase-field variables can be derived as

$$\frac{\partial \phi_i}{\partial t} = -\frac{2}{n} \sum_{j=1}^{n} M_{ij}^{\phi} \left(\frac{\partial G}{\partial \phi_i} - \frac{\partial G}{\partial \phi_j} \right) \tag{2}$$

where n is the number of phase-field variables at an arbitral point and M_{ij}^{ϕ} is the mobility of the phase-field variables related to physical interfacial mobility, M. Substituting Eqn. (1) into Eqn. (2), we obtain the final form of the evolution equation of the phase-field variables as follows:

$$\frac{\partial \phi_i}{\partial t} = -\frac{2}{n} \sum_{j=1}^{n} M_{ij}^{\phi} \sum_{k=1}^{n} \left\{ \left(W_{ik} - W_{jk} \right) \phi_k + \frac{1}{2} \left(a_{ik}^2 - a_{jk}^2 \right) \nabla^2 \phi_k \right\} \tag{3}$$

We performed the calculation defined by Eqn. (3) in a numerical simulation using a second-order finite difference scheme for space with a first-order forward Euler-type finite difference method for time on a regular 3D computational grid. Further, we employed the active parameter tracking (APT) method proposed by Kim et al. [9] to reduce the computational load and memory

consumption.

Multiple-GPUs Computing Technique

In our study, we used the NVIDIA Tesla K20X GPU. This GPU contains 2688 CUDA cores constituted from 14 streaming multiprocessors (SMX), each of which comprises 192 CUDA cores as single instruction, multiple data stream units. In CUDA, onboard device memory is called global memory, and the amount of global memory on the GPU is 6.0 GB (GDDR5 SDRAM). In order to perform computations on the GPU, we developed program code using the CUDA Fortran language released by the Portland Group, Inc. [10].

To conduct parallel computing of the MPF simulation using multiple-GPUs and CPUs on the GPU-cluster computer and on the TSUBAME2.5 supercomputer, we decomposed an entire computational domain into subdomains. Then, we assigned the computation in each subdomain to one compute node. The entire computational domain can be partitioned in 1D, 2D, or 3D. When the whole computation domain is decomposed in 3D, as shown in Figure 1, the computation in each subdomain requires data on the surface of the neighboring subdomains (boundary region). Therefore, similar to conventional multi-CPU computing with MPI, we have to conduct data communication among the nodes to exchange data between neighboring subdomains. However, because data communication decreases parallel efficiency, we developed an overlapping method that masks the time taken for data communication by conducting both the computation on the GPU and the data communication simultaneously [11].

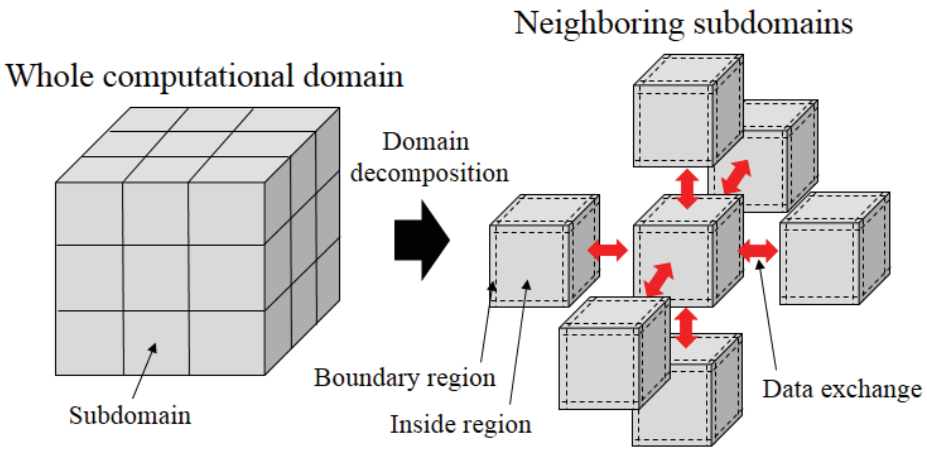

Figure 1. 3D domain decomposition of computational domain.

Figure 2 depicts the computational diagram used to calculate the MPF simulation with the overlapping method. Our computational method primarily comprises four steps: (1) Computation of the MPF simulation on the GPU, (2) data communication between CPU and GPU via CUDA APIs [12], (3) computation of the APT method on the CPU, and (4) data communication between the nodes with MPI. First, the GPU starts to compute the inside region and the boundary region, concurrently. After the computation for the boundary region is finished, the calculated data on the global memory is transferred to the CPU (host) memory, while the GPU computes the inside region. Then, the CPU performs memory operations for the APT method and the data communication among the nodes with MPI. To perform the memory operation for the APT method and update the data for the next time step in the GPU, the data on the host memory is returned to the global memory. Although the data communication with MPI and the data transfer

from GPU to CPU tend to be bottlenecks, most parts of these data communications can be masked by the computation on the GPU by choosing an optimum number of subdomains.

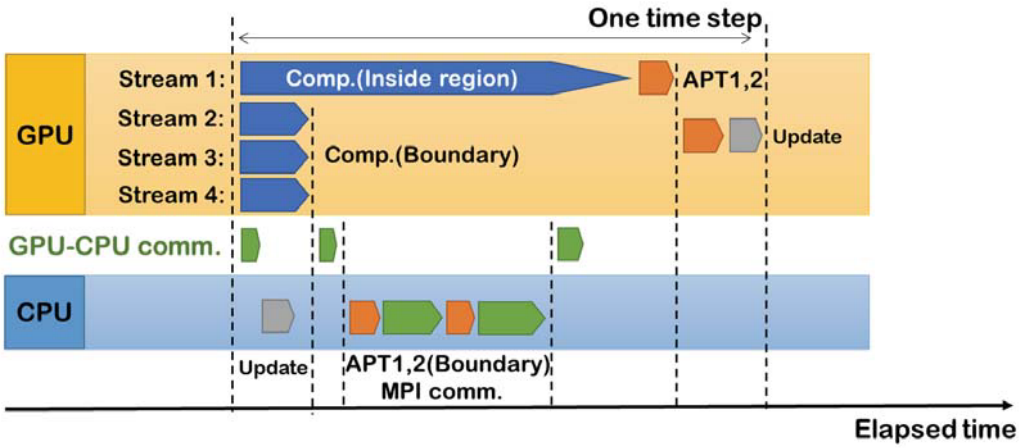

Figure 2. Computational diagram illustrating the overlapping method.

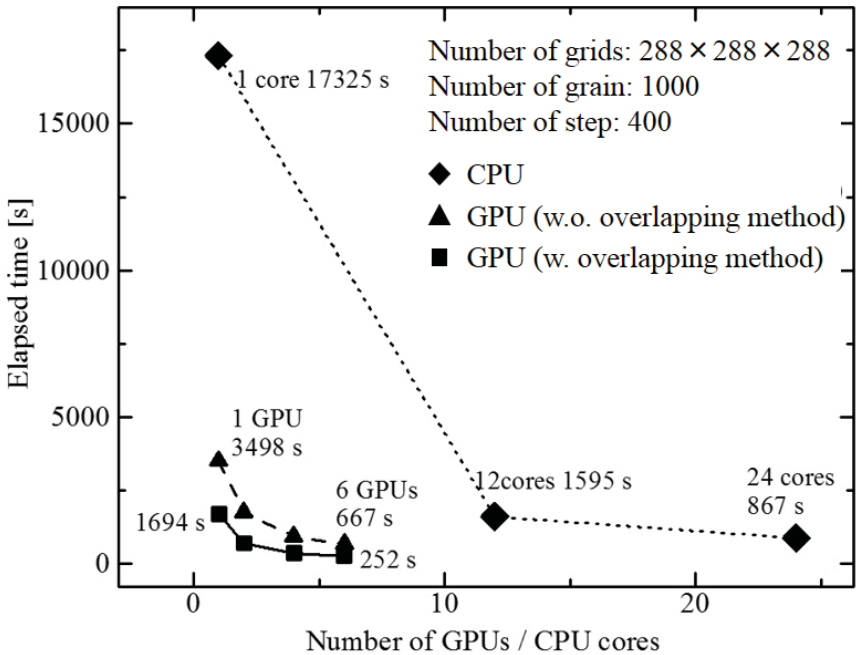

Figure 3. Comparison of the acceleration performances obtained by multiple-GPU and multiple-CPU computations.

Performance on GPU-cluster Computer

We first evaluated the performance of the multiple-GPUs computing technique developed on a GPU-cluster computer installed in our laboratory. The GPU-cluster computer used comprises four computational nodes, with two GPUs and two Intel Xeon E5-2690 CPUs with eight cores mounted. Thus, eight GPUs are installed on the cluster. The data communication was performed using QDR InfiniBand.

Using the GPU-cluster computer, we performed 3D MPF simulations of polycrystalline grain growth. The size of the whole computational domain was 144 × 144 × 144 μm^3 and it was

discretized by a regular finite difference grid of dimension 288 × 288 × 288. The initial microstructure was composed of 1000 crystal grains, and the number of computation steps and the time increment were 400 and 0.51 s, respectively. Other parameters used in the simulation were as follows: temperature T = 800 K, interfacial energy σ = 0.5 J/m^2, physical interfacial mobility $M = M_0\exp(-Q/kT)$, where pre-exponential factor M_0 = 6.2 × 10^{-6} m^{4}K/J, activation energy Q = 2.1 × 10^{-19} J, and interfacial thickness δ = 3.5 μm.

Figure 3 shows the total elapsed time for the MPF simulation utilizing multiple-GPUs computing with and without the overlapping method. The result obtained using multiple-CPU computing is also indicated in the same figure. It can be seen that the elapsed time for multiple-CPUs computing reduces as the number of CPU cores increases, whereas for GPU computing without the overlapping method, the elapsed time is decreased very significantly. Furthermore, we found that multiple-GPU computing with the overlapping method further improved the performance, because the overlapping method can completely mask the data communication time with the computation time. These results demonstrate that the multiple-GPUs computing technique with the overlapping method facilitates efficient 3D MPF simulations performances.

Large Scale 3D Multi-phase-field Simulation on TSUBAME2.5 Supercomputer

In the preceding section we demonstrated that the multiple-GPUs computing technique is very efficient. We implemented the technique on the TSUBAME2.5 supercomputer at the Tokyo Institute of Technology [14]. The main part of the TSUBAME2.5 supercomputer consists of 1408 computational nodes, and each node is equipped with three TESLA K20X GPUs. Thus, the total number of GPUs in the system is 4224. Each node also has two Intel CPU Xeon 5670, 54 GB DDR3 main memory and two QDR InfiniBands.

Figure 4 shows polycrystalline grain growth obtained using a grid size of 1024 × 1024 × 1024 grids on 256 GPUs of the TSUBAME2.5 supercomputer. In this simulation, we took into account 32768 crystal grains in a cubic region 0.512 × 0.512 × 0.512 mm^3. Performing this same simulation on a single CPU core would require approximately one month of running time. In contrast, using the multiple-GPUs computing technique for large-scale 3D MPF simulation on the supercomputer, the running time required was less than two hours.

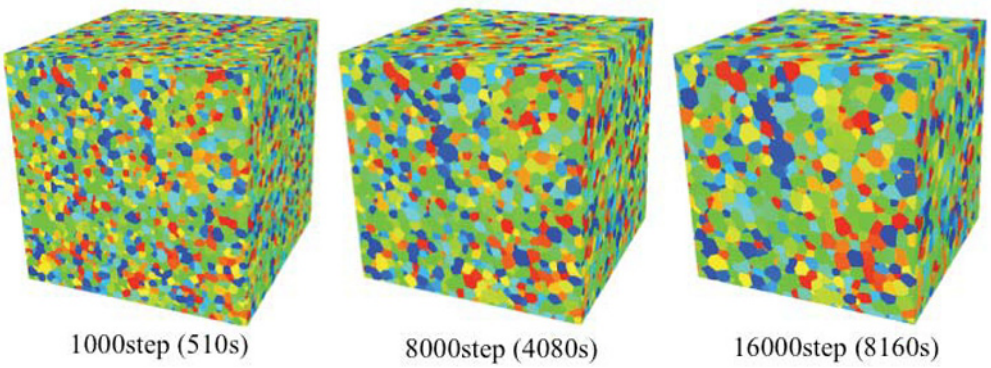

Figure 4. Polycrystalline grain growth on 1024 × 1024 × 1024 grids using 256 GPUs of the TSUBAME2.5 supercomputer.

Conclusion

In this paper, we discussed our multiple-GPUs computing technique that facilitates efficient performance of large scale 3D MPF simulations, and our overlapping method that facilitates high performance using a large number of GPUs by masking the data communication time with the computation time. We demonstrated that this overlapping method significantly reduces the elapsed time for 3D MPF simulations. We also showed that very large scale 3D MPF simulations of polycrystalline grain growth with up to 1024^3 grids can be successfully performed using 256 GPUs. The realistic 3D morphology of microstructures obtained by large scale MPF simulations such as this are useful for comparing experimentally observed microstructures and understanding the microstructure evolution mechanism.

Acknowledgement

This research was supported by the "Joint Usage/Research Center for Interdisciplinary Large-scale Information Infrastructures" and "High Performance Computing Infrastructure" in Japan, KAKENHI, Grant-in-Aid for Scientific Research for Young Scientists (A) 25709002, and Challenge Exploratory Research 25630322 from the Japan Society for the Promotion of Science (JSPS).

References

1. I. Steinbach, F. Pezzola, B. Bestler, M. Seeβelberg, R. Perieler, G.J. Schmiz, and J.L.L. Renzende, "A Phase Field Concept for Multiphase Systems," *Physica D*, 94, 135-147, 1996.
2. I. Steinbach and F. Pezzola, "A Generalized Field Method for Multiphase Transformations using Interface Fields," *Physica D*, 134, 385-393, 1999.
3. D. Fan and L-Q. Chen, "Computer Simulation of Grain Growth using A Continuum Field Model," *Acta Materialia*, 45, 611-622, 1997.
4. I. Steinbach, "Phase-field Model for Microstructure Evolution at the Mesoscopic Scale," *Annual Review of Materials Research*, 43, 89-107, 2013.
5. I. Steinbach and O. Shchyglo, "Phase-field Modeling of Microstructure Evolution in Solids: Perspectives and Challenges," *Current Opinion in Solid State and Materials Science*, 15, 87-92, 2011.
6. M. Ohno and K. Matsuura, "Quantitative Phase-field Modeling for Two-phase Solidification Process Involving Diffusion in the Solid," *Acta Materialia*, 57, 5749-5758, 2010.
7. Y. Suwa, Y. Saito, and H. Onodera, "Parallel Computer Simulation of Three-dimensional Grain Growth Using the Multi-Phase-Field Model," *Materials Transactions*, 49, 704-709, 2008.
8. A. Yamanaka, T. Takaki, T. Aoki, and T. Shimokawabe, "Multiphase-field Simulation of Austenite-to-Ferrite Transformation Accelerated by GPU Computing," *Journal of Computational Science and Technology*, 6, 182-197, 2012.
9. S.G. Kim, D.I. Kim, W.T. Kim, and Y.B. Park, "Computer Simulation of Two-dimensional and Three-dimensional Ideal Grain Growth," *Physical Review* E, 74, p. 061605, 2006.
10. The Portland Group Inc., *CUDA Fortran Programming Guide and Reference*, (2012)
11. M. Okamoto, A. Yamanaka, T. Shimokawabe, and T. Aoki, *Transactions of JSCES*, 2013, pp. 20130018, 2013. (In Japanese)
12. G. Ruetsch and M. Fatica, *CUDA Fortran for Scientists and Engineers*, (Elsevier, 2013).
13. Tsubame, http://www.gsic.titech.ac.jp/en/tsubame

Microstructure/Property Relationship in 3D: Deformation and Damage

2nd International Congress on 3D Materials Science
Edited by: Dominique Bernard, Jean-Yves Buffière, Tresa Pollock, Henning Friis Poulsen, Anthony Rollett, and Michael Uchic
TMS (The Minerals, Metals & Materials Society), 2014

FINITE ELEMENT SIMULATION AND EXPERIMENTAL ANALYSIS ON FATIGUE BEHAVIOR OF SiC_n/Al CO–CONTINUOUS COMPOSITES

Yu Liang[1,2], Kun–Peng Yang[2], Xiao–Dong Nong[2], Yan–li Jiang[1,2*], Nan–nao Ge[3], Ming Fang[3]

[1] Guangxi Scientific Experiment Center of Mining, Metallurgy and Environment, Guilin, 543004, China
[2]Key Laboratory of New Processing Technology for Nonferrous Metals & Materials, Ministry of Education, Guilin University of Technology, Guilin, 543004, China
[3]Zhejiang Tianle New Material Technologic Co. Ltd, Shengzhou, 312400, China

Keywords: Fatigue behavior, Finite Element, SiC_n/Al alloy, co–continuous composite,

Abstract

The co–continuous ceramic/metal composite (referred to as C^4 composites) are becoming an important class of materials as the result of the development of a number of new techniques for fabricating composites with interpenetrating macrostructures. In this paper, the fatigue endurance behaviors of three three–dimensional (3–D) continuous SiC ceramic network reinforced ZL111 Al alloy composites (T6–treated SiC_n/ZL111Al) were simulated by the finite element method (FEM). The finite element simulation showed that the stress concentration, due to the presence of continuous SiC ceramic network reinforcements, produces controlled crack growth and higher stresses, which are related to regular energy release by the material during fracture. The need for higher stresses for a crack to propagate reveals the material's microstructural strength. Experimental analysis showed fatigue life for specimen was 4.8×10^5 cycles for 200 MPa, R=-1.0, and 6.5×10^5 cycles for 95 MPa, R=-0.05. The number of cycles to failure predicted numerically is higher than the experimental one. This difference is attributed mainly to an upper stage of fatigue crack growth, particularly, the interaction between fatigue crack growth and growth that cannot be accounted for in the numerical model.

Introduction

Al metal matrix composites (Al–MMCs) have highlighted a commercially competitive advantage largely owing to their relatively low cost and ease of processing. Among Al–MMCs, the co–continuous ceramic/metal composites (referred to as C^4 composites), also called the interpenetrating phase composites (IPCs) have aroused extensive interest [1–5]. The C^4 composites can provide the desirable mechanical properties including high specific stiffness, high plastic flow strength, creep resistance, good oxidation and corrosion resistance, due to their three–dimensional (3–D) network structure having two, distinct, interconnected phases, namely one of a soft metallic alloy (generally Al alloy or an intermetallic) and one of a hard ceramic phase (generally Al_2O_3 or SiC). It is reported that the unique arrangement of matrix and reinforcement provides high strength–to–weight and stiffness–to–weight ratios which are ideal for use in the dry friction and wear applications [6–10]. Our previous experiment shows that the C^4 SiC_n/Al (n means network structure) can be used as brake disk material for China Railway High–speed trains (CRH) for its excellent wear properties [11,12]. Numerical calculations have been done to predict the behavior of compression, stiffness, strength, and energy dissipation of the C^4 composites [13,14]. In the literature, fatigue studies on metal–ceramic composites are generally based on particle–reinforced aluminium[15,16] or, more rarely, fibre–reinforced aluminium[18]. To the authors' knowledge, to date only studies based on static

tensile/compressive stress[14] or crack propagation[13] have been performed on C^4 composites, while a high cycle fatigue characterisation has not been undertaken. In this paper, the 3–D finite element model is developed to simulate the elastic and plastic behavior of the SiC_n/Al composites based on their macrostructures. The relationship between macroscopic mechanical response and the macrostructures are discussed.

Crystal structures and calculation details

The SiC_n/Al composites were prepared by infiltration of a molten ZL111 Al alloy liquid (ZL111 Al alloy that had the following chemical composition (in wt%, 8.80Si /1.30Cu /0.30Mn /0.30Mg /0.20Ti /0.3Zn, balance Al) into the SiC porous preform struts using a low–pressure casting. The processing and physical properties of the composites were described in greater depth in Ref [9–12]. Fig.1 (a) shows the typical macrostructure of SiC_n/Al composite, where the brighter phase is Al alloy matrix and the darker phase is SiC struts. It can be seen that the molten Al alloy is completely infiltrated into the SiC struts. The volume fractions of the phases are approx. 75% Al and 25% SiC. The appearance of the phases suggests that the macrostructures are in agreement with the C^4 composites SiC/Al constituent described in Ref [1–8]. In the production of metal matrix composite, one of the subjects of interest when choosing the suitable matrix/reinforcement is the interaction in its interface. In some cases, reactions that occur in the interface between a matrix and its reinforcement have been considered harmful to the final mechanical properties and are usually avoided. In others, the interfacial reactions are intentionally induced when the new layer formed at the interface acts as a strong bonder between the phases.Many works aimed to obtain a suitable matrix/reinforcement system, that provides minimum and controlled reaction and fine and thermally stable ceramic struts dispersed uniformly in the metal matrix. The present works led to the development of the in situ composites, in which the SiC struts are embedded in a metal matrix during the composite fabrication. As a result of the process the interface between the materials is clean and a strong interfacial bonding is obtained. The simple two–phase–interpenetrating cell geometry is used to represent the composites for the simulation. The SiC struts have pore diameters of 3 mm. In order to represent the SiC struts microstructure, previous structural foam researchers have successfully used space filling Kelvin cells [15]. A Kelvin cell is a tetrakaidecahedron, a 14–sided polyhedron comprised of six squares and eight hexagonal faces. In the present work, initial modeling of a Kelvin cell is done using solid modeling software SOLIDWORK. The space inside and outside this cell is filled with Al alloy, assumes to be a macroscopically homogeneous for modeling purposes. A schematic diagram is shown in Fig. 1(b).

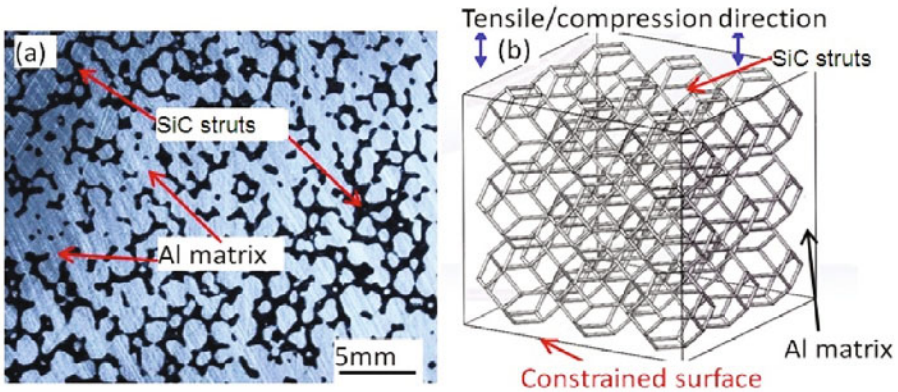

Fig.1 (a) Macrostructure of SiC_n/Al composite; (b) Simulated model of SiC_n/Al composite;

We make some assumptions for simulating the mechanical properties of composites as follows: the SiC struts, ribs are continuous and their size is the same; The actual cross–section of ribs of

the SiC struts used in experiments is close to a rounded shape and hence is approximated as an rounded; The impurities is nonexistent at the interface of SiC struts and Al alloy in the simulations for simplicity. The cosssectional area of the ribs is decided such that the overall volume fraction of the SiC struts in the composites is approximately 25%, same as that of the preform used in the experiments. Finite element analyses are carried out using ANSYS/standard structural analysis software. A four node tetrahedron element with linear interpolation is used to discretize the unit cell. The unit cell model has a total of 91523 elements and 16937 nodes. The elastic constants of Al alloy and the SiC struts (from experiments) are assigned to the two phases of the composites. The mechanical properties of SiC struts, elasticity modulus=450 GPa, ν=0.10, density=3.15 g/cm^3, yield limit=14 MPa, shear modulus=192 MPa. The stress–strain response of Al alloy (Young's modulus =68.9 GPa, ν =0.33, yield stress =245 MPa at 0.2% strain, ultimate stress=330 MPa (at 6% strain). The Al alloy is regarded as visco–plastic material described by a new cyclic constitutive model provided in Ref [11–13]. Simulate mechanical properties under tensile, under compressive loads, cyclic load/unload, by displacing the nodes uniformly on the top face of the cell in the *Z*–direction shown in Fig.1 (b). The *xy* plane is constrained and the opposite plane is required to displace as a plane during deformation.

Results and discussions

Microstructure of the SiC_n/Al composite

Fig.2 shows the microstructure of interface of SiC_n/Al composite. Micrograph of porous SiC performs before infiltration is shown in Fig. 2(a). It can be seen that the pores are similar hexagonal holes, interconnected and uniform in size and distribution. The porosity of the SiC preform measured by mercury porosimetry is ~45% (volume fraction), average diameter of pore is 1.5~2.5 mm, and average diameter of the ribs is ~0.5 mm.

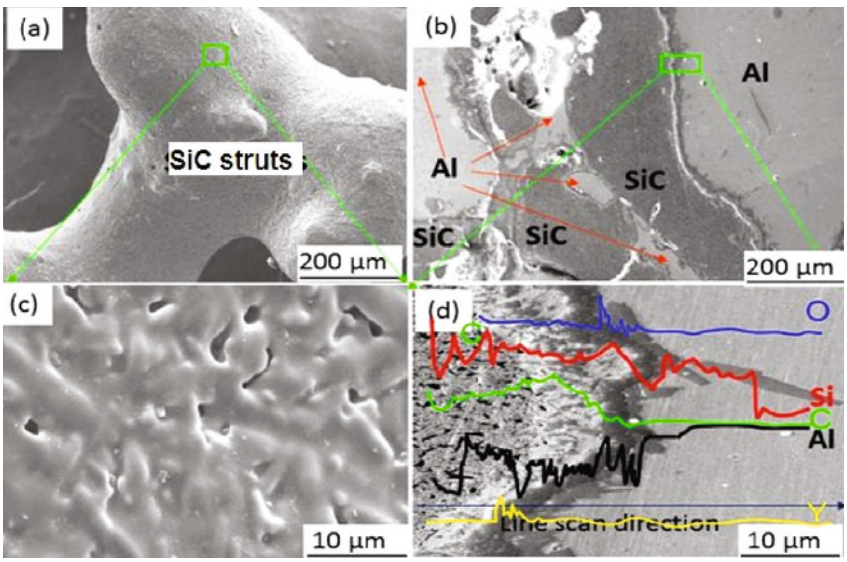

Fig. 2 (a) SiC struts ;(b) interface of SiC_n and Al alloy; (c) surface of SiC struts; (d) line scanning analysis of primary elements in interface of SiC_n/Al composite.

Micrograph Fig.2 (b) shows the typical SEM image, from which the molten Al alloy completely infiltrats the SiC struts perform, density measurements shows that the composites are >99% of theoretical one. The appearance of the phases suggest that these microstructures were in agreement with the co–continuous SiC/Al micro constituent described in the articles mentioned in the introduction, but in present work their morphology is finer as Y, Sr elements are used to

reduce the surface tension of the molten Al alloy liquid to improve the wettability of the SiC struts and Al matrix. From Fig.2 (b), no bulk second phases can be observed in the composites, and a SiO_2 thin film may be seen at localized positions on the Al grain boundaries in the infiltrated cells. Fig.2 (c) shows a continuous SiO_2 layer on the SiC struts. It will protect the inner SiC from the attack of molten Al. Line scanning analysis suggests the SiO_2 film is 1～4 μm in thickness, forms at the Al–SiC interface shown in Fig.2 (d). So the interface between the Al and SiC struts is clean and a strong interfacial bonding is obtained.

Stress–strain and Fatigue Behavior

Static tensile tests were performed on at least ten specimens manufactured from the SiC_n/Al composites. Fig.3 (a) shows representative experimental and simulated stress–strain curves for composites. The non–linear behaviour of the composites is in agreement with observations of Daehn et al and F. Scherm [14, 15]. This behaviour can be explained by the combination of an elastic deformation of the SiC preform accompanied by a plastic deformation of the metal at higher stresses. It is difficult to determine a yield stress for these materials with good enough reproducibility. The 0.2% yield stress was determined using the Young's modulus measured with acoustic resonance technique. The ultimate tensile strength (UTS) of these composites reached values beyond 375 MPa with a fracture strain around 0.5%. Depending on casting conditions, unreinforced ZL111 Al alloy has an UTS from 300 to 350 MPa and a fracture strain from 0.5 to 3% [16]. Hence, all composites are considerably stronger and slightly less ductile than the unreinforced Al alloy. The samples were loaded in the first cycle until a stress of 100 MPa, then unloaded to a stress of 15 MPa. In the following cycles the max applied stress was increased in 20 MPa steps. The stress–strain curves of these cyclic experiments is shown in Fig. 3(b). The failure of the sample occurred in cycle number 16 at 307 MPa stress and 0.9% strain. Hysteresis loops for cycle number 5, 10 and 15 are marked. They broaden with increasing cycle numbers and stresses. Pseudo elastic modulus decreases from the first cycles to the last cycle. This tendency gives hints for an increasing an elastic effect of the material at higher loads. A possible explanation can be seen in the growth of micro–cracks with increasing cycle number. The number of cycles to failure predicted numerically is higher than the experimental one.

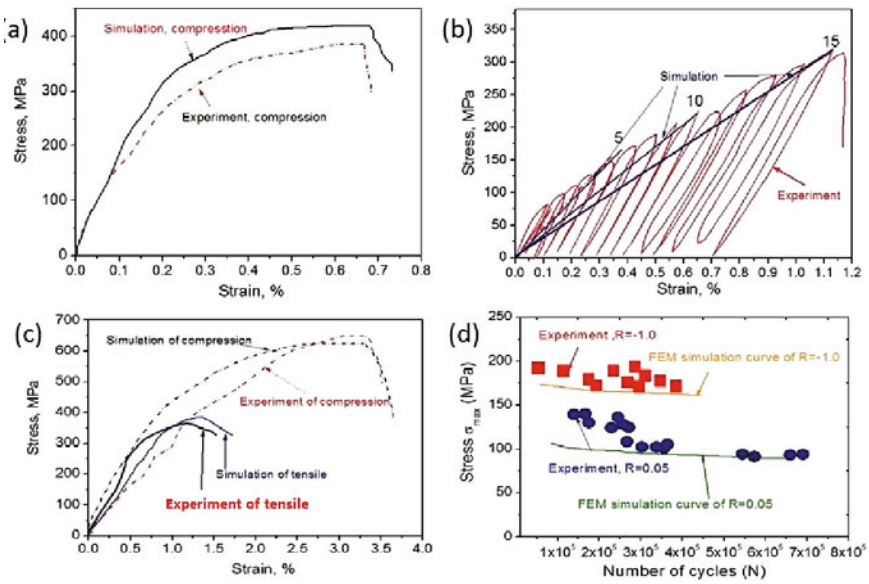

Fig. 3.Experimental and simulated curves for SiC_n/Al; (a) Stress–strain curves; (b) Stress–strain curves for cyclic load/unload; (c) curves under tensile and compressive load; (d)Stress versus cycles to failure curves(room temperature, stress ratio R =0.05 and -1);

Fig. 3(c) shows the tensile behaviour of the composite in comparison to its compression behaviour. Measured values for compressive strength were approximately 710 MPa with 2% compressive strain. The ultimate compressive strength is thus about 2 times higher than the UTS 410 MPa, the strain to failure for compression is about 3 times higher than for tension. The non–linear stress–strain behaviour was also found in the compression tests. Cyclic fatigue tests were carried out at room temperature and at 150 °C. The ratio of applied maximum and minimum stress $R=\sigma_{min}/\sigma_{man}$ was either R=0.05 or R=-1. The stress versus cycles to failure curves is shown in Fig. 3(d). Compared the *S*–*N* curves for tension–compression and tension–tension cycle types on the basis of maximum stress, it can be found that the two *S*–*N* curves have nearly the same slope. Fatigue life for specimen is 4.8×10^5 cycles for 200 MPa, R =-1.0, and 6.5×10^5 cycles for 95 MPa, R=-0.05. This was in agreement with previous observations, concluding that the SiC struts reinforcement strongly affects both the static properties, and the failure mechanisms during quasi–static tension–compression loading [13–15]. The displacement, stress and strain of the model under compression load are shown in Fig 4. The maximum stress occurred at the interfacial boundary between SiC struts and Al matrix. From Fig 4(a, b) the elastic deformation in the ceramic is accommodated by plastic deformation in the metal phase. The properties suggest C^4 composites as excellent energy dissipative elements in advanced structures or armor by controlling volume fraction and tailoring geometric arrangements to meet different requirements. It should be noted that different mechanical behavior between SiC struts and Al matrix, difference of elasticity modulus of two constituents occasion difference of generated deflection. Additionally, the deformation behavior of material shows a great difference in near interface of two constituents. This is caused due to the 3–D connected structural characteristic of the material, the force on each rib affects other adjacent rib of the SiC struts, stress intensity is related to ribbed–orientation. The degree of stress concentration shows that a suitable interfacial bonding can improve the material performance. Compared to the conventional composites, the C^4 composites are 3–D multi–directionally reinforced, are less dependent on material distribution, and simultaneously provide relatively high stiffness, strength and energy absorption in all directions. The large deformation appears inside Al matrix. Al alloy matrix and SiC struts can restrict each other to prevent from producing the strain under the load. Namely, the SiC struts change the distribution of stresses of composites, which can restrict the extraneous stretch or compression, and this structural has the tensile or compression strength [13–16].

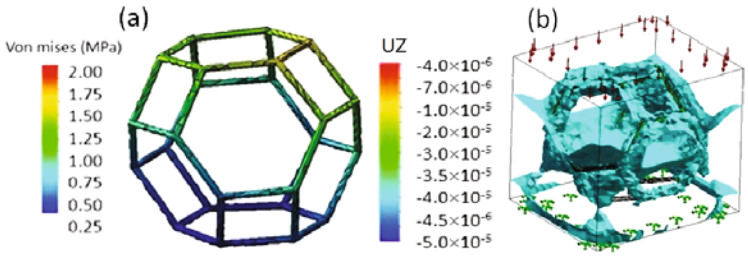

Fig. 4 Stress and strain of SiC_n/Al composites under compression load 1.5 MPa; (a) Von Mises stress on SiC struts, max 2.07 MPa; (b) strain on Al matrix, max URES displacement -5.0×10^{-5};

Conclusions

SiC_n/Al composites fabricated by infiltration of SiC preforms with melted Zl111 Al alloy with T6 heat treatment exhibit high mechanical properties. The ultimate tensile strengths of the composite is up to 375 MPa at a failure strain up to 0.6%. The compression strength is up to 710 MPa with 2% strain to failure. Fatigue life for specimen was 4.8×10^5 cycles for 200 MPa, R=-1.0, and 6.5×10^5 cycles for 95 MPa, R=-0.05. Simulated data shows there is different mechanical behavior between SiC struts and Al matrix. A suitable interfacial bonding can improve the

composite performance; Due to structural characteristic of SiC, the force on each rib affects other adjacent rib, Al and SiC restrict each other to prevent from producing the strain.

Acknowledgements

This work was supported by offends pass item (No. 2013YB112), province science and technology in the Guilin offends pass item (No. 1346011–5), and start–up funding of Guilin university of technology (No. 002401003330 and No. 002401003329).

References

[1] Yu L, Jiang Y L, Lu S K, et al. FEM for brake discs of SiC 3D continuous ceramic reinforced 7075 aluminum alloy for CRH3 trains applying emergency braking[J]. Applied Mechanics and Materials, 2012, 120: 51–55.

[2] Yu L, Jiang Y L, Lu S, et al. Numerical simulation of brake discs of CRH3 high‐speed trains based on Ansys[C]//Proceedings of the 1st World Congress on Integrated Computational Materials Engineering (ICME). John Wiley & Sons, Inc., 2011: 183–188.

[3] Jiang L, Jiang Y, Yu L, et al. Thermal analysis for brake disks of SiC/6061 Al alloy co–continuous composite for CRH3 during emergency braking considering airflow cooling[J]. Transactions of Nonferrous Metals Society of China, 2012, 22(11): 2783–2791.

[4] Jiang L, Jiang Y, Yu L, et al. Experimental study and numerical analysis on dry friction and wear performance of co–continuous SiC/Fe–40Cr against SiC/2618 Al alloy composites[J]. Transactions of Nonferrous Metals Society of China, 2012, 22(12): 2913–2924.

[5] Yu L, Zhao J, Yue X Y, et al. Microstructure and properties of graphite embedded SiC composite by coating method [J]. Advanced Materials Research, 2010, 105: 855–858.

[6] Ding L, Jiang G, Yao X, et al. New progress of co–continuous ceramic composites [J]. Bulletin of the Chinese Ceramic Society, 2012, 5: 023.

[7] Yu, L., Jiang, Y., Lu, S., Ru, H. and Fang, M. (2012) Numerical simulations of compression properties of SiC/Fe-20Cr co–continuous composites, in 1 International Conference on 3D Materials Science (eds M. De Graef, H. F. Poulsen, A. Lewis, J. Simmons and G. Spanos), John Wiley & Sons, Inc., Hoboken, NJ, USA. doi: 10.1002/9781118686768.ch13.

[8] Zhao L Z, Zhao M J, Cao X M, et al. Thermal expansion of a novel hybrid SiC foam–SiC particles–Al composites [J]. Composites Science and Technology, 2007, 67(15): 3404–3408.

[9] Qin Y W, Lu S K. Simulation and experimental mechanical properties of SiC_n/2024 Al alloy co–continuous composites [J]. Advanced Materials Research, 2013, 712: 997–1001.

[10] Cree D, Pugh M. Dry wear and friction properties of an A356/SiC foam interpenetrating phase composite [J]. Wear, 2011, 272(1): 88–96.

[11] Zhang S Y, Qu S G, Li Y Y, et al. Two–body abrasive behavior of brake pad dry sliding against interpenetrating network ceramics/Al–alloy composites [J]. Wear, 2010, 268(7): 939–945.

[12] Agrawal P, Conlon K, Bowman K J, et al. Thermal residual stresses in co–continuous composites [J]. Acta Materialia, 2003, 51(4): 1143–1156.

[13] Wang L, Lau J, Thomas E L, et al. Co‐continuous composite materials for stiffness, strength, and energy dissipation[J]. Advanced Materials, 2011, 23(13): 1524–1529.

[14] Zhao M, Li N, Zhao L, et al. Numerical simulations of compression properties of SiC/Al co–continuous composites[M]//Computer and Computing Technologies in Agriculture IV. Springer Berlin Heidelberg, 2011: 480–485.

[15] Jhaver R, Tippur H. Processing, compression response and finite element modeling of syntactic foam based interpenetrating phase composite (IPC)[J]. Materials Science and Engineering: A, 2009, 499(1): 507–517.

[16] Bernal Ostos J, Rinaldi R G, Stucky G D, et al. Deformation stabilization of lattice structures via foam addition [J]. Acta Materialia, 2012, 60(19): 6476–6485.

2nd International Congress on 3D Materials Science
Edited by: Dominique Bernard, Jean-Yves Buffière, Tresa Pollock, Henning Friis Poulsen, Anthony Rollett, and Michael Uchic
TMS (The Minerals, Metals & Materials Society), 2014

INFLUENCE OF THE CASTING MICROSTRUCTURE UPON THE TENSILE BEHAVIOUR IN A319 Al-Si ALLOY INVESTIGATED BY X-RAY TOMOGRAPHY AND DIGITAL VOLUME CORRELATION

Long Wang[1], Nathalie Limodin[1], Ahmed El Bartali[1], Julien Rethore[2], Jean-François Witz[1], Rian Seghir [1], Eric Charkaluk[1], Jean-Yves Buffiere[3]

[1]Laboratoire de Mécanique de Lille (LML), CNRS UMR 8107; Cité Scientifique; Villeneuve d'Ascq, Nord, 59650, France
[2]Laboratoire de Mécanique des Contacts et des Structures (LaMCoS), CNRS UMR 5259; 18-20, rue des Sciences; Villeurbanne, Rhône, 69621, France
[3]Laboratoire Matériaux, Ingénierie et Sciences (MATEIS), INSA-Lyon, CNRS UMR 5510; 20 Av. Albert Einstein; Villeurbanne, Rhône, 69621, France

Keywords: Aluminum-silicon alloys, Digital Volume Correlation, X-ray tomography

Abstract

Aluminum alloy automotive parts produced by the Lost Foam Casting (LFC) process have coarser microstructure and porosity defects than parts produced with conventional casting processes at faster cooling rates. This coarse microstructure has a major influence on the fatigue properties and crack initiation. In order to study its influence upon the mechanical behaviour, an experimental protocol has been set up using X-ray tomography and 3D Digital Volume Correlation (DVC). The present work focuses on the use of this protocol to study the influence of the casting microstructure upon the tensile behaviour. The 3D cracks were observed to initiate at large pores and microshrinkage cavities and then to propagate along the hard inclusions towards the free surface when cracks originate from a subsurface pore. The validated experimental protocol is presently applied to in-situ fatigue tests realized with synchrotron tomography and a newly developed DVC platform in order to analyze the damage micromechanisms of this alloy subjected to low cycle fatigue test.

1. Introduction

In the automotive industry, the conventional die casting process is progressively being replaced by the Lost Foam Casting (LFC) process for the purpose of geometry optimization, cost reduction and consumption control. However, aluminum alloy automotive parts produced by the LFC process have a coarser microstructure and more porosity defects than parts produced with conventional casting processes at faster cooling rates. This microstructure has a major influence on the fatigue properties. Above a critical size, pores [1] play a decisive role by providing preferential crack initiation sites. However, an influence of oxides [2], iron-based intermetallics [3] and Si particles [4] is also observed. The cracks can initiate at defects present in bulk of the material and, in low cycle fatigue, the failure often results from multicracking rather than from a single crack. In order to study the influence of this microstructure upon the mechanical behaviour in bulk, an experimental protocol, which allows following the cracks initiation and propagation in 3D, has been set up using X-ray tomography and Digital Volume Correlation

(DVC). The present work focuses on the use of this protocol to study the influence of the casting microstructure upon the tensile behaviour.

2. Experimental procedure

The alloy used in this study is an A319 Aluminum Silicon alloy (Table I), which is used for manufacturing of cylinder heads and is casted by a LFC process. Small specimens (Figure 1 (a)) were extracted from automotive cylinder heads provided by PSA Company by electro discharge machining. The screening of specimens was realized prior to the tensile test using a laboratory computed X-ray tomography system V-Tomex (MATEIS laboratory, Lyon, France) in the fast scan mode, i.e. the scan lasts about 5 minutes, at a 4.5 µm voxel size; these medium resolution images allow revealing the size and shape of the large pores inside the specimens gauge length rapidly. The chosen specimens have no large defects near the shoulders while they have defects with a size compatible with the specimen cross-section in the gauge length.

Table I: Chemical composition of LFC A319 Al-Si alloy (mass percentage)

Al	Si%	Mn%	Fe%	Mg%	Cu%	Zn%	Ti%	Ni%	V%	Zr%	Sr(ppm)	P(ppm)
bal.	7.18	0.15	0.43	0.32	3.17	0.19	0.05	0.010	0.020	0.006	0.002	0.010

The selected specimens were then polished on both faces up to a ¼ µm surface finish. The matrix, i.e. the material without pores, of these specimens was segmented from the X-ray tomography 3D image and a geometric model with a volumetric tetrahedral grid was created using Avizo software. The model was then used for finite element simulation using Abaqus software in order to predict the most strained region under tensile loading and to focus the subsequent in-situ observation by high resolution X-ray tomography on this small volume.

The in-situ tensile test was performed at the MATEIS laboratory. A 80kV acceleration voltage was selected to enable for at least 10% transmission of incoming X-ray beam. The specimens were placed on the rotating stage in the tomography chamber between the X-ray source and the detector. A set of 900 radiographies was recorded while the specimen was rotating over 360° along its vertical axis. An acquisition time per image of 500ms yields a scan duration of 45 min. An in-situ test rig [5] was installed in the tomography chamber in order to load the specimen (Figure 1 (b)). First, the specimen was scanned under minimum load with a voxel size of 1.7 µm and 1.695 µm separately in order to later assess the uncertainty of DVC [6]. The obtained image at 1.695µm was further used as a reference for DVC and for the 3D characterization of the iron-based intermetallics and Al_2Cu phase. Then the specimen was loaded step by step until fracture and a scan was performed at each step with a 1.695µm voxel size. Loading procedure is illustrated in Figure 1(c); the stresses for the 6 steps correspond to 147, 165, 176, 188, 192 and, 198 MPa respectively.

Besides, a larger sample of the same material was scanned with a voxel size of 3 µm in order to characterize the pores distribution in a much larger, hence more representative, volume, i.e. 70 mm^3 vs. 8.2 mm^3 for the studied tensile specimen.

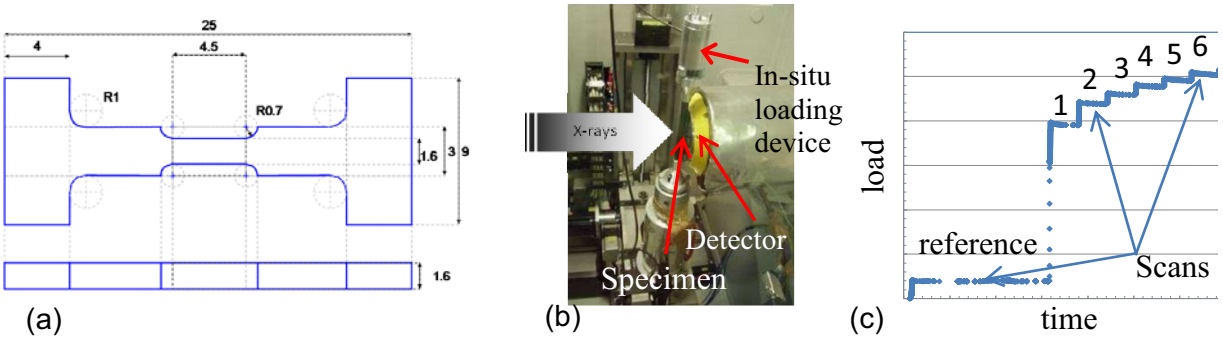

Figure 1. In-situ tensile test with: (a) specimen geometry (dimensions in mm), (b) in-situ test rig inside the tomography chamber and (c) the loading procedure

The images processing and pores analysis were performed with Avizo software. Feret diameter, which is the distance between the two farthest points on the surface of an object, was used to characterize the size of pores. The granulometry analysis, which allows calculating the thickness distribution of interconnected phases such as iron intermetallics and Al_2Cu phase, was performed with the "Analysis_3D" plugin in Fiji software [7].

The displacement field was measured with the DVC technique [8], which is an extension of the well-developed Digital Image Correlation (DIC) method, using the Mechanical Image Correlation (MIC3D) algorithm developed by J. Réthoré. The numerous and finely dispersed microstructural features inside the material, i.e. iron intermetallics and Al_2Cu phase, were successfully used as natural markers.

3. Results and discussion

3.1 3D characterization of specimens

An example of 3D rendering of pores in the bulk of a selected specimen is shown in Figure 2(a). Numerous large pores were found in the central part of the specimen and some of them having sharp shape produce large stress concentration. The volume fraction porosity in the studied tensile specimen is 0.88%, which is close to that measured in a larger volume of the material (1.17%). Distributions of pores in the small tensile specimen and in a larger volume are shown in Figure 2(b): the green (resp. red) curve and histogram stand for the pores distributions in the tensile specimen (resp. studied material) with a voxel size of 4.5 µm (resp. 3µm) in number and volume frequency, respectively. While the first peak in the number distribution corresponds to small rounded gas pores, the peak in the volume distribution corresponds to large microshrinkage cavities, which are fewer in number but do represent most of the pores volume fraction. The small difference between tensile test and the material for the first peak in the number distribution may be caused both by the different resolutions used, which controls the detectability of small pores, and by the scattering in microstructure. Figure 2(b) shows that the selected tensile specimen is representative of the studied cast material in terms of the size distribution of small pores and most importantly of large pores, which are believed to play the most important part in damage initiation, all the more so as they present sharp edges, which induce stress concentration. Consequently, all the in-situ observations during mechanical tests were performed with a higher

resolution but in a smaller volume, which was focused on a zone of interest where cracks were more likely to initiate, i.e. in the neighbourhood of large pores.

The 3D rendering of iron intermetallics and eutectic Al_2Cu phase in the studied alloy (Figure 3 (a) and (b)) explains why only a granulometry analysis could be used to characterize the thickness distribution of these highly interconnected phases (Figure 3(d)). As shown in Figure 3(c), although the average thickness of the interdendritic phases is almost the same, the maximum thickness of iron intermetallics is much larger. However, the maximum size of pores being more than 10 times larger than that of iron intermetallics, pores were assumed to be the most critical defects and the present analysis will focus on their influence upon tensile damage initiation.

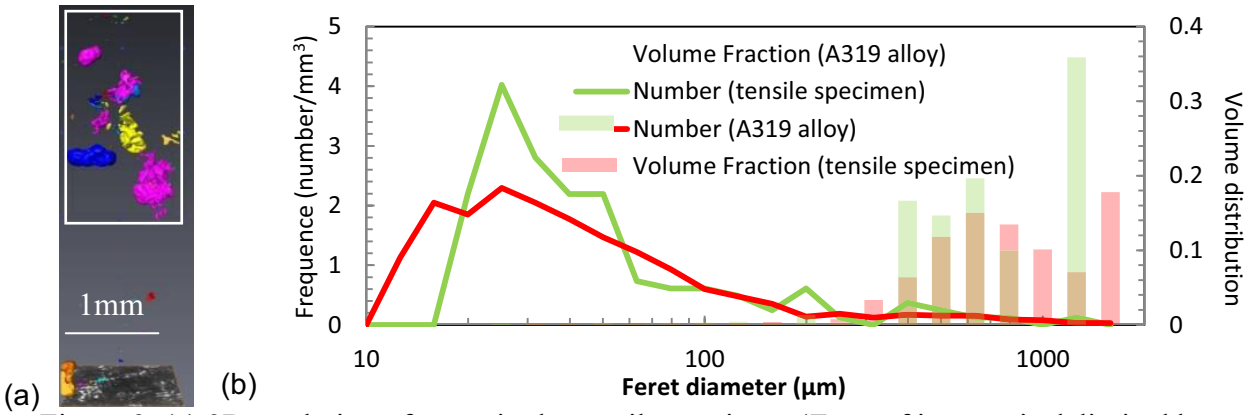

Figure 2. (a) 3D rendering of pores in the tensile specimen (Zone of interest is delimited by a white box) and (b) size distributions of pores for tensile and large specimens

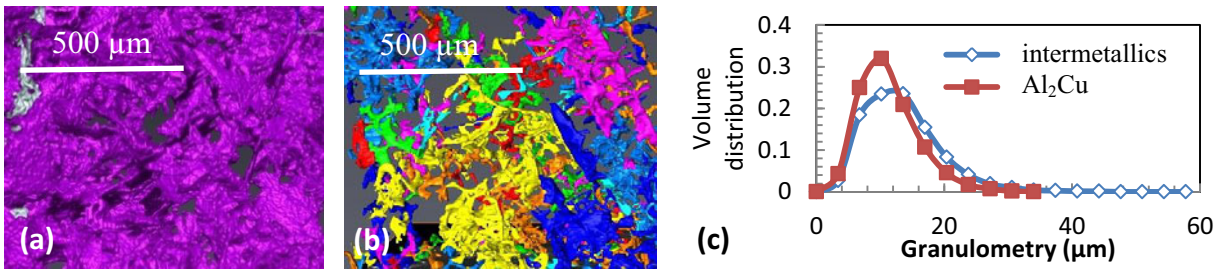

Figure 3. 3D rendering of (a) iron intermetallics. (b) Al_2Cu phase and (c) their thickness distributions in volume fraction

3.2 Full field measurements of in-situ tensile tests

An isotropic element with a 16 voxel edge was used for DVC in a zone of interest of 688 × 768 × 768 voxels^3 inside the specimen. 3D displacement field and longitudinal strain field along the loading direction at 198 MPa, which is the last step before failure, are shown in Figure 4 (a) and (b). A good correlation is observed between displacement discontinuities and strain localization in the measured field and the cracks. The correlation residual error is found to be, maximum at the cracks locations in Figure 4(c), thus it provides a less arbitrary way to extract the cracks than greyscale thresholding from the tomography image. The correlation between the cracks and pores and hard inclusions can be observed in Figure 4(d). Applying this method to the 6 loading steps, the 3D cracks are observed to initiate at large pores and microshrinkage cavities and then

to propagate along the hard inclusions towards the free surface when cracks originate from a subsurface pore.

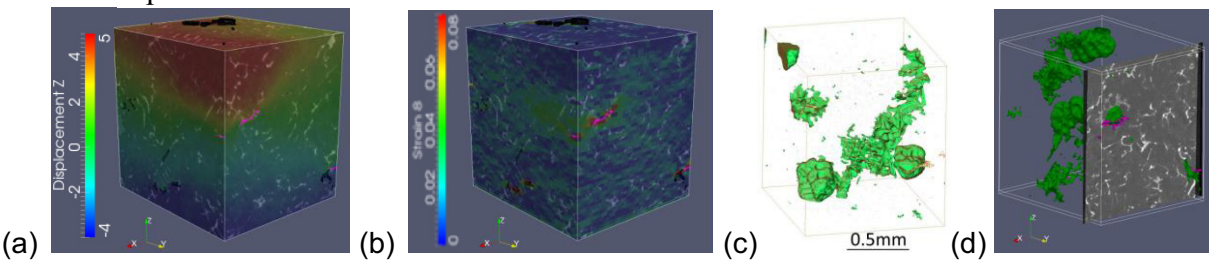

Figure 4. (a) 3D displacement field (in voxels) along loading direction (z-axis) and (b) ε_{zz} strain field with pores shown in grey and cracks shown in purple color; (c) comparison of residual error in yellow and cracks segmented (roughly) in red color; (d) correlation between cracks and pores and hard inclusions.

The strain field along the loading direction (ε_{zz}) was averaged over the whole volume at each loading step in order to determine the stress-strain curve in Figure 5(a). Compared with the experimental curve of the same material obtained from a conventional test, i.e. with appropriate extensometry measurement on larger specimens, the curve derived from DVC can be considered reliable. This stress-strain curve deduced from DVC is then used for FEM simulation of the porous matrix, and the strain field is shown in Figure 5(b). In the areas where large deformations around pores are observed, a good correlation is observed between the strain field measured from DVC (Figure 4(b)) and that computed from Abaqus; this emphasizes the influence of pores on strain localization under monotonic tensile loading. The displacement field measurement uncertainty [6] was calculated in order to assess the feasibility of DVC for A319 alloy, and DVC was considered reliable as the uncertainty was only 0.218 voxel for an element size of 16 voxels.

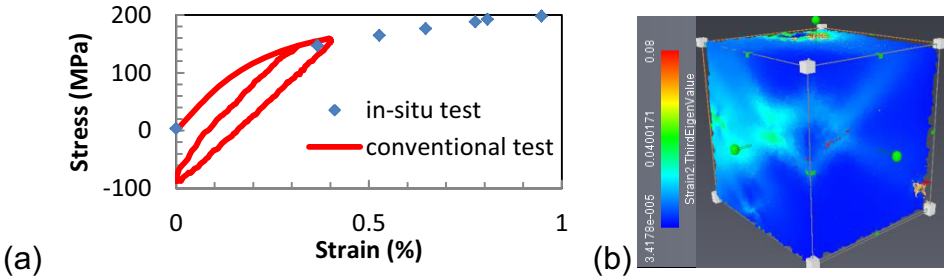

Figure 5. (a) Stress-strain curve, (b) 3D strain field (ε_{zz}) along the loading direction from FEM simulation with pores shown in yellow color and cracks shown in red color

4. Conclusions

In order to study the influence of the microstructure of a cast Al-Si alloy upon its mechanical behaviour, an experimental protocol has been set up and applied using X-ray tomography and digital volume correlation. The most suitable specimens were screened and characterized in 3D to reveal defects and hard inclusions in the interdendritic space with X-ray tomography. The correlation residual error, which is maximum at the cracks locations, constitutes a non-arbitrary way to extract the cracks. Cracks were observed to initiate at large pores and microshrinkage cavities and then to propagate along the hard inclusions towards the free surface. The stress-strain curve derived from DVC was considered reliable by comparison with an experimental curve obtained with conventional extensometry method. In the areas where large deformations

around pores were observed, a good correlation was observed between the strain field measured from DVC and that computed from FEM using Abaqus. This emphasized the influence of pores on strain localization under monotonic tensile loading. The validated experimental protocol presented here has already been applied to in-situ fatigue tests using synchrotron tomography and a 2D/3D image correlation platform based on C++ newly developed at LML laboratory and designed to process large data volumes in a limited amount of time. Preliminary results are presented in another paper in this conference.

5. Acknowledgements

The authors wish to thank the ANR (Agence Nationale de la Recherche) and PSA Peugeot Citroën for funding the study on Al-Si aluminum alloys.

6. References

1. Q.G. Wang, D. Apelian, D.A. Lados, "Fatigue behavior of A356-T6 aluminum cast alloys. Part I. Effect of casting defects," *Journal of Light Metals*, 1 (2001), 73-84.

2. X. Cao and J. Campbell, "The Nucleation of Fe-Rich Phases on oxide films in Al-11.5Si-0.4Mg cast alloys," *Metallurgical and Materials Transactions A*, 34 (7) (2003), 1409-1420.

3. S. Tabibian, E. Charkaluk, A. Constantinescuc, F. Szmytkaa, A. Oudin, "TMF-LCF life assessment of a Lost Foam A319 aluminum alloy," *International Journal of Fatigue*, 53 (2013), 75-81.

4. J-Y. Buffière, S. Savelli, P.H. Jouneau, E. Maire, R. Fougères, "Experimental study of porosity and its relation to fatigue mechanisms of model Al–Si7–Mg0.3 cast Al alloys," *Materials Science and Engineering A*, 316 (2001), 115-126.

5. J. -Y. Buffière, E. Maire, J. Adrien, J. -P. Masse, E. Boller, "In situ experiments with X ray tomography: an attractive tool for experimental mechanics," *Experimental Mechanics*, 50 (3) (2010), 289-305.

6. N. Limodin, A. El Bartali, L. Wang, J. Lachambre, J-Y. Buffière, E. Charkaluk, "Application of X-ray microtomography to study the influence of the casting microstructure upon the tensile behaviour of an Al–Si alloy," *Nuclear Instruments and Methods in Physics Research Section B: Beam Interactions with Materials and Atoms*, 324 (2014), 57-62.

7. V. Boulos, V. Fristot, D. Houzet, L. Salvo, P. Lhuissier, "Investigating performance variations of an optimized GPU-ported granulometry algorithm" in *: Design and Architectures for Signal and Image Processing (DASIP)*, Karlsruhe, Germany (2012), 1-6.

8. J. Réthoré, N. Limodin, J-Y. Buffière, F. Hild, W. Ludwig, S. Roux, "Digital volume correlation analyses of synchrotron tomographic images," *Journal of Strain Analysis for Engineering Design*, 46 (2011), 683-695.

2nd International Congress on 3D Materials Science
Edited by: Dominique Bernard, Jean-Yves Buffière, Tresa Pollock, Henning Friis Poulsen, Anthony Rollett, and Michael Uchic
TMS (The Minerals, Metals & Materials Society), 2014

3D EVALUATION OF INHOMOGENEOUS PLASTIC DEFORMATION OF GRAINS IN ALUMINUM ALLOY

M. Kobayashi[1] and Y. Kawamura[1]

[1]Toyohashi University of Technology;
1-1 Hibarigaoka Tenpackucho; Toyohashi, Aichi 441-8580, Japan

Keywords: Inhomogeneous deformation, grain, X-ray, microtomography.

Abstract

Inhomogeneous deformation in polycrystalline material is important matter, because the concentration of deformation relates with the origins of yield, fracture and recrystallization. Plastic strains in three-dimension during tensile deformation have been investigated by using the marker tracking method in synchrotron X-ray microtomography. Three-dimensional position of grains was detected by grain-boundaries visualizing method. The variation of deformation was measured for each grain. We investigated how much external deformation deformed grains heterogeneously.

Introduction

The plastic deformation of metallic material is caused by slip deformation. The slip system depends on crystal lattice. In polycrystalline materials, crystallographic orientations differ in each grain. Therefore, direction of slip system also varies. Grains deform inhomogeneously, because slip deformation is not continuous on grain boundary. The crystal plasticity model can relate slip deformation with deformation of the whole specimen. Furthermore, crystal plasticity model enables to connect deformation and microstructural evolution because the model can estimate lattice rotation caused by the plastic deformation. This has developed as deformation texture prediction model. The model developed by Taylor [1] is the most classical. The predictions that are brought by the Taylor model are generally analogous with actual texture development. However, the model has a tendency in which texture becomes sharper than that in experiment. Taylor model assumes that grains deform homogeneously by the strain identical to the whole specimen in order to keep continuous strain condition. As mentioned above, actual polycrystalline materials cannot deform homogeneously due to difference of crystallographic orientation. Therefore, prediction of deformation of texture evolution has been performed by modified models [2, 3] that allow strain relaxation thereafter. Here, the strain relaxation means effect of local inhomogeneous deformation. Various modified models have been developed and more successful predictions of deformation texture were achieved by them. These models are very useful for texture design and engineering. However, it is necessary to customize strain relaxation parameters to alloys. Unclear point exists in the models, i.e. why is such level of strain relaxation necessary for this alloy? The parameters of strain relaxation set up to the model seem to be related with a state of local deformation within grain. However, there is almost no information of local deformation about grain microstructure, because measurement of inhomogeneous deformation is difficult in actual grain microstructure. We can only measure deformation on the sample surface, even if we can. Disappointingly, most of the result of a measurement makes no sense, because stress condition is quite different between the surface of sample and the inside of sample.

Recently, three-dimensional strain mapping became possible by synchrotron radiation microtomography (SR-CT) [4]. The microtomography, which achieved 1 μm resolution by utilizing synchrotron radiation, is non-destructive inspection. Therefore, it is the only method for measuring time-dependent evolution of local strain in grain structure by tracking microstructural features that exist in sample like particles and pores step by step. This microstructural tracking technique based on microtomography has been utilized for studies of ductile fracture [5], crack propagation [6], and so on. In this study, inhomogeneous deformation in grain microstructure in aluminum alloy was investigated using this technique. Especially, the variation of deformation was measured for each grain. We investigated how much external deformation deformed grains heterogeneously.

Experimental procedure

Sample

A 2024 aluminum alloy heat-treated is used in this study. Large-size grains and spherical precipitates on grain boundaries are obtained by heat-treatment. The grain sizes are about 100-150 μm on rolling plane and about 30-80 μm on the cross section of roll normal direction. The precipitate size is approximately 3-8μm. Match-stick-like tensile specimens, whose size corresponds to field of view (ϕ948 μm × 626 μm) of microtomography, were cut from the sheet by electrical discharge machining. The cross section of specimens is 0.6 mm × 0.6 mm square and the gage length is 19 mm.

In-situ observation of tensile test by SR-CT

Synchrotron radiation experiment was carried out at beamline BL47XU in synchrotron radiation facility, SPring-8 in Japan. X-ray energy used in this study was 20 keV considering linear absorption coefficient in aluminum alloy. Compact material testing rig, which was designed for SPring-8 beamline and was driven by compression air, was installed in high-accuracy rotation stage. Prepared specimens were set up to the testing rig. The distance of 55 mm between sample and detector was used to enhance image by phase contrast. The detector system consists of a cooled CCD camera (Hamamatsu photonics, C4880-41S: focus = 105 mm, 4000 × 2624 pixels, 5.9 μm × 5.9 μm, 2 × 2 binning mode), an optics lens (× 20) and a scintillator ($Lu_2SiO_5:Ce^+$). The pixel size of detector system was $(0.5\ \mu m)^2$ from the combination of CCD camera and optics lens. The sample was scanned by taking 1500 radiographies from 0 to 180 degree with a 0.12 degree step.

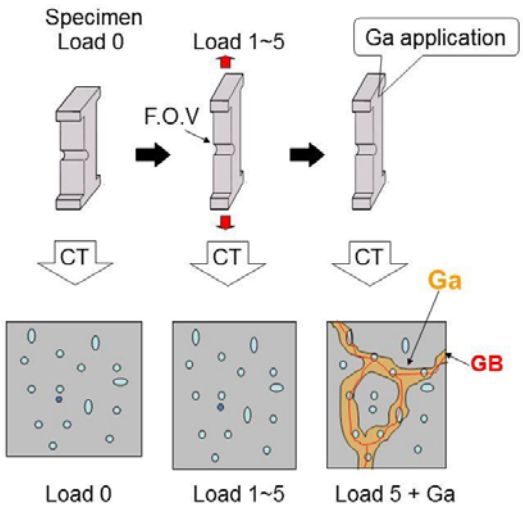

Fig. 1 Schematic illustration of experimental procedure

The scanning time was about 30 minutes. Schematic illustration of experimental procedure is shown in Fig. 1. First, tomography scan was performed at non-load situation (Load 0). Load was applied to the specimen step by step. The scan was conducted from Load 1 (29 N) to Load 5 (43 N). Before fracture occurs, we stopped increasing load. Liquid gallium, which penetrates aluminum grain boundary preferentially, was applied to the tensile deformed specimen. And then tomographic scan was performed again to visualize grain boundaries position.

3D extraction of grains

Three-dimensional images were reconstructed by convolution back projection method [7]. The voxel size of reconstructed volumetric image was $(0.5\ \mu m)^3$. Grains in three-dimension were extracted from CT image obtained after gallium application, which makes grain boundary position clear, by using 3D image processing as shown in Fig. 2. Registration was performed between CT images before and after gallium application. This process includes an image contraction of sample that was expanded by gallium penetration into grain boundaries. A part of gallium, which corresponds to grain boundary, was taken out from gallium-applied image by binarization. However, all grain boundaries cannot be detected by the binarization. Grain boundaries became disconnected. Sometimes, particles that have high linear absorption value as similar to gallium were also picked up. So, grains were detected by applying the image processing as follows. (1) Binarized objects that are a volume less than 1000 voxel were removed as a noise. (2) Gray level image that indicates distance from binarized object was produced by the distance transformation. (3) The local minimum was adjusted by the H-minima transformation. (4) Grain area was segmented by Watershed transformation. 74 grains were found in this study. Grain that was cut into pieces with (1)-(4) process was merged into one, and then volume and position of gravity center were re-calculated.

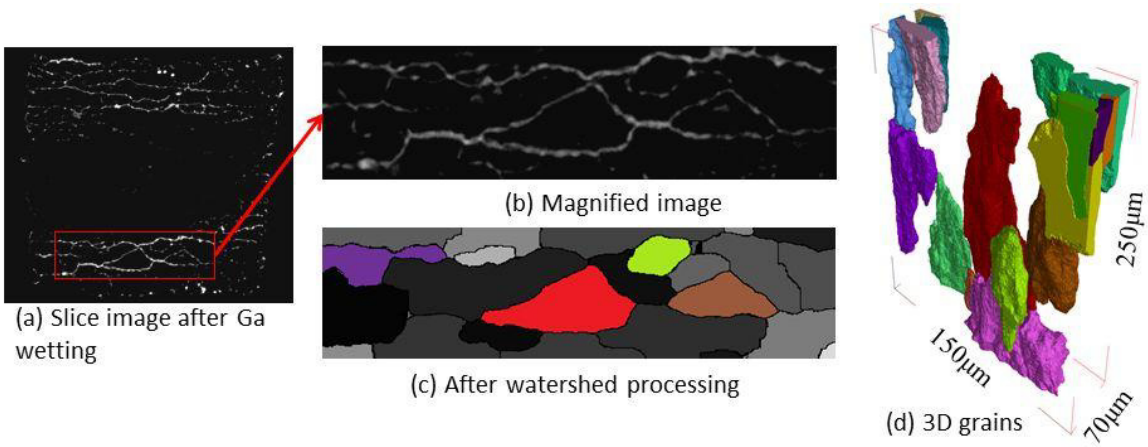

Fig. 2 Procedure of 3D grain extraction.

Measurement of plastic strain within grain

3D strain components of individual grains are estimated from displacement of particles that exist in the detected grain area. A grain contains the number of 10 - 100 particles. The displacement of these particles was measured by tracking them backward from load 5. The matching parameter method [8] was utilized for the particles tracking. The weight parameters for distance, volume and surface area were set up as $\alpha : \beta : \gamma = 0.8 : 0.1 : 0.1$. The grain was divided into many tetrahedrons whose vertex is gravity center position of particle, by utilizing 3D Delaunay tessellation algorithm. Strain of a tetrahedron was calculated from displacements of particles that

constitute the tetrahedron. The tensile strain in the whole sample was measured from the number of slices by counting 1 pixel as 0.5 μm.

Result and discussion

The global strain along the tensile direction in Load 1, 2, 3, 4 and 5 was 0.94 %, 1.89 %, 3.52 %, 5.32 % and 8.32%, respectively. Figure 3 shows maps of strain components in Load 5. Strain concentration and dispersion are seen in Fig. 3 due to polycrystal grain microstructures. Normal and shear strain distributions in the whole sample at 3.52 % (Load 3) is shown in Fig. 4.

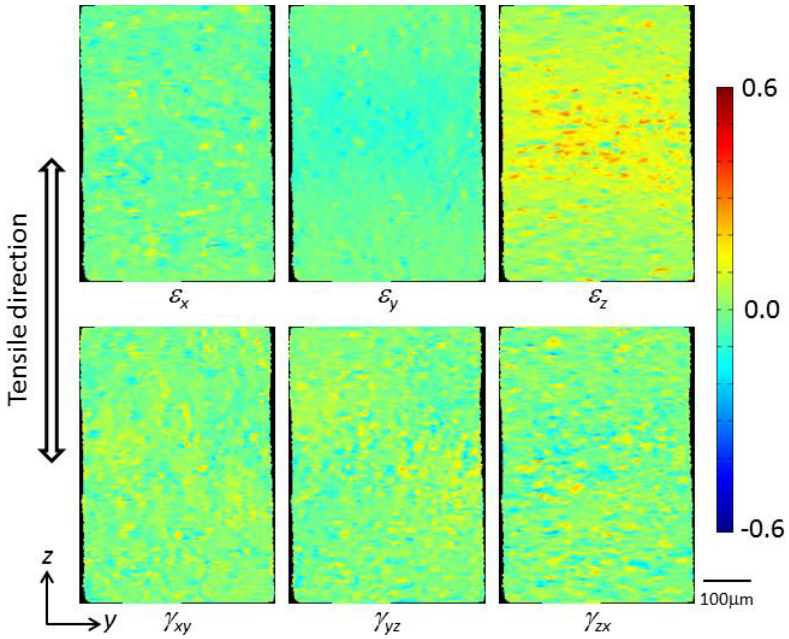

Fig. 3 Maps of strain components in Load 5, whose global tensile strain is 8.32%, on the y-z section at x = 300 μm

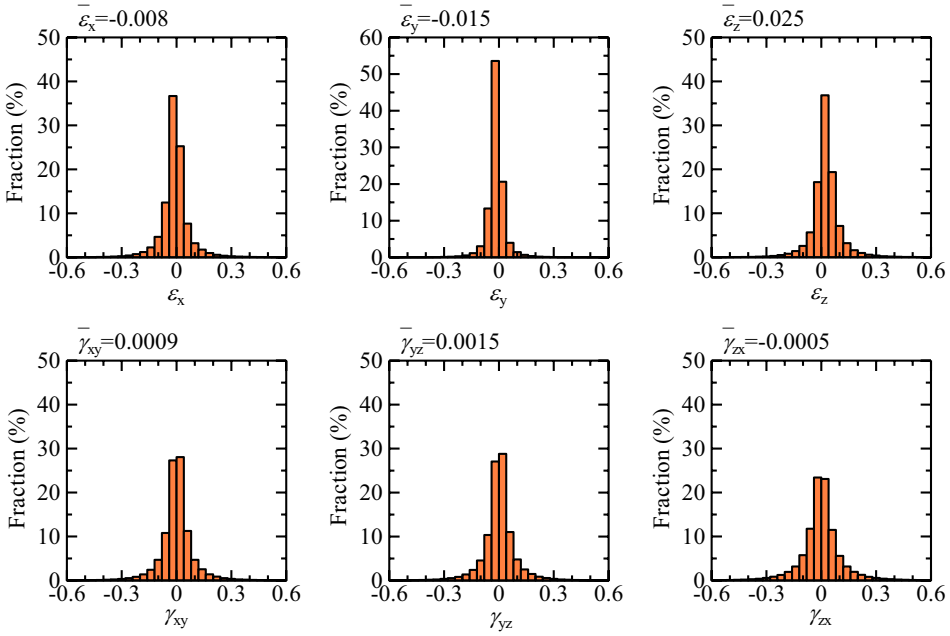

Fig. 4 Distribution of strain components in the whole of sample at Load 3, whose global tensile strain is 3.52 %

The distribution of ε_x, ε_y and ε_z shifted with increasing load step. The average strains of ε_z in the local strain measurement were 2.5 % and 6.0 % at Load 3 and Load 5, respectively. The average strains of ε_z roughly correspond to tensile strain, i.e. 3.25 % and 8.32%. The shape of strain distribution did not change, and the distribution of shear strain almost was constant without depending on load step. Although typical distribution of strain components within a grain obtained in this analysis seemed to be similar to that in Fig. 4, it was found that absolute values of average of shear components are relatively large and the distribution width is wide in γ_{xy} and γ_{yz}. It was considered that anisotropy of deformation caused by own orientation and restriction of deformation caused by the neighbor grain exist.

Table I. Strain components of neighboring grains at 8.32% global tensile strain (Load 5).

	ε_x	ε_y	ε_z	γ_{xy}	γ_{yz}	γ_{zx}
Average in all grains	-0.021	-0.036	0.059	0.001	0.004	-0.001
Grain A	-0.044	-0.063	0.117	0.022	0.019	-0.002
Grain B	-0.013	-0.061	0.082	-0.001	0.009	-0.028
Grain C	-0.012	-0.050	0.063	-0.033	0.007	-0.004
Grain D	-0.024	-0.075	0.060	-0.054	0.011	-0.002
Grain E	-0.010	-0.051	0.051	-0.056	-0.007	0.002
Grain F	-0.001	-0.093	0.014	-0.079	-0.034	0.020
Grain G	-0.021	-0.056	0.112	0.011	-0.017	0.012

Strain components in neighboring grains at 8.32% global tensile strain (Load 5) are listed in Table I. We can recognize local inhomogeneous deformation relative to the average value of strain components in all grains. As for ε_z strain, amount of deformation is different. Although grain A and grain G deformed, grain F deformed little. The direction of shear deformation seems to be different in individual grains. Therefore, the ratio of shear direction distinguished by plus and minus sign was investigated in individual grains. The ratios of shear deformation with plus sign were 41.9 %, 60.8 % and 47.3 % in γ_{xy}, γ_{yz} and γ_{zx}, respectively. As for the shear strain in γ_{zx}, the ratio of plus and minus sign was almost half. However, some deviation was observed in the shear γ_{xy} and γ_{yz}. In addition, relatively small scattering was confirmed in γ_{zx}. In contrast, a tendency of large scattering was observed in γ_{xy} and γ_{yz}. This seemed to be related with pan-cake like grain microstructure caused by a rolling in sample production process. The z-x plane corresponds to rolling plane. In addition, grain size in the z-x section is a little larger than that in other sections.

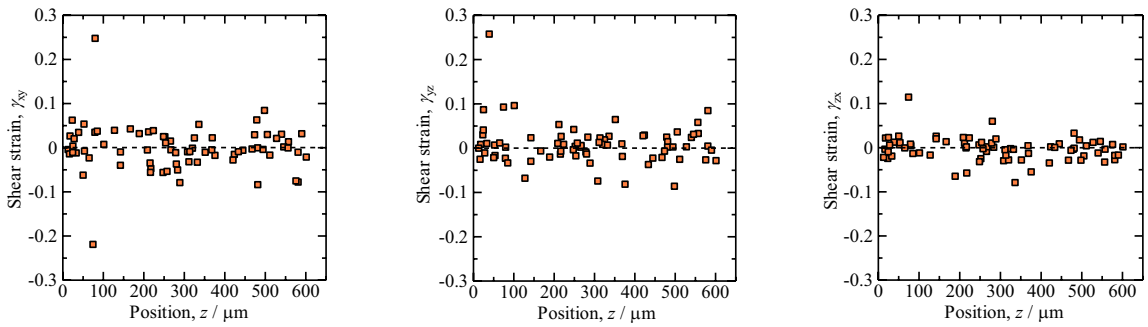

Fig. 5 Dependence of shear strain on z-position.

Scattering of shear strain in grain is shown in Fig. 5. The shear strains are plotted along the z-position. It is found that the scattering does not have any tendency depending on grain position.

It is suggested that shear deformation with the same direction doesn't occur among grains as if a group. The direction of shear deformation of a grain may be decided by neighbor grains so that shear strain is canceled among the grains. Moreover, no difference of shear direction was found in grain size on strain distribution.

Summary

Inhomogeneous deformation in grain microstructure of aluminum alloy was investigated using synchrotron radiation microtomography. The variations of deformation were measured for each grain. The shape of strain distributions didn't change in all strain components with increasing macroscopic tensile strain. Development of inhomogeneous deformation wasn't confirmed in the whole sample. With regard to individual grains, shear strains vary more widely than normal strains. Shear strain in individual grains was uneven and the shear direction was different. In the sample in this study, relatively small scattering was confirmed in γ_{zx}. In contrast, tendency of large scattering was observed in γ_{xy} and γ_{yz}. This reason may be grain microstructure caused by a rolling of sample production process. There was no tendency that neighbor grains deform to the same shear direction. Therefore, it is suggested that each grain deforms keeping boundary condition with neighbor grains and canceling shear-deformation.

References

1. G.I. Taylor, "Plastic Strain in Metals", *J. Inst. Metals*, 62 (1938) 307-324.

2. H. Honneff and H. Mecking, *Proc. 5th Int. Conf. in Texture of Materials*, ed. by G. Gottstein and K. Lücke, Springer-Verlag, Berlin, 1 (1978) 832-842.

3. J. Hamada, K. Agata and H. Inoue, "Estimation of Planar Anisotropy of the r-Value in Ferritic Stainless Steel Sheets", *Mater. Trans.*, 50 (2009), 752-758.

4. J. Baruchel, J.Y. Buffire, E. Maire, P. Merle, G. Peix (Eds.), *X-Ray Tomography in Material Science*, (Herms science publication, Paris 2000)

5. H. Toda, E. Maire, S. Yamauchi, H. Tsuruta, T. Hiramatsu, M. Kobayashi, "In situ observation of ductile fracture using X-ray tomography technique", *Acta Mater.* 59 (2011) 1995-2008.

6. H. Toda, I. Sinclair, J.-Y. Buffière, E. Maire, K.H. Khor, P. Gregson, T. Kobayashi, "A 3D measurement procedure for internal local crack driving forces via synchrotron X-ray microtomography", *Acta Mater.*, 52 (2004) 1305-1317.

7. G. T. Herman, *Fundamentals of Computerized Tomography: Image Reconstruction from Projection*, (Academic Press, New York, 1980)

8. M. Kobayashi, H. Toda, Y. Kawai, T. Ohgaki, K. Uesugi, D. S. Wilkinson, T. Kobayashi, Y. Aoki, M. Nakazawa, "High-density three-dimensional mapping of internal strain by tracking microstructural features", *Acta mater.* 56 (2008) 2167-2181.

2nd International Congress on 3D Materials Science
Edited by: Dominique Bernard, Jean-Yves Buffière, Tresa Pollock, Henning Friis Poulsen, Anthony Rollett, and Michael Uchic
TMS (The Minerals, Metals & Materials Society), 2014

INVESTIGATION OF PRE-EXISTING PORES IN CREEP LOADED 9Cr STEEL

Surya Deo Yadav[1], Joerdis Rosc[2], Bernhard Sartory[2], Roland Brunner[2], Bernhard Sonderegger[1,3], Christof Sommitsch[1], Cecilia Poletti[1]

[1]Institute for Materials Science and Welding, Graz University of Technology, Kopernikusgasse 24, A-8010 Graz, Austria
[2]Materials Center Leoben Forschung GmbH (MCL), Roseggerstraße 12, A-8700 Leoben, Austria
[3]Centre for Materials Engineering, Department of Mechanical Engineering, University of Cape Town, Cape Town, South Africa

Keywords: Cavity growth, P91, Martensitic steel, Computed tomography, Modelling

Abstract

Creep failure of materials under service conditions strongly rely on the formation and growth of cavities, encouraging the characterization and modelling of the cavitation process. In the present work pre-existing pores from manufacturing process are investigated in 9Cr steel creep loaded for up to 9000 hours. Scanning electron microscopy (SEM) is used for 2D analysis while Computer tomography (CT) is employed for 3D exploration. Nearest neighbours distances in 3D are calculated from 2D measurements and are decreasing with creep exposure time. The pore growth is studied applying a physical growth model, and experimental results are compared with numerical simulation. From this research it is deduced that damage occurs by agglomeration and growth of pre-existing cavities. The developed model can predict the growth of pores as a function of temperature and load at service.

Introduction

P91 belongs to the family of 9-12 wt-% Cr steels, widely used by the power plant industries to manufacture components such as boiler tubes, super heater tubes and turbine rotors. The microstructure of this 9 wt-% Cr steel consists of tempered martensite having $M_{23}C_6$ carbides distributed along prior austenitic grain boundaries, lath and packet boundaries. Furthermore MX type fine carbonitrides are dispersed throughout the matrix. When the material is exposed to high temperature loading, coarsening of precipitates, formation of new phases (Laves phase, Z-phase) and decrease of the dislocation density within laths due to recovery take place [1]. The precipitation of Laves phase drops the Mo content in the matrix, reducing solid solution strengthening. Precipitation of coarse Z-phase occurs at the expense of finely distributed MX type carbonitrides. Therefore, the density of restraining particles inside the matrix decreases [2]. The synergistic effect of these processes weakens the material and promotes cavitation/pore formation. The cavity nucleation, growth and interlinking are the leading failure mechanism in this material [3]. If macro cavities/pores exist in the material from the manufacturing process, they will be responsible for the final rupture [4]. These pre-existing macro cavities can grow either by diffusion, plasticity or by coupled diffusion and plasticity depending on temperature and applied stress [5].

The main objective of the present research is to characterize and model growth of pre-existing cavities/pores. Scanning electron microscope (SEM) and computed tomography (CT) are employed for characterization while standard stereological method is used for quantification.

Experiments and Methodology

Material and Creep Test

The chemical composition of P91 steel is given in Table 1. The material was supplied by RWE power AG in the form of a pipe with a wall thickness of 21 mm and a diameter of 250 mm. The creep samples were machined from the pipe with an aspect ratio of five. These specimens were creep loaded for 7000 hours and 9000 hours, at 650 ºC with an initial tensile stress of 60 MPa. The elongation was measured using the interrupted strain measurement technique. Mechanical polishing was employed up to 1 µm with silicon carbide polishing paper followed by vibrational polishing with neutral OPH solution for investigation.

Table 1 Chemical composition of used P91steel

Material	C	Si	Mn	P	S	Cr	Mo	Ni	Al	Nb	V	N	Fe
Wt-%	0.12	0.31	0.45	0.013	0.003	8.23	0.98	0.13	0.014	0.06	0.22	0.041	balance

Characterization

The pores produced from the manufacturing process having size larger than 1 µm were detected in as received condition by the means of SEM in BSE mode. SEM images using BSE detector were used for 2D measurements. The open source Image J software [6] was used to analyse the images in 2D and features like equivalent diameter, circularity and area were calculated.
X-ray computed tomography (CT) was used to get the 3D localization of the pores within the sample. A GE *nanotom m* was applied for the present investigation. The sample was positioned between an X-ray tube and an X-ray-sensitive flat panel detector to obtain CT scan. A number of radioscopic images were taken and three-dimensional volume was reconstructed by means of a mathematical algorithm [7]. Due to the high density of the P91, a smaller sample of about 560×340 µm was inspected with a resolution of about 2 µm. The quantitative analysis of defects within the sample was not possible due to artefacts within the CT data set which come from scattered radiation, which leads to highly blurred edges in the data [8].

Number Density and Nearest Neighbours Distance

A standard stereological method [4, 9] is used for estimation of number density and volume fraction, assuming that cavities are spherical. The number density in particular size class of cavity having diameter (D_i) is given as:

$$(N_v)_i = \left[(N_A)_i - \sum_{n=i+1}^{k} P_{i,n} D_n (N_v)_n \right] / \; P_i \cdot D_i \qquad (1)$$

Where i = 1, 2, 3…k and n ≤ k. In above equation $(N_A)_i$ is, number of sections of particular size per unit area from all possible sizes and P_i the probability that a random plane intersecting the cavity of diameter i produces a section diameter i. The details about the derivation can be found elsewhere [4]. The nearest neighbour distance is a key parameter for the modelling of pore

growth. In terms of number density, the nearest neighbour distance [10-11] of cavities (λ_{3d}) in 3D from the 2D measurements, is given as,

$$\lambda_{3d} = \sqrt[3]{3 \cdot \ln(2)/4\pi \cdot N_v} \tag{2}$$

Growth Modelling of Cavities

The present model was developed to describe the growth of pre-existing cavities, which can grow by addition of vacancies to their surface, under the influence of the local stress. The cavity growth rate is derived in terms of vacancies diffusion flux, which depends on the gradient of chemical potential [5, 12].

$$\frac{dr_{mean}}{dt} = \left(\frac{D_g \nabla\mu}{2kTr_{mean}}\right) \tag{3}$$

In above equation $D_g = D_0 \cdot exp(-Q/RT)$, is the grain boundary diffusion coefficient, $\nabla\mu$ the gradient of chemical potential, k the Boltzmann constant, Q the activation energy, R the gas constant and T is the temperature of loading. The chemical potential at grain boundaries is given by $\mu_{gb} = -\sigma_l\Omega$, while the chemical potential at a cavities surface is given as $\mu_{cavity} = -2\Omega\gamma/r_{mean}$, where σ_l is the local normal stress, Ω is the atomic volume, γ the cavity surface tension and r_{mean} is the mean radius of cavities [13]. The calculated chemical potentials in as received condition are 1.41×10^{-21} and 7.72×10^{-23} J/kg at the grain boundary and at the cavity surface, respectively. Thus cavities act like a sink for vacancies and grain boundaries as sources, triggering the growth of cavities. In the present model it was assumed that the vacancies which are produced in the regime where the local stress is about 10% percentage of the applied stress will diffuse to the cavity surface and contribute to growth (see fig. 1).

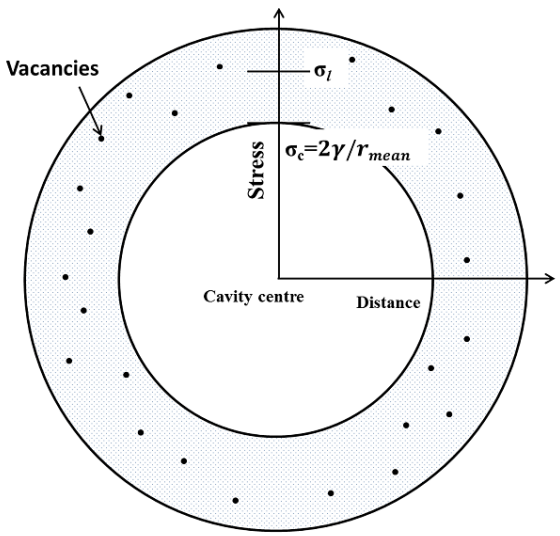

Figure 1. Surface tension at cavity surface and local stress away from cavity

The rest of the produced vacancies, other than in this region, have the tendency to agglomerate elsewhere and form a new cavity. The gradient of the chemical potential can be derived as:

$$\nabla\mu = \frac{\Omega}{\lambda_{3d}k_1}\left(\sigma_l - \frac{2\gamma}{r_{mean}}\right) \tag{4}$$

Here, λ_{3d} is the nearest neighbour distance calculated from equation (2) and k_1 is a constant. The numerical simulation was carried out by MatLab software package taking the mean radius of cavities as 1.28 μm in as received condition as input parameter. The activation energy was taken as Q = 290 kJ/mol and the following values have been chosen for the calculation: $\Omega = 2.35\times10^{-29}$ m^3 ; γ = 2.1 J/m^2 [14-15]. The simulation was performed for three different temperatures, including the experimental tested one.

Results and Discussion

Creep Data

The creep curves of specimens creep loaded for 7000 and 9000 hours with an initial tensile stress of 60 MPa at 650 ºC have shown [4] that the 9000 hours crept specimen has just started moving towards tertiary creep while the 7000 hours crept specimen still is in the secondary creep region. The specimens have shown, steady state creep rate of 8.3×10^{-10} s^{-1}.

Cavities

The pores are almost circular in shape and have a size range of 1 to 6 μm in the as received condition. The size was increased into the range of 2 to 11 μm, while the mean circularity was reduced from 0.86 in as received condition to 0.62 after 9000 hours of creep loading (see fig. 2).

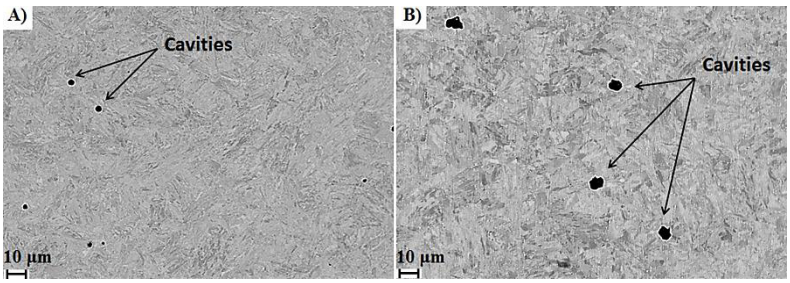

Figure 2. SEM micrograph (in BSE mode) of (a) as received material (b) specimen crept for 9000 hours

The number density of pores was estimated by a stereological method in as received and creep loaded condition. Although, it has been reported that stereological method overestimates the number density [4]. Before creep it was 4.95×10^4 mm^{-3}, while it decreased to 3.95×10^4 and 2.77×10^4 mm^{-3} for 7000 and 9000 hours creep exposed samples, respectively. The mean diameter was 2.56 μm in as received state, which was raised to 5.42 μm after 9000 hours of loading. The initial volume fraction was 0.11% which was upraised to 0.47% after 9000 hours of creep exposure. The increase in mean diameter and volume fraction while the lessening of number density with exposure time suggests growth and agglomeration of pre-existing pores.

The nearest neighbour distance was estimated from equation (2) assuming a random distribution without preferential nucleation sites. Investigation reveals that the distance is found 14.95 μm for as received material while increasing to 16.12 μm and 18.14 μm for 7000 and 9000 hours creep exposed samples, respectively. The nearest neighbour distance between pores is increasing with the creep loading time, which can be attributed to the agglomeration of the pores.

The CT measurement gives an overview of the 9000 hours creep loaded specimen (see fig. 3). The CT data set clearly showed a number of pores within the sample. The pores are represented as dark areas within the brighter volume. As can be estimated from the scale bar at the bottom of

the three slices, pores having size range of 6 to 10 μm could be visualized. Figure 3 shows three orthogonal slices and a 3D view of the sample. One specific pore is marked in the slice views as well as in the 3D views. The observation reveals the pores agglomeration which is in accordance with 2D measurements. The spatial distribution shows a heterogeneous spread of the pores throughout the reconstructed volume.

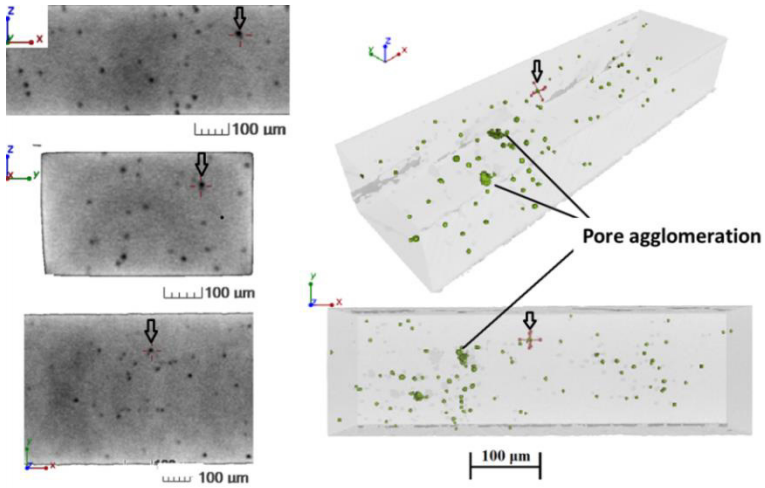

Figure 3. Three orthogonal slices and 3D reconstructed volume (850×789×2398 voxels) of 9000 hours crept specimen

Growth of Cavities

Figure 4 depicts the evolution of the mean radius of cavities with exposure time at three different temperatures. The numerical simulation was carried out assuming that the local stress is 10% of the applied stress. The model shows a good correlation with the experimental results at 650 ºC up to 7000 hours in the secondary creep stage while deviate at 9000 hours. The underestimation of the cavity mean size at 9000 hours is attributed to the macro volume interaction such as cavity agglomeration. After 9000 hours of loading the related specimen is in the tertiary creep stage and thus agglomeration of cavities take place.

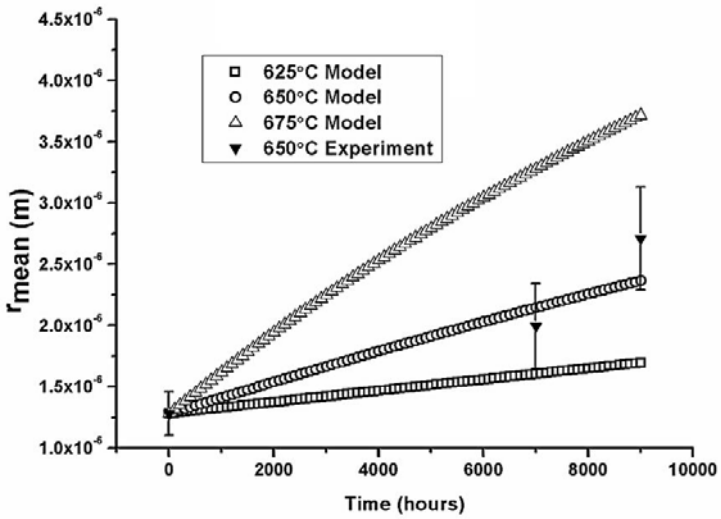

Figure 4. Growth of pre-existing cavities with loading time and temperature using a load of 60 MPa

Summary and Conclusions

This work characterizes the pre-existing pores in a P91 steel employing SEM and CT. The quantification was done using stereological methods. A cavities growth model was developed based on local stress levels. This research reveals that the pre-existing pores are growing followed by agglomeration with creep exposure time.

Acknowledgement

This research work was carried out under the project Hot Pipes number 826434, supported by the FFG -- Austrian Research Promotion Agency.

References

1. C. G. Panait, W. Bendick, A. Fuchsmann, A. F. Gourgues-Lorenzon and J. Besson, "Study of the microstructure of the Grade 91 steel after more than 100000 h of creep exposure at 600 ºC," *Int. J. of Press. Vessel. and Pip.,* 87 (2010), 326-335.
2. H. K. Danielsen and J. Hald "Behaviour of Z phase in 9-12%Cr steels," *Energy Mater.*, 1 (2006), 49-57.
3. H. T. Yao, F. Z. Xuan, Z. Wang and S. T. Tu, "A review of creep analysis and design under multi-axial stress states," *Nucl. Eng. and Des.*, 237 (2007), 1969-1986.
4. S. D. Yadav, B. Sonderegger, B. Sartory, C. Sommitsch and C. Poletti, "Characterization and quantification of cavities in 9Cr martensitic steel for power plants," *Mater. Sci. Technol.*, under review.
5. M. E. Kassner and T. A. Hayes, "Creep cavitation in metals," *Int. J. of Plast.*, 19 (2003), 1715-1748.
6. http://imagej.nih.gov/ij/download.html.
7. L. A. Feldkamp, L. C. Davis and J. W. Kress, "Practical cone-beam algorithm," *J. Opt. Soc. Am. A*, 1 (6) (1984), 612-619.
8. T. Buzug, Einführung in die Computertomographie, Springer-Verlag Berlin Heidelberg 2004.
9. E. E. Underwood, Quantitative Stereology, Addison Wesley Series In Metallurgy And Materials, (1970).
10. B. Sonderegger and E. Kozeschnik, "Particle strengthening in fcc crystals with prolate and oblate precipitates," *Scripta Mater.*, 66 (2012), 52-55.
11. S. Chandrasekhar, "Stochastic problems in physics and chemistry," *Rev. Mod. Phys.*, 15 (1943), 1-89.
12. W. Beere and M. V. Speight, "Creep cavitation by vacancy diffusion in plastically deforming solid," *Metal Science*, April (1978), 172-176.
13. D. Hull and D. E. Rimmer, "The growth of grain-boundary voids under stress," *Philos. Mag.*, 4 (1959), 673-687.
14. H. Magnusson and R. Sandström, "Creep strain modeling of 9 to 12 Pct Cr steels based on microstructure evolution," *Metall. Mater. Trans. A*, 38A (2007), 2033-2039.
15. P. Shewmon and P. Anderson, "Void nucleation and cracking at grain boundaries," *Acta Mater.*, 46 (1998), 4861-4872.

2nd International Congress on 3D Materials Science
Edited by: Dominique Bernard, Jean-Yves Buffière, Tresa Pollock, Henning Friis Poulsen, Anthony Rollett, and Michael Uchic
TMS (The Minerals, Metals & Materials Society), 2014

APPLICATION OF DIFFRACTION-AMALGAMATED GRAIN BOUNDARY TRACKING (DAGT) TO FATIGUE CRACK PROPAGATION BEHAVIOR IN HIGH STRENGTH ALUMINUM ALLOY

Hui Li[1], Hiroyoki Toda[2], Kentaro Uesugi[3], Akihisa Takeuchi[3],
Yoshio Suzuki[3], Masakazu Kobayashi[1]

[1]Toyoshashi University of Technology;
1-1 Hibarigaoka, Tempaku-cho; Toyohashi, Aichi 441-8580, Japan
[2]Kyushu University;
744 Motooka; Nishi-ku, Fukuoka 819-0395, Japan
[3]Japan Synchrotron Radiation Research Institute (JASRI);
1-1-1 Kouto, Sayo-cho; Sayo-gun, Hyogo, 679-5198, Japan

Keywords: Fatigue, Synchrotron Radiation, Crack propagation behavior, Grain orientation

Abstract

The fatigue crack propagation behavior in an Al-Zn-Mg-Cu alloy was investigated by amalgamating X-ray diffraction (XRD) with grain boundary tracking (GBT). The integrated technique, Diffraction-Amalgamated Grain Boundary Tracking (DAGT), provides new possibilities for mapping grain morphologies and crystallographic orientations in three-dimension (3D). 3D crack morphologies at different propagation stages in the bulk of metallic materials were successfully obtained by using Synchrotron Radiation X-ray Microtomography (SRCT). Using 2D slices of the 3D crack, the crack length increment was measured to calculate the crack growth rate which varies significantly. Typical crack morphology, such as crack tilt, is detected by the observation of 2D tomographic slice image. The observed interaction between fatigue crack and polycrystalline microstructures can be analyzed in 3D. Through this synthesis of techniques, DAGT, a detailed direct assessment of microstructure and crack propagation behaviors has been achieved.

Introduction

Fatigue crack propagation behavior within polycrystalline materials has been investigated for several years. It has well been documented that the crystallographic microstructure could be one of the key factors that control the fatigue crack propagation process. Zhai et al. [1] studied the effects of grain orientation on the crack propagation behavior of short fatigue cracks in high strength Al-Li 8090 and AA 2026 aluminum alloys. The results showed that the twist and tilt angles of the crack plane deflected by a grain boundary are the key factors controlling transgranular crack growth.

High resolution Synchrotron Radiation X-ray microtomography (SRCT) technique has been utilized for in situ visualization of 3D fatigue crack propagation behavior in the bulk of metallic materials. Three-dimensional X-ray diffraction (3DXRD) microscopy is a new experimental method which provides the possibility of non-destructive 3D crystallographic analysis. For example, Nielsen et al. [2] utilized the 3DXRD microscope for the study of the rotation history of individual grains during the tensile straining.

In this study, a novel method has been utilized to obtain the accurate information about grain morphologies to 1 micron level and individual grain orientation from near field XRD analysis by amalgamating the X-ray diffraction (XRD) microscopy with grain boundary tracking (GBT) [3]. The crystallographic orientation of individual grains is determined directly from the position of the diffraction spots recorded on the detector, using the information from all the rotation angle ω settings. Hereby, the measurements by DAGT [4] of the grains surrounding a fatigue crack allow us to discuss and interpret the fatigue crack propagation behaviors.

Experiment

Material and specimen preparation

The material used in this work was a 7075 aluminum alloy which is used as an aerospace material. It is an Al-Zn-Mg-Cu alloy and its chemical composition is given in Table I. Hot rolled plate of Al alloy was solution heat-treated at 773K for 36 ks followed by cold water quenching and artificial aging under the T7 condition at 453 K for 108 ks. A three-point bending (TPB) specimen was machined obliquely at about 45° along the rolling direction from the plate. A notch with a radius of 0.45 mm was introduced by electrodischarge machining to allow easy precracking. After that, a small match-like parallelepiped specimen (square cross-section of 0.6 × 0.6 mm^2) containing a fatigue crack tip was carefully machined from the TPB specimen by electrodischarge machining, and Al tabs were glued to the two ends of the small specimen for the subsequent in situ loading of the specimen into the testing machine [5].

Table I. Chemical compositions of 7075 Al alloy (mass %)

Si	Fe	Cu	Mn	Mg	Cr	Zn	Ti	Zr + Ti	Al
< 0.40	< 0.50	1.6	< 0.30	2.5	0.23	5.6	< 0.20	<0.25	Bal.

Grain orientation measured by Pencil-beam XRD

A pencil beam X-ray diffraction experiment was performed using the X-ray imaging beamline, BL20XU, of the synchrotron radiation facility, SPring-8, in Hyogo, Japan. A 10 × 10 μm^2 pencil beam was obtained with a photon energy of 35 keV from a Si double crystal, which was scanned across the specimen at intervals of 10 μm across the horizontal direction at 70 different points, and down the axial direction at intervals of 10 μm at 21 points. The specimen was rotated through 180° at each point with an exposure time of 100 ms per degree. A Powder P43 (Gd_2O_2Si:Tb) scintillator was used in combination with a 2048 × 2048 element CMOS camera to collect the data with a pixel size of 5 μm.

In situ X-ray microtomography and fatigue testing

A highly coherent monochromatic X-ray beam, with an energy of 20 keV, was obtained from a Si double crystal. A Ce-doped scintillator was used in combination with a 4000 × 2624 element charge-coupled device (CCD) camera to capture the visible light while the rotation stage is rotated over 180°. The specimen-to-detector distance was set at 60 mm in the in situ test. The fatigue test was carried out with a stress ratio R of 0.1. During fatigue cycling, the maximum and minimum loads were 50 N and 5 N, respectively. Once a crack extension was detected, the

fatigue cycling was stopped at 2,000 and 3,000 cycles and a tomographic scan was performed. A total of 1,500 radiographs were obtained for each tomographic scan while the specimen was rotated 180° along the specimen axis. The isotropic voxels in the reconstructed image were (0.497 μm) ^{3} in size. After the fatigue testing, the gallium wetting procedure was adopted for the visualization of the grain boundaries [6].

Crystal orientation analysis by DAGT

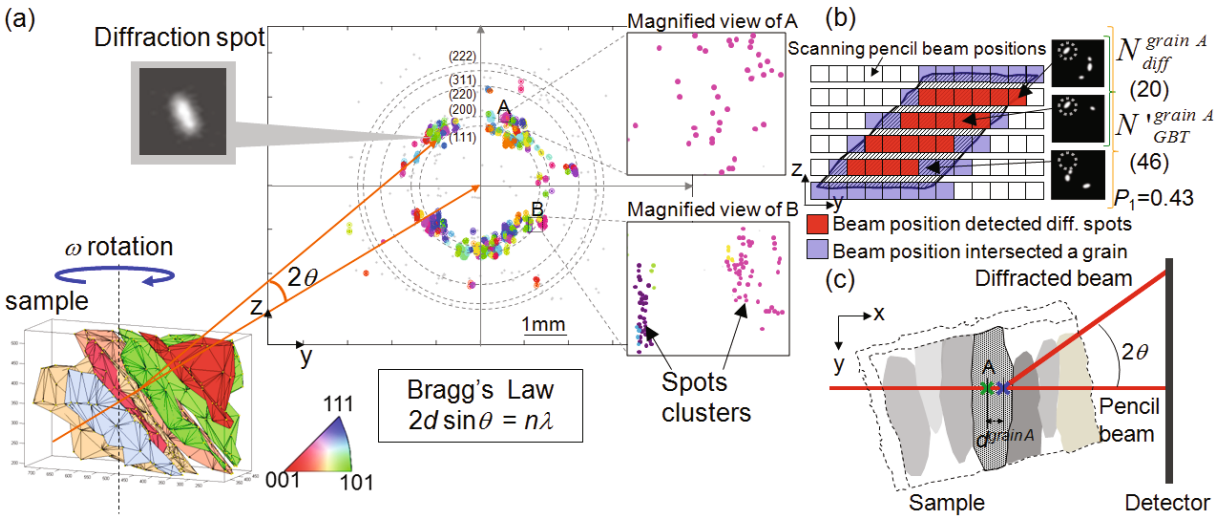

Figure 1. Schematic illustration of diffraction spots cluster found by clustering algorithm at a specific ω angle. (b) Schematic diagram depicting the cross-section of a grain with positions of scanning pencil beam and points of intersection. (c) P_2 is based on the distance between where a diffraction spot originated (✕) and mid-point of the grain/beam interaction (✕).

The groups of diffraction spots were arranged by the rotation angle ω, as shown in Figure 1a. When the beam intersected the grain, the first probability (P_1) was calculated by the relationship between the total number of times the beam intersected the grain and the groups of diffraction spots. The second probability (P_2) was based on the difference between the center of mass (CCM) of the beam interacting with the grain and the calculated origin of the diffracted beam. Both P_1 and P_2 had been calculated, as shown in equation (1) and (2). The schematic diagram of P_1 and P_2 is shown in Figure 1b-c. P_1 and P_2 are then combined to generate P_{final} (equation 3).

$$P_1 = (N_{\text{diff}}) / (N_{\text{GBT}}) \quad (1)$$

$$P_2 = e^{-d} \quad (2)$$

$$P_{\text{final}} = (\omega_1 \times P_1 + \omega_2 \times P_2) \quad (3)$$

where ω_1 and ω_2 were weighting values determined according to the relative accuracy of each previously determined probabilities. If P_{final} is below a pre-determined threshold value, it is rejected for that grain. Crystallographic orientations were then systematically calculated by pairing up each of the retained diffraction spots. The orientation for each pair diffraction spots was derived from the scattering vectors of each diffraction spot.

Results and Discussion

Crystal orientations determined by DAGT

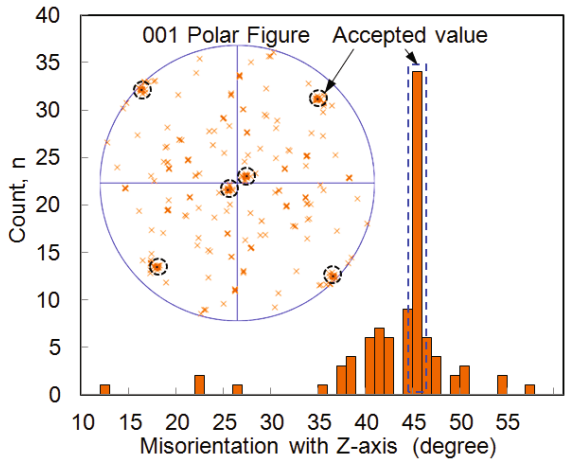

Figure 2. Polar figure depicting relative orientations and the resulting histogram.

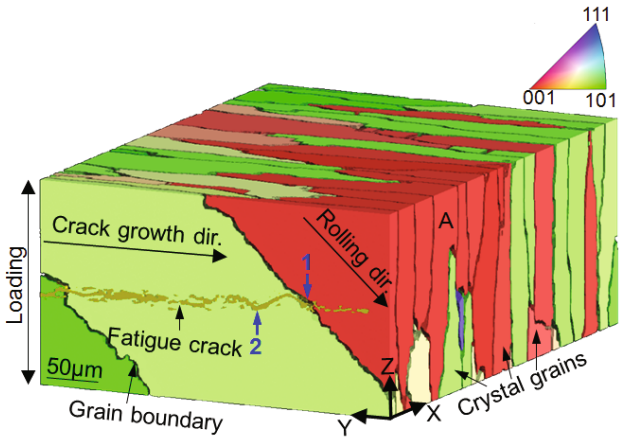

Figure 3. 3D rendering of the grains intersecting the fatigue crack.

Figure 2 shows all of the crystal orientations which are calculated by the groups of diffraction spots assigned to the crystal grain A labeled in Figure 3 and plotted on a histogram. 34 pairs of points, their misorientations with Z-axis within 1° tend to integrate into one point. Groups of diffraction spots from the adjacent grains will also be included. The orientation related to the highest frequency density was assigned to the grain related to the previously retained diffraction spots. Figure 3 shows that the crack path on planes clipped within the volume as they would appear on observations made by the section of the sample. In some cases strong deflection of the crack is clearly correlated with the presence of grain boundary with the large misorientation of 59.07° (e.g. arrow 1), but the deflection can also be observed within a grain (e.g. arrow 2).

Observation of the crack in 2D

Figure 4 shows a 2D tomographic slice image of the reconstructed volume for a sample after 3,000 cycles showing the fatigue crack, intermetallic particles and micropores. It corresponds to slice number 378 labeled by a black line in Figure 5c. The complex crack morphology can be seen at the centre of the image, with relatively spherical micropores (black) and complex intermetallic particle groups (white) in the surrounding matrix. The crack was segmented by a simple grayscale threshold. Manual separation of some connected objects was necessary. The stack of 2D images was segmented to reconstruct a 3D rendering of the fatigue crack as a function of the number of cycles. The extracted cracks were projected onto a plane perpendicular to the loading axis for different stages of fatigue, as shown in Figure 5. Areas where the background color can be seen (white) indicate the existence of crack closure, or ligaments in the crack wake, or a crack opening too small to be detected.

To provide quantitative information on crack growth, the apparent crack length increment as a function of loading cycles was measured by using 2D slices of the 3D crack. This was divided by the number of cycles to obtain the crack growth rate, da/dN, as shown in Figure 6. Since a projection of the crack (Figure 5) is used, some effects of crack deflection on crack growth rate

are not included in the calculation. Note that the crack growth rate varies significantly and appears to be inhomogeneous. At the initial step, crack propagation is relatively fast. In the final 1,000 cycles, the crack growth rate decreases.

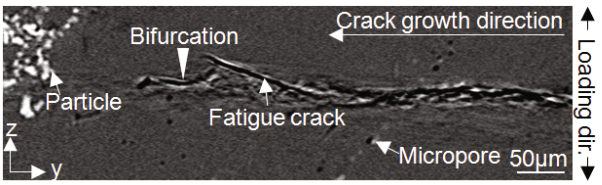

Figure 4. Reconstructed slice image showing typical fatigue crack and microstructure.

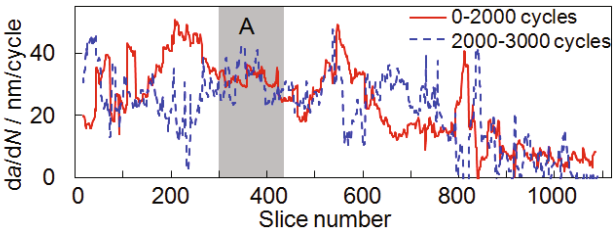

Figure 6. Variations of the crack growth rate at different fatigue cycles.

Observation of the crack front profile revealed several features of crack propagation. It is noted from the second fatigue stage (Figure 5b) that the crack propagation is retarded by fatigue cycling, which corresponds to slice number in the range 300-430, as indicated by region A. The crack growth rate of region A is relatively slow at the first step as shown in Figure 6.

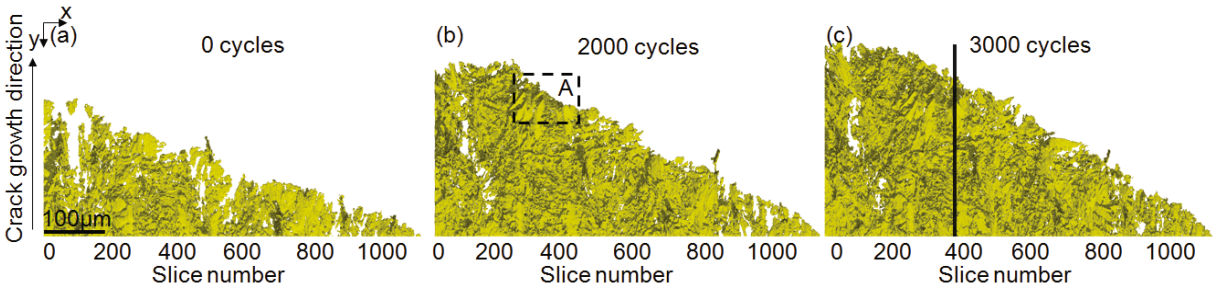

Figure 5. Projection of fatigue crack volume on a plane (X-Y) perpendicular to the loading axis. The crack front profiles at different stages of fatigue cycling from 0 cycles (a) to 3000 cycles (c) are highlighted.

Observation of the crack in the bulk of the sample

The crack path in the interior of the sample is more complex than the relatively linear propagation observed on the 2D slice image. A better understanding of the crack morphology can be obtained when looking directly at a 3D representation of the crack surface. Figure 7a shows a 3D rendering of the crack in the 3,000-cycle sample, highlighting the crack geometry and the crack front profile. A typical crack tilting region was labeled A, magnified in Figure 7b. In the central part of the crack front, one can also distinguish the bifurcation shown previously in Figure 4. The abrupt change in inclination of the central crack segment suggests that the crack front in the crack propagation direction propagates from one grain (G1) into a new grain (G2) with the large misorientation of 59.07° between these adjacent grains and the crack path changes as a consequence. In order to check this assumption, the information of the 3D shape of the grains along the crack path could be used, as shown in Figure 7c. The analysis of the strongly inclined central segment with respect to the surrounding grain structure clearly revealed that the deflection of the crack is related to a new grain on the crack front.

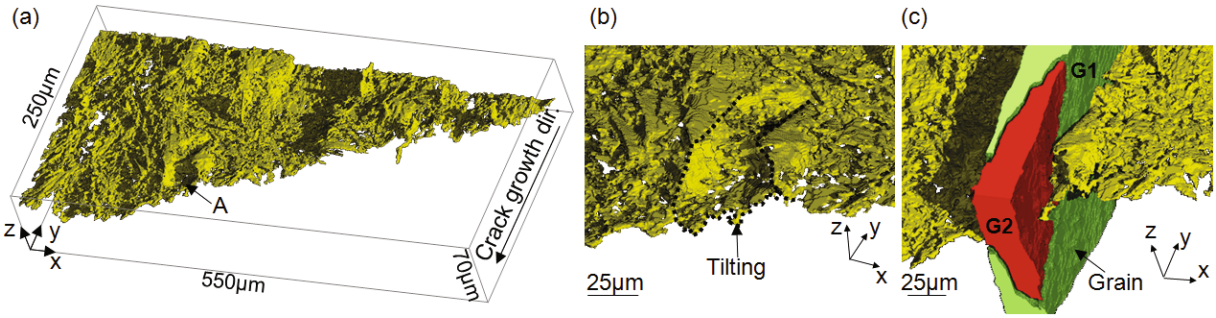

Figure 7. Three-dimensional rendering of the crack volume extracted from the 3000-cycle sample. The crack abrupt tilting is labeled A. (b-c) Magnified views of crack tilt region A in (a) and the grain that caused the sudden deviation.

Conclusion

A novel method that can provide crystallographic analysis of polycrystalline materials has recently been utilized by combining GBT with XRD. This combination of techniques, Diffraction-Amalgamated Grain-Boundary Tracking (DAGT), provides individual grain orientations from XRD analysis, whilst GBT accesses 1 μm level analysis of grain morphologies in 3D. The three-dimensional analysis of the crack with respect to the grain structure indicates that the growth of the crack into a new grain occurs preferentially from regions on the grain boundary, where the growth can be accommodated by tilting of the crack plane.

Acknowledgement

The synchrotron radiation experiment was performed at SPring-8 with the approval of JASRI through proposal number: 2011B1116. This work was undertaken with the support of a Grant-in-Aid for Scientific Research (A) from JSPS, through Subject No. 20760466.

References

1. T. Zhai, A.J. Wilkinson and J.W. Martin, "A Crystallographic Mechanism for Fatigue Crack Propagation through Grain Boundaries", *Acta Materialia*, 48 (2000), 4917-4927.
2. S.F. Nielsen et al., "A Three-Dimensional X-ray Diffraction Microscope for Deformation Studies of Polycrystals", *Materials Science and Engineering*, A 319-321 (2001), 179-181.
3. H. Toda et al., "Grain Boundary Tracking: A Four-Dimensional Visualization Technique for Determining Grain Boundary Geometry via Local Strain Mapping", *Acta Materialia*, 61 (2013), 5535-5548.
4. D.J. LeClere et al., "Diffraction-Amalgamated Grain-boundary Tracking (DAGT) Technique and its Application to An Aluminum Alloy" (Papers presented at the 13_{th} International Conference on Aluminum Alloys (ICAA13), Pittsburgh, Pennsylvania, 3 June 2012), 9-14.
5. H. Toda et al., "Direct Measurement Procedure for Three-Dimensional Local Crack Driving Force Using Synchrotron X-ray Microtomography", *Acta Materialia*, 56 (2008), 6027-6039.
6. M. Kobayashi et al., "Preferential Penetration Path of Gallium into Grain Boundary in Practical Aluminum Alloy", *Philosophical Magazine*, 86 (2006), 4351-4366.

2nd International Congress on 3D Materials Science
Edited by: Dominique Bernard, Jean-Yves Buffière, Tresa Pollock, Henning Friis Poulsen, Anthony Rollett, and Michael Uchic
TMS (The Minerals, Metals & Materials Society), 2014

INFLUENCE OF THE LOST FOAM CASTING MICROSTRUCTURE ON LOW CYCLE FATIGUE DAMAGE OF A319 ALUMINUM ALLOY

Nora Dahdah[1], Nathalie Limodin[1], Ahmed El Bartali[1], Jean-François Witz[1], Rian Seghir[1], Long Wang[1], Eric Charkaluk[1], Jean-Yves Buffiere[2]

[1]Laboratoire de Mécanique de Lille (LML), CNRS UMR 8107; Cité Scientifique; Villeneuve d'Ascq, 59650, France
[2]Laboratoire Matériaux, Ingénierie et Sciences (MATEIS), INSA-Lyon, CNRS UMR 5510; 20; Villeurbanne, Rhône, 69621, France

Keywords: Aluminum-silicon alloys, Digital Volume Correlation, synchrotron X-ray tomography

Abstract

In cast aluminum alloys used in the automotive industry the microstructure inherited from the foundry process has a strong influence upon the fatigue behavior. In the cylinder heads produced by the Lost Foam Casting process, the microstructure consists of hard intermetallic phases and large gas and microshrinkage pores. In order to study the influence of this complex 3D microstructure on fatigue crack initiation and propagation, an experimental protocol using laboratory and synchrotron tomography, Finite Element simulation and 3D Digital Volume Correlation has been used. Full field measurements at the microstructure scale were performed during a low cycle fatigue test at room temperature performed in situ under synchrotron X-ray tomography (TOMCAT beamline, SLS). Synchrotron tomography allowed characterizing the eutectic Al–Al_2Cu, iron based intermetallics phases and above all eutectic Si, which could not be distinguished with laboratory tomography; these constituents were proved a suitable natural speckle for Digital Volume Correlation.
The 3D cracks were observed to initiate at large pores and then to propagate along the hard inclusions towards the free surface. The DVC of in-situ fatigue tests allows observing the relations between cracks and displacements discontinuities and strain localizations in measured field. The experimental protocol proposed will be further improved for a validation at a temperature characteristic of in-service conditions of cylinder heads (250°C).

1. Introduction

In the automotive industry, economical constraints together with environmental requirements have led into process modification of some engine parts like cylinder heads. Nowadays, the Lost Foam Casting process (LFC) replaces the conventional Die Casting (DC) process due to cost reduction and geometry optimization goals. Even if this process seems promising, there are some drawbacks such as a coarsening of the microstructure, which consists in hard second phase particles (eutectic Si, eutectic Al–Al_2Cu, and iron based intermetallics), large pores and microshrinkage cavities. Above a critical size, pores [1] play a decisive role by providing preferential crack initiation sites. However, an influence of oxides [2], iron-based intermetallics [3] and Si particles [4] are also observed. The cracks could initiate at any large defects present in bulk. In order to study the

influence of this casting microstructure upon the fatigue behavior of the A319 Al–Si–Cu alloy, an experimental protocol using synchrotron tomography and 3D digital volume correlation has been set up.

2. Experimental procedure

The material studied was an A319 aluminum silicon alloy (Al bal.– Si 7.18 wt.% – Mg 0.32 wt.% – Mn 0.15 wt.% – Cu 3.17 wt.% –Fe 0.43 wt.% – Ti 0.05 wt.%). Specimens with a 2.6x2.6mm^2 cross section were cut out from a cylinder head in the fire deck area by electro discharge machining. X-ray microtomography was realized prior to the low cycle fatigue test to screen ten specimens not presenting large defects away from the specimen's shoulders and with a maximum size of defects compatible with the specimen cross-section. Laboratory X-ray microtomography was performed at the MATEIS laboratory (Lyon, France) in fast scan mode with a 80 kV acceleration voltage to ensure a 10% transmission of the X-ray beam through the cross-section of the sample. The scan was made at a medium resolution with a voxel size of 5µm and an acquisition time per image of 500 ms; this medium resolution images allow revealing the size and shape of the large pores in the bulk of the specimens gauge length rapidly.

The aim was first to obtain 3D characterization of pores in the ten selected samples which were then mechanically polished on all faces using SiC paper and diamond suspension. The matrix, i.e. the material without the pores, of these specimens was segmented from the 3D image obtained from X-ray tomography and a geometric model with a volumetric tetrahedral grid was created using Avizo software. The model was used for elastic finite element simulation using Abaqus software in order to predict the most strained region under tensile loading and to focus the subsequent in-situ observation by high resolution X-ray tomography on this small volume.

The low cycle fatigue tests were realized at room temperature and monitored by synchrotron X-ray tomography on TOMCAT beamline at the Swiss Light Source. The coherence of the synchrotron monochromatic X-ray beam (25keV) allowed performing absorption contrast tomography in edge enhancement mode with a voxel size of 1.625 µm. 1500 radiographs were taken while the specimen was rotating over 180° along its vertical axis. With an exposure time of 300 ms per image, one scan lasted about 7 min. A specially designed fatigue machine was used to load the specimen in situ. The fatigue test ($R \approx 0.1$, $\sigma max \approx 151$MPa) was performed step by step, only a few cycles were launched between each step. The test was conducted until crack initiation or failure with periodic interruptions to acquire tomographic scans under minimum and maximum load of the considered cycle in order to detect and follow fatigue crack initiation and growth. All the 3D images were reconstructed by using the reconstruction platform [5] developed by SLS. Then, they were binned to reduce the amount of data and the time needed to process them; this results in an effective voxel size of 3.25µm.

Synchrotron tomography allowed to visualize the eutectic Al–Al_2Cu, iron based intermetallics phases and above all eutectic Si, which could not be distinguished with laboratory tomography; these constituents were proved a suitable natural speckle for Digital Volume Correlation. The 3D displacement field was measured with the Digital Volume Correlation (DVC) technique [6], which is an extension of the well-developed Digital Image Correlation (DIC) method. In the present study, a 2D/3D image correlation platform newly developed at LML laboratory (Lille, France) has been

used. This correlation platform is based on C++ and it has been optimized to process large 3D volumes in a limited time. For a 780x725x1080 voxels image the calculation lasts about 40min with an isotropic element of 16 voxel edge on a 32Go RAM laptop. The correlation calculation is a sequence of optical flow integrated and finite element methods using regularization with a median filter [7] to compensate for poor microstructural textures avoiding thus the extremes values.

3. Results and discussion

The analysed specimen, as well as all the ten selected samples contains rather large number of pores in the gauge length volume (Figure 1(a)).

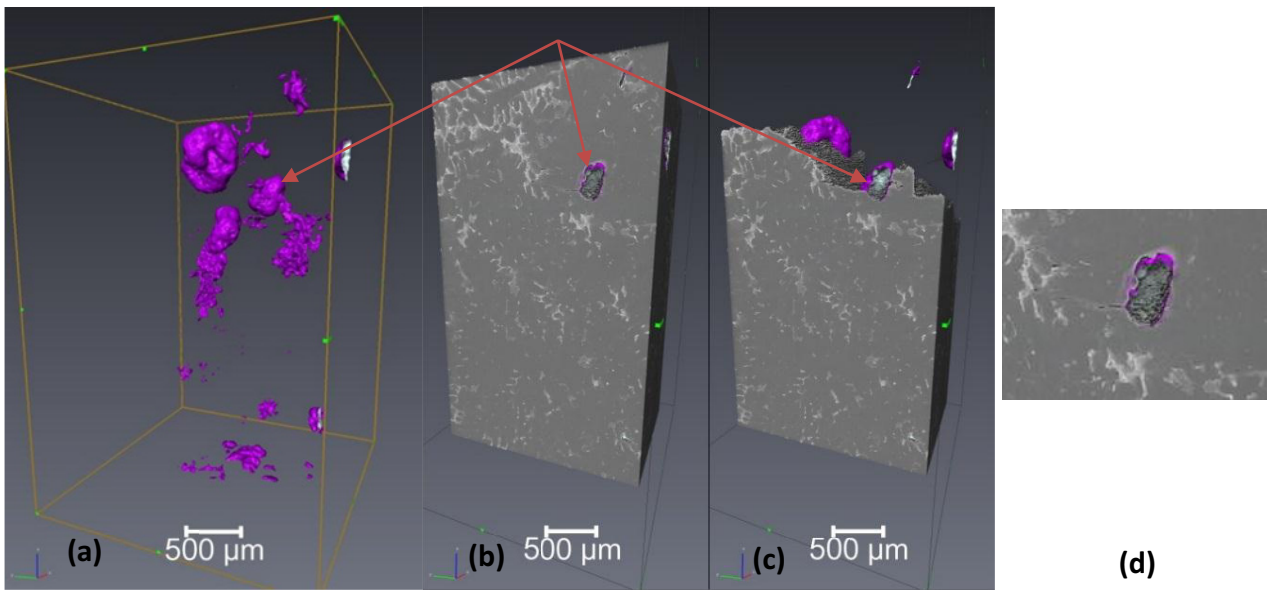

Figure 1. (a) Rendering of pores in the fatigue test specimen, (b) Specimen microstructure before failure (c) Specimen microstructure after failure (d) crack zone

The distribution of Feret diameter of these pores shows a peak around 70µm with a maximum Feret diameter of 940µm. Although scarce in number, the largest pores represent most of the pores volume fraction; this implies that large pores may have a significant influence on fatigue behaviour.

The displacement and strain fields were computed by DVC zone of the sample (779x724x1030 voxels^3) containing the largest pores fraction (upper of the block shown in Figure 1(a). The pore shown with the arrows in Figure 1(b) has led to progressive crack growth (Figure 1(d)) until final failure (Figure 1(c)).

Figure 2 and 3 show the displacement and corresponding strain field along the loading direction; the image of the microstructure was superposed to these fields to allow comparison of the crack path with local deformation.
The fields were studied at different steps of the fatigue cycles. The figures 2 and 3(a) show respectively displacement and strain fields between 300 cycles and 500 cycles (300c-500c), the crack initiation was detected at 500 cycles and sample broke after 2500 cycles; the figures 2 and 3 (b) show fields between 500c and 1000c where the propagation of the crack is observed, the figures

2 and 3 (c) are the last steps before the failure between 1000c and 2500c where crack growth is the most important. The figures 2 and 3 (d) allowed a better visualization of the microstructure in the crack neighbourhood. A good correlation is observed between the crack location, the displacement discontinuities and the strain localizations.

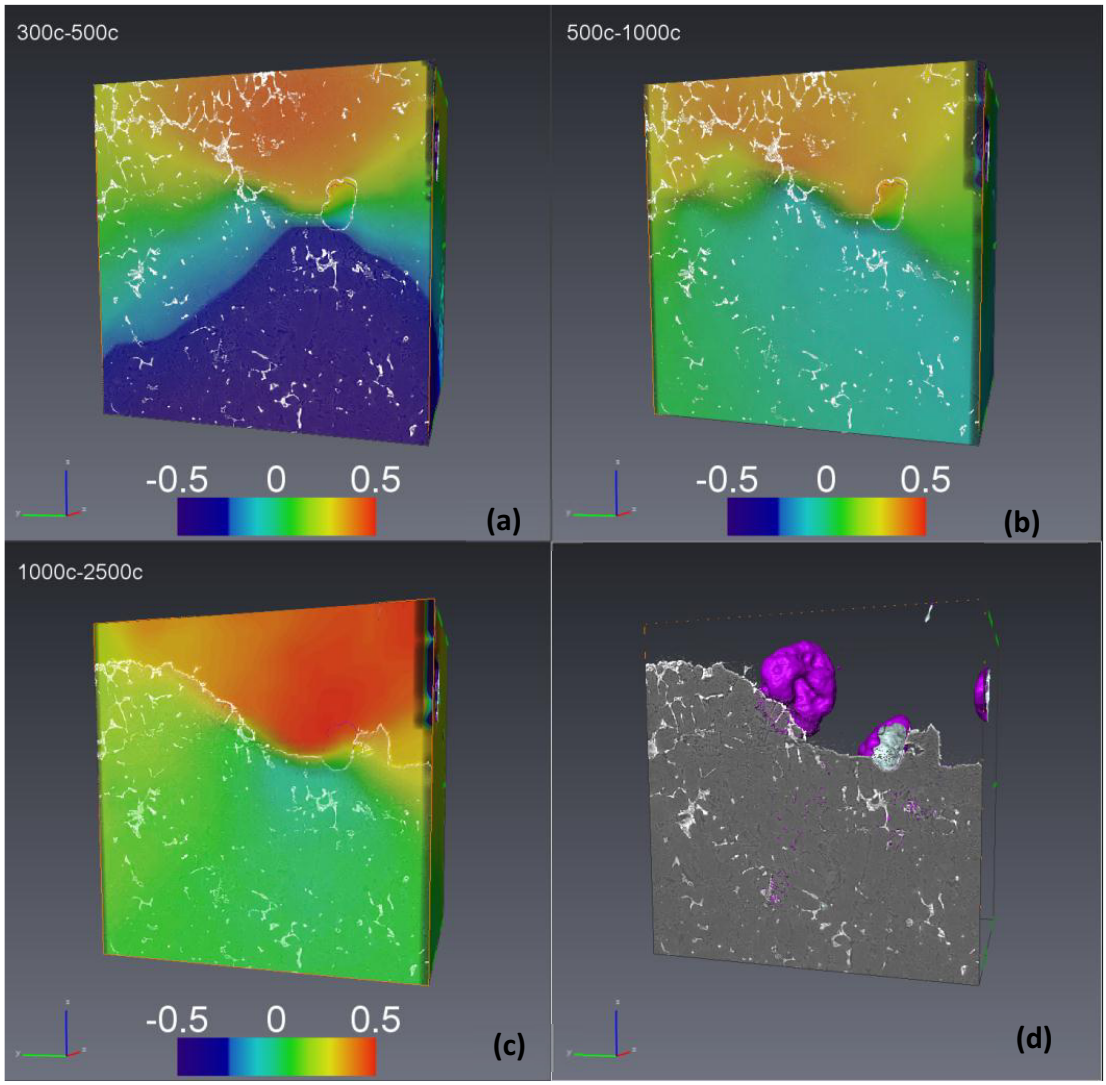

Figure 2. 3D displacement field (in voxels) along z with the microstructure shown in transparency between (a) 300c-500c, (b) 500c-1000c, (c) 1000c-2500c and (d) the fracture surface

The results show that the 3D crack initiated first at large subsurface pores and then propagated along the hard inclusions towards the free surface.

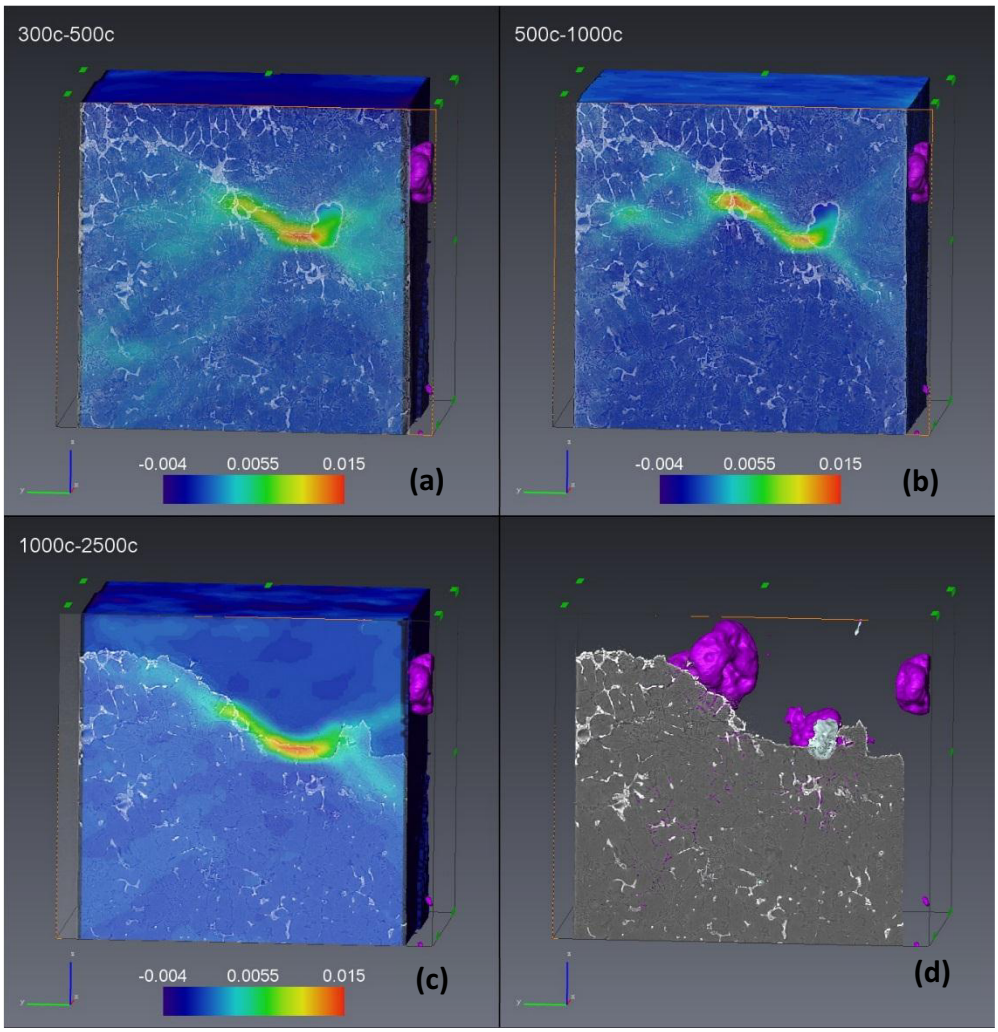

Figure 3. εzz strain field with the microstructure shown in transparency between (a) 300c-500c, (b) 500c- 1000c, (c) 1000c-2500c and (d) the fracture surface

The Finite Element results showed a large strain concentration at the pores cluster; where crack initiation was indeed observed. As a result, in the present case crack initiation were porosity driven while propagation was correlated with the presence of hard intermetallic phases.

4. Conclusions

The efficiency of the experimental protocol using laboratory and synchrotron tomography, FE simulation and 3D digital volume correlation to study the influence of the casting microstructure upon the mechanical properties of an Al-Si alloy has been proved. By prior screening the fatigue samples, it was to focus the X-ray tomography on a volume where cracks are likely to initiate. The synchrotron tomography permitted to increase the volume fraction of visible natural markers compared to laboratory tomography and thus allowed to enhance the spatial resolution and precision of the field measurements [8]. The DVC analysis of in-situ fatigue tests emphasized the relations between cracks, displacements discontinuities and strain localization in the measured fields. The results obtained at different steps of the fatigue cycles allowed the observation of crack

initiation close to the largest pores and of the crack propagation along the hard inclusions towards the free surface. The method illustrated here will now be systematically used to analyze the fatigue behavior of the 4 samples broken during the SLS fatigue experiment in order to make correlations between initiation sites and crack path and the local microstructural features. In a second step, similar fatigue test will be carried out at temperature around 200°C which are more representative of the service temperature of the cylinder heads.

5. Acknowledgments

The authors wish to thank the ANR (Agence Nationale de la Recherche) MatetPro project INDiANA for funding the study on Al-Si aluminum alloys. The SLS (Paul Scherrer Institute) is also acknowledged for providing beamtime on the TOMCAT beamline; Dr. Rajmund Mokso from SLS is particularly acknowledged for his help and advices with the Synchrotron tomography experiment.

6. References

1. Q.G. Wang, D. Apelian, D.A. Lados, "Fatigue behavior of A356-T6 aluminum cast alloys. Part I. Effect of casting defects," *Journal of Light Metals*, 1 (2001), 73-84.

2. X. Cao and J. Campbell, "The Nucleation of Fe-Rich Phases on oxide films in Al-11.5Si-0.4Mg cast alloys," *Metallurgical and Materials Transactions A*, 34 (7) (2003), 1409-1420.

3. S.Tabibian, E.Charkaluk, A.Constantinescu, F.Szmytkaa, A.Oudin, "TMF-LCF life assessment of a Lost Foam A319 aluminum alloy," *International Journal of Fatigue*, 53 (2013), 75-81.

4. J-Y. Buffière, S. Savelli, P.H. Jouneau, E. Maire, R. Fougères, "Experimental study of porosity and its relation to fatigue mechanisms of model Al–Si7–Mg0.3 cast Al alloys," *Materials Science and Engineering A*, 316 (2001), 115-126.

5. F.Marone, B.Münch, M.Stampanoni, "Fast reconstruction algorithm dealing with tomography artifacts," *Proceedings of SPIE-The International Society for Optical Engineering*, 7804 (2010).

6. J.Réthoré, N.Limodin, J-Y.Buffière, F.Hild, W.Ludwig, S.Roux, "Digital volume correlation analyses of synchrotron tomographic images," *Journal of Strain Analysis for Engineering Design*, 46 (2011), 683-695.

7. P.Cachier, E.Bardinet, D.Dormont, X.Pennec, N.Ayache. "Iconic feature based nonrigid registration: the PASHA algorithm." Computer Vision and Image Understanding, 89(2003) : 272 – 298, 2003. ISSN 1077-3142

8. N.Limodin, A.El Bartali, L.Wang, J.Lachambre, J-Y.Buffière, E.Charkaluk, "Application of X-ray microtomography to study the influence of the casting microstructure upon the tensile behaviour of an Al–Si alloy," *Nuclear Instruments and Methods in Physics Research Section B: Beam Interactions with Materials and Atoms*, in press.

New Experimental Techniques

2nd International Congress on 3D Materials Science
Edited by: Dominique Bernard, Jean-Yves Buffière, Tresa Pollock, Henning Friis Poulsen, Anthony Rollett, and Michael Uchic
TMS (The Minerals, Metals & Materials Society), 2014

DYNAMIC HIGH-TEMPERATURE MONITORING OF MICROWAVE ENERGY ABSORPTION AND HEATING OF MATERIALS WITH ULTRAFAST *IN SITU* SYNCHROTRON X-RAY TOMOGRAPHIC MICROSCOPY AND POWDER DIFFRACTION TECHNIQUES

Sebastien Vaucher[1], Rajmund Mokso[2], Kotaro Ishizaki[1], Manuela Stir[3], Radu Nicula[1]

[1]Empa - Swiss Federal Laboratories for Materials Science and Technology;
Feuerwerkerstrasse 39, CH-3602 Thun, Switzerland
[2]Swiss Light Source, Paul Scherrer Institut;
CH-5232 Villigen, Switzerland
[3]Dept. of Chemistry and Biochemistry, University of Berne;
Freiestrasse 3, CH-3012 Berne, Switzerland

Keywords: in-situ microwave heating experiments using synchrotron radiation; X-ray tomography; synchrotron radiation powder diffraction; microwave sintering

Abstract

In-situ time- and temperature-resolved synchrotron radiation techniques like ultrafast synchrotron X-ray tomographic microscopy and powder diffraction are unique tools for the dynamic characterization of materials processing by microwave heating. The absorption of microwave energy is typically a very fast process, with heating rates of the order of hundreds of degrees per second being no exception. The microwave energy absorption efficiency changes significantly with increasing temperature. Another unique feature of microwave heating is the intrinsic dielectric and/or magnetic selectivity, which often translates into the preferential deposition of microwave field energy only into specific specimen regions. For inhomogeneous materials in particular, complex patterns for the dynamic electromagnetic and temperature field distributions can be expected thus making the use of 3D monitoring methods not only meaningful but also necessary. We report on our recent progress with the *in-situ* characterization of microwave heating of metallic, ceramic and composite materials at very high heating rates. Experimental methods with subsecond temporal resolution, in particular high-temperature time-resolved X-ray scattering and time-resolved X-ray microtomography using synchrotron radiation, are discussed. Examples include microwave-assisted structural phase transitions and sintering in Al-alloys, foaming of construction materials, microwave processing of ceramics and composites.

Introduction

During the recent few years, the interest in using microwave fields for the solid-state synthesis and processing of complex materials increased dramatically [1-3]. In order to better understand and exploit the unique advantages of microwave heat processing, in situ neutron [4-6] as well as X-ray [7,8] small- and wide-angle diffraction experiments were performed in the past. At high-brilliance synchrotron radiation sources, time-resolved synchrotron radiation powder diffraction (SRPD) experiments with sub-second resolution could be performed in conjunction with in situ microwave heating of various materials, including metals and alloys [3,9-14]. Progress was also reported concerning the time-resolved investigation of microwave sintering processes by in situ synchrotron-based X-ray tomographic microscopy (SRXTM) [15,16]. We report on our recent results with the in-situ characterization of microwave heating of Al-alloys and polymer-matrix composites using SRPD and SRXTM techniques.

In-situ 3D monitoring of microwave heating of Al-Cu-Fe alloy powders by X-ray tomography using synchrotron radiation

The discovery that microwaves are able to heat metallic powders [17] resulted in a widespread interest in processing and sintering of particulate metals using microwave radiation. In spite of the growing experimental knowledge, the phenomenology of microwave heating of metals yet remains to be fully understood. Several models were developed [18-20] however for different scales and with different levels of complexity. For the case of microwave heating, finite-difference time-domain (FDTD) models exist that incorporate both electromagnetic and thermal models, allowing to account for convective and radiative losses, the power absorbed by the powder bead, as well as for the temperature dependence of the physical, thermal and dielectric properties of the material. However, solid-state diffusion processes (needed in the description of microwave sintering) are seldom taken into consideration. For conventional sintering, the individual contributions of the surface, grain-boundary and volume diffusion transport into sintering kinetics during the various stages of sintering can be estimated [21-23]. Moreover, for the case of spherical rigid particles, the 3D sintering problem can be reduced to a 2D mass transport problem if effective diffusion coefficients are introduced [23]. Microwave metal sintering models thus obviously benefit from experiments on nearly monosize spherical particles of well-characterized materials.
The SRXTM experiments were performed at the TOmographic Microscopy and Coherent rAdiology experimenTs (TOMCAT) beamline at the Swiss Light Source (SLS). Recently, the TOMCAT beamline [24] has established itself as a state-of-the art hard x-ray tomographic microscopy endstation for experiments ranging from the fields of biology to materials science. It routinely performs absorption as well as phase-contrast imaging with an isotropic voxel size in the sub-micron range. Typical acquisition times are on the order of a few minutes, depending on energy and resolution. In addition to further developments in phase-contrast imaging, scientific activities focus on pushing spatial and temporal resolution by orders of magnitude, aiming at nanoscale [25] and "real-time" [26] tomography. In the present *fast-tomography* experiments 701 views were accumulated (exposure time 225 ms, field of view 1.5 mm, voxel size 0.7 μm).

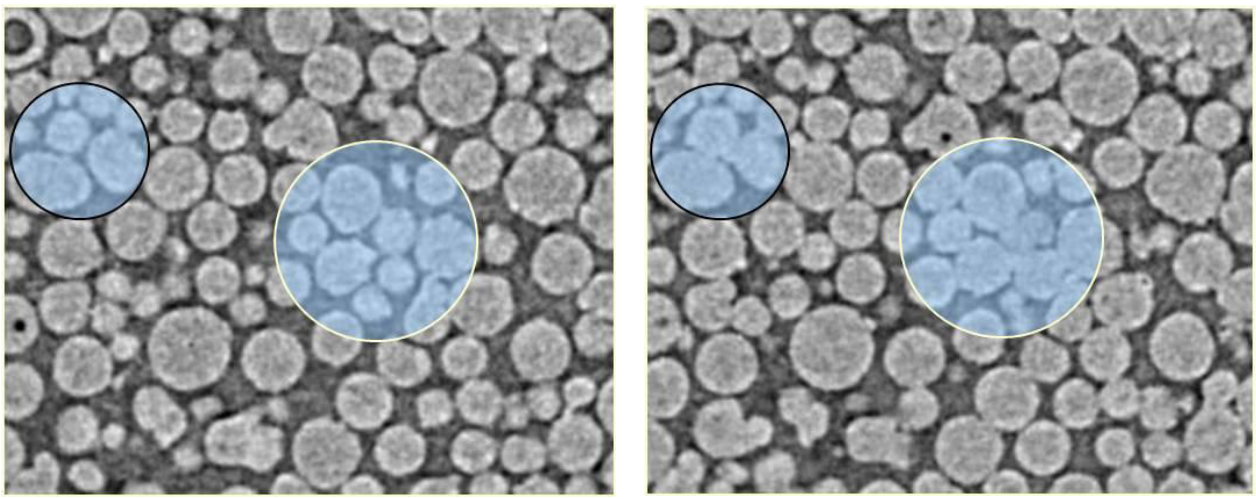

Figure 1. Multiparticle necking and coalescence events (see for ex. the blue regions) observed during microwave heating of $Al_{65}Cu_{23}Fe_{12}$ particles at 650°C. Particle sizes range from 25 to 45 microns. Left: initial state. Right: final state.

The *in-situ* microwave heating SRXTM experiments were performed on $Al_{65}Cu_{23}Fe_{12}$ (at.%) particles kindly provided by Prof. D. Sordelet (Ames Laboratory, Iowa State University, U.S.). For particles between 25 to 45 microns, microwave heating at approx. 650°C results in particle necking and coalescence (Fig. 1). Additional *in-situ* microwave heating SRXTM experiments were performed on larger (100 μm) spherical $Al_{65}Cu_{23}Fe_{12}$ particles (Fig. 2), for which the microwave absorption properties is expected to differ. In these experiments the alloy powders were exposed to higher temperatures, namely ranging from 700 to 870°C.

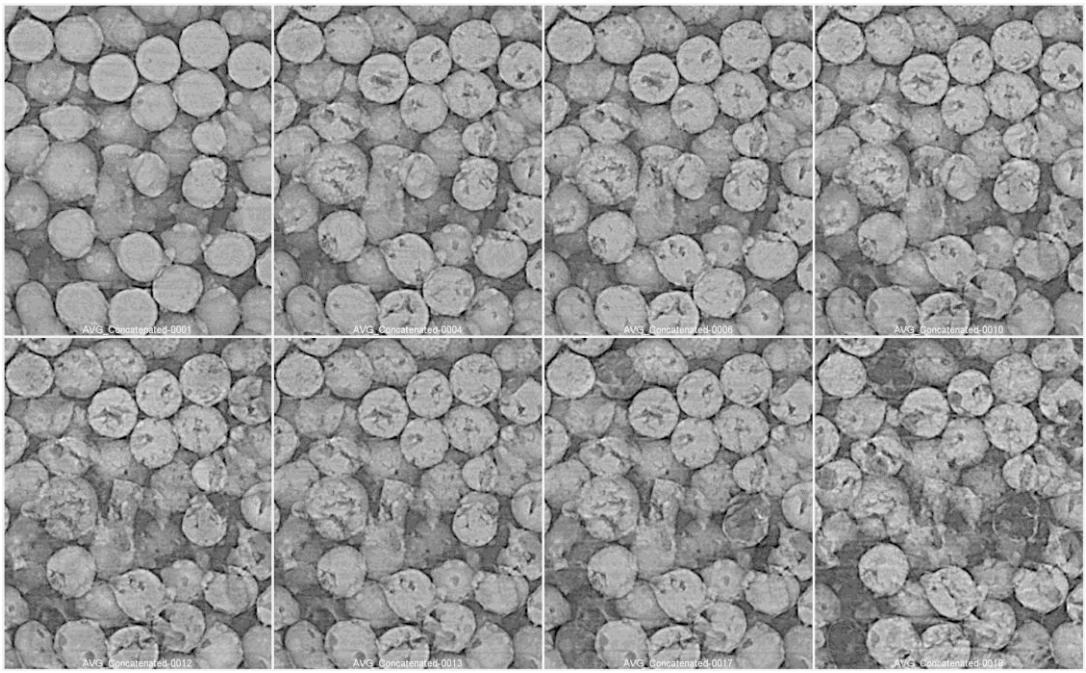

Figure 2. Time sequence of X-ray tomographic images (from left to right, top to bottom) collected on Al-Cu-Fe during microwave heating above 700°C. First and last images were taken at ambient temperature (see also Fig. 3).

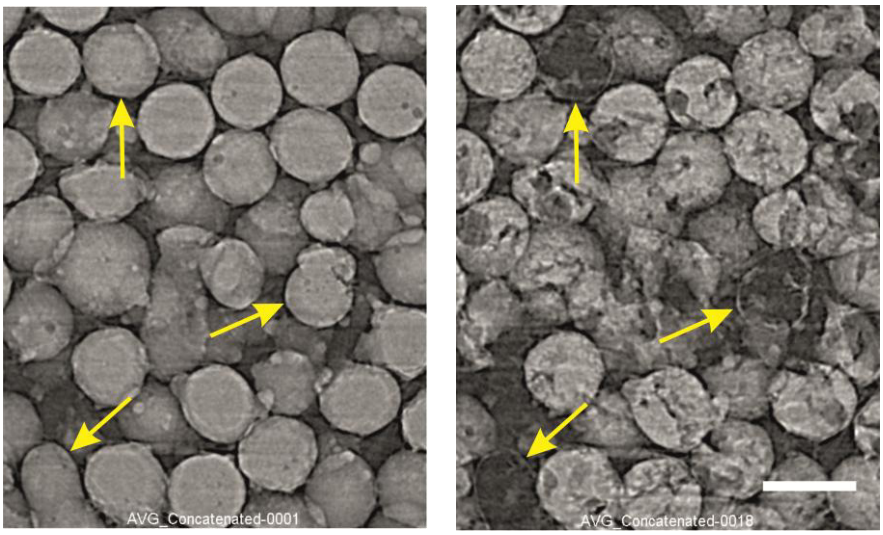

Figure 3. XTM images collected at room temperature before (left) and after the microwave treatment (white scale bar 100 microns). Arrows indicate metal particles that undergo full volumetric transformation, except at the surface.

Unusual microwave effects were observed for 100 µm alloy particles at temperatures above 700°C, namely a disruptive action of the microwave field leading to rapid changes of the particle inner structure and porosity, which nevertheless sometimes leaves the near-surface regions intact in size and shape (Fig. 3). Indeed, some particles seem to be emptied out through channels in the surface, with only shells retaining their initial shape upon cooling. An explanation of these microwave effects might involve e.g. structural phase transformations or partial melting, however this requires a more careful analysis (in progress).

<u>In-situ monitoring of selective microwave heating of metal particles in a polymer matrix by synchrotron radiation powder diffraction</u>

In particular for polymer-matrix composites, new opportunities for improved material properties are sought through the use of advanced powder processing technologies. For example in the field of biomaterials for acetabular cup prosthetics, ultra-high molecular weight polyethylene (UHMWPE) composites comprising Al-Cu-Fe quasicrystalline alloy particles were recently shown to exhibit significantly improved wear loss properties compared to pure UHMWPE, without compromising the excellent biocompatibility of the untreated UHMWPE matrix. Further improvement of the wear resistance of such composites is nowadays sought in the better anchoring of the metal particles to the polymer matrix. Towards this objective, a novel rapid thermal processing approach was explored that exploits the *selective* absorption of microwave field energy by the metal particle constituent of the composite material, with further advantages coming from the ultrafast volumetric microwave processing ability and the potential fine-control of the polyethylene (PE) regions solely-modified around the metal-particle inclusions, so as to preserve to a maximum extent the optimal biomechanic performance of the initial polymer. In this new approach, metallic Al particles act as local internal heaters that absorb the microwave energy, then release it as heat to a limited volume of the polymer matrix surroundings.

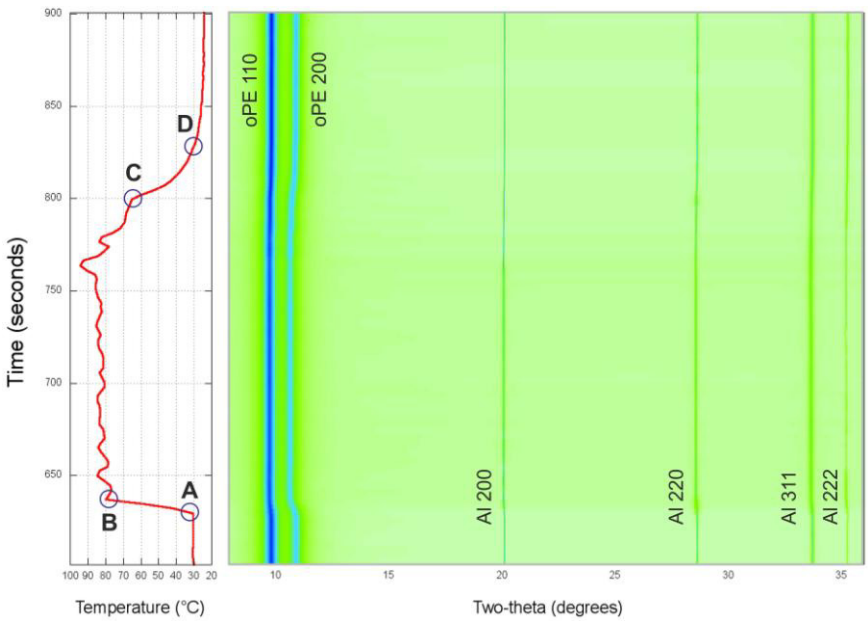

Figure 4. WAXS diffracted intensity map collected during the microwave heating of Al/UHMWPE composite at 2.45 GHz. The (110) and (200) X-ray diffraction lines of orthorhombic polyethylene are located at low 2θ scattering angles. The (200), (220), (311) and (222) diffraction lines of face centered cubic Al are also visible.

First results were obtained on microwave heating of model powder specimens of UHMWPE with various contents of pure aluminium (Fig. 4). The preferential heating of Al particles by the 2.45 GHz microwave E-field was monitored *in-situ* by simultaneous small- and wide-angle scattering SAXS/WAXS of synchrotron radiation. The experiments were performed at the MS X04 SA beamline at the SLS, using monochromatic synchrotron radiation (λ = 0.0708 nm) and Mythen II detectors. This state-of-the-art method may reveal the energy flow from the high-frequency electromagnetic field selectively to the UHMWPE-embedded metal particles and further to nearby polymer matrix regions by the *in-situ* monitoring of dynamic thermal expansion effects of the individual constituent phases. Since UHMWPE is a poor microwave absorber, the microwave heating of the polymer-metal composites is not granted a priori. Indeed, pure UHMWPE and low-Al content specimens could not be heated this way. It therefore appears that a minimum fraction of Al (less than 10%) is needed for the microwave coupling. The present results nevertheless demonstrate for the first time the feasibility of this novel microwave processing approach.

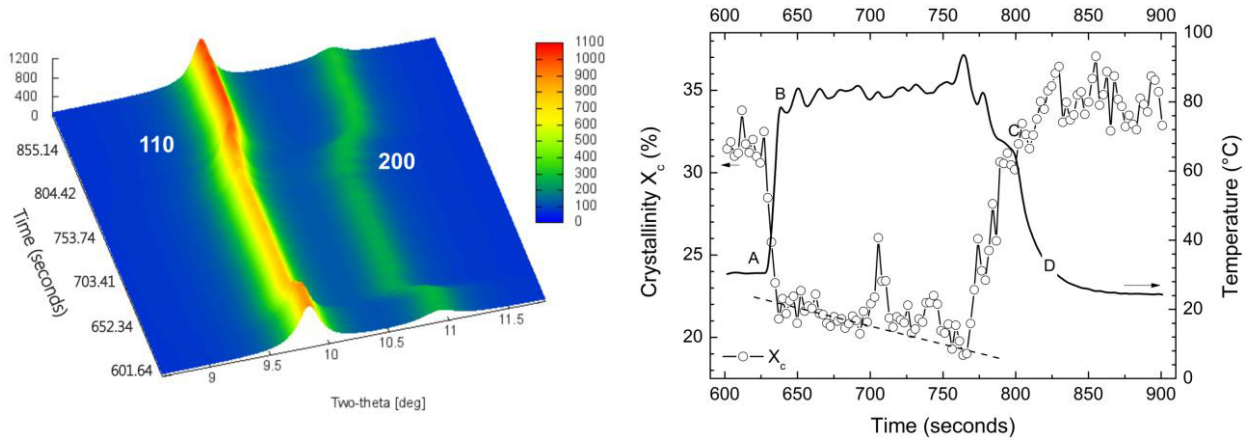

Figure 5. 3D X-ray intensity map showing the (110) and (200) diffraction lines of orthorhombic polyethylene (left). Notice the significant attenuation of the Bragg peak intensities during the 'isothermal' treatment at T ≈ 85°C (region B-C), which translates into a lower PE crystallinity (right). Upon cooling, the degree of crystallinity is improved by 3% compared to the initial state.

Indeed, microwave heating seems promising for promoting local structural modification of the initial orthorhombic polymer structure around the metal inserts via controlled thermal treatments below the melting point (Fig. 5). The crystallinity degree of PE was evaluated as the ratio of the Bragg diffracted intensity – comprising the (110) and (200) PE diffraction lines – and the total X-ray intensity both recorded within the same 2θ scattering angle range between 9 to 12 degrees (the total intensity includes an additional broad amorphous peak). The re-organization of UHMWPE chains during the quasi-isothermal treatment at 85°C favours a higher degree of PE crystallinity upon subsequent cooling (Fig. 5). This is expected to assist in better anchoring of the Al particles in the UHMWPE matrix.

Acknowledgements

The authors kindly acknowledge the teams at the TOMCAT and MS X04SA beamlines at the Swiss Light Source (PSI, Switzerland), as well as the team of Prof. J.M. Català-Civera at ITACA (University of Valencia, Spain). This work was jointly supported by the Swiss National Science

Foundation and by the German Science Foundation, project "*Calorimetry of phase transitions in ultrafast conventional and electromagnetic heating*", SNSF Grant 20PA21-129123 and DFG Grant SCHI331/21-1.

References

1. H.J. Kitchen et al, Chemical Reviews 114(2) (2014) 1170-1206.
2. R. Rosa, P. Veronesi, C. Leonelli, Chemical Engineering and Processing 71 (2013) 2-18.
3. S. Vaucher, R. Nicula, J.M. Català-Civera, B. Schmitt, B. Patterson, J. Mater. Res. 23 (2008) 170-175.
4. A.G. Whittaker, A. Harrison et al, Rev. Sci. Instrum. 72 (2001) 173.
5. A. Harrison, R. Ibberson, G. Robb, G. Whittaker, C. Wilson, D. Youngson, Faraday Discuss. 122 (2002) 363.
6. M.M. Günter et al, Z. Anorg, Allg. Chem. 631 (2005) 1277.
7. G.R. Robb, A. Harrison, A.G. Whittaker, Phys. Chem. Commun. 5 (2002) 135.
8. G.A. Tompsett et al, Rev. Sci. Instrum. 77 (2006) 124101.
9. R. Nicula, M. Stir, K. Ishizaki, J.M. Català-Civera, S. Vaucher, Scripta Materialia 60 (2009) 120-123.
10. R. Nicula, M. Stir, K. Ishizaki, J.M. Català-Civera, S. Vaucher, J. Phys. Conf. Ser. 144 (2009) 012109.
11. S. Vaucher, M. Stir, K. Ishizaki, J.M. Català-Civera, R. Nicula, Thermochim. Acta 522 (2011) 151.
12. R. Nicula, K. Ishizaki, M. Stir, Z. Shen, S. Vaucher, Philos. Mag. 91 (2011) 2450.
13. R. Nicula, M. Stir, A. Wurm, J.M. Català-Civera, K. Ishizaki, S. Vaucher, E. Zhuravlev, C. Schick, Thermochim. Acta 526 (2011) 137.
14. K. Ishizaki, M. Stir, F. Gozzo, J.M. Català-Civera, S. Vaucher, R. Nicula, Mater. Chem. Phys. 134 (2012) 1007-1012.
15. K. Ishizaki et al, Ceram. Trans. 209 (2010) 211-217.
16. F. Xu, Y. Li, X. Hu, Y. Niu, J. Zhao, Z. Zhang, Mater. Lett. 67 (2012) 162.
17. R. Roy, D.K. Agrawal, J.P. Cheng, S. Gedevanishvilli, Nature 399 (1999) 668-670.
18. Yu.V. Bykov, K.I. Rybakov, V.E. Semenov, J. Phys. D: Applied Physics 34 (2001) R55
19. P. Mishra, G. Sethi, A. Upadhyaya, Metall. Mater. Trans. B 37B (2006) 839
20. J. Luo et al, Appl. Phys. Lett. 84 (2004) 5076.
21 A. Vagnon et al, Acta Mater. 56(5) (2008) 1084-1093.
22. C.L. Martin, L.C.R. Schneider, L. Olmos, D. Bouvard, Scripta Materialia 55 (2006) 425.
23 A.L Maximenko, E Olevsky, Acta Mater 52 (2004) 2953.
24. M. Stampanoni et al, Proc. SPIE 6318 (2006) art. no. 63180M.
25. M. Stampanoni, R. Mokso et al, Phys. Rev. B 81(14) (2010) art. no. 140105.
26. R. Mokso, F. Marone, D. Haberthür, J.C. Schittny, G. Mikuljan, A. Isenegger, M. Stampanoni, AIP Conf. Proc. 1365 (2011) 38-41.

Analysis at the Nanoscale

2nd International Congress on 3D Materials Science
Edited by: Dominique Bernard, Jean-Yves Buffière, Tresa Pollock, Henning Friis Poulsen, Anthony Rollett, and Michael Uchic
TMS (The Minerals, Metals & Materials Society), 2014

ATOMIC SCALE AND 3D CHARACTERIZATION OF THE HETEROGENEOUSLY FORMED S (Al_2CuMg) PRECIPITATES AT DISLOCATIONS IN Al-Cu-Mg ALLOY

Zongqiang Feng[1,2], Yanqing Yang[1], Yanxia Chen[1]

[1] Shaanxi Materials Analysis and Research Centre, Northwestern Polytechnical University, Xi'an 710072, China
[2] College of Materials Science and Engineering, Chongqing University, Chongqing 400044, China

Keywords: Aluminum alloy, Precipitation, Dislocations, HRTEM, Electron tomography

Abstract

The variant distribution and three-dimensional (3D) configurations of the heterogeneously formed S (Al_2CuMg) precipitates at dislocations were studied by means of high resolution transmission electron microscopy (HRTEM) and high angle annular dark field scanning transmission electron microscopy (HAADF-STEM) tomography. The preferred S variant pair along dislocation was proved to be S1 & S4 or its counterparts, and the inherent characteristic of the crystal structure of the S phase, i.e. the symmetry of pentagonal subunit, was considered to be the fundamental factor determining the preference of variant pair. The obtained 3D reconstructions of the S precipitates formed at helical dislocations can clearly reveal both the morphology of individual S precipitates and the overall configuration of the S precipitates nucleated at these dislocations.

Introduction

Precipitation in Al-Cu-Mg alloys during artificial ageing can usually take place in either homogeneous or heterogeneous manner. In the case of homogeneous precipitation, the main strengthening phase S (Al_2CuMg) precipitates with needle/rod-like shapes uniformly nucleate in the Al matrix and mainly grows along its $[100]_S$ direction [1]. The orientation relationship (OR) between S precipitate and Al matrix is $[100]_S//[100]_{Al}$, $(001)_S//(012)_{Al}$, which has 12 equivalent variants and four of them, S1~S4, can be seen edge-on in $[100]_{Al}$ direction (Fig. 1) [1,3]. In the case of heterogeneous precipitation, the S precipitates can form at some intrinsic defects such as dislocations, grain boundaries as well as dispersoid/Al interfaces [4]. Specifically, the heterogeneous precipitation of S precipitates at dislocation shows many novel crystallographic and morphological features, hence attracts increasing research concern. By using conventional transmission electron microscopy (TEM), previous researchers have revealed the precipitation process, variant distribution and strengthening effect of S precipitates at dislocations [1,3-7]. To date, however, some major issues, such as the selection criterion for the favorable S variant pair at dislocation, and the spatial distribution characteristics of S precipitates along different morphologies of dislocations, are not yet fully

understood.

In this study, we applied high resolution transmission electron microscopy (HRTEM) and high angle annular dark field scanning transmission electron microscopy (HAADF-STEM) tomography to achieve atomic scale and three-dimensional (3D) characterization of the variant distribution of the heterogeneously formed S precipitates along dislocations, with an attempt to establish the selection rule for favorable variant pair from the crystallographic perspective.

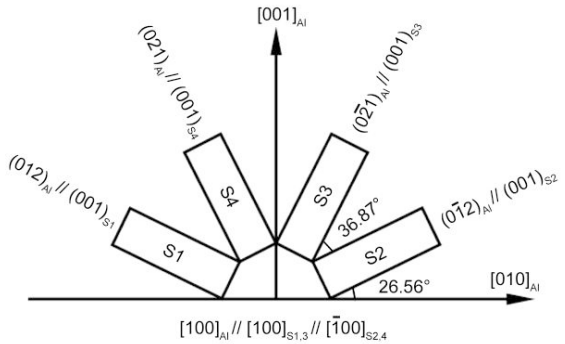

Fig. 1. Schematic illustration of four S variants observed from $[100]_{Al}$//$[100]_{S1,3}$//$[\bar{1}00]_{S2,4}$ direction (edge-on).

Experimental

An Al-4.2Cu-1.5Mg-0.6Mn-0.5Fe-0.5Si (wt%) alloy was solution-treated at 495℃ for 45 min, water quenched and then aged at 195℃ for 9h. Two states of the alloy, before and after ageing treatment, were focused on in the present research. Samples for TEM observation were prepared using twin-jet electropolishing in a 30% nitric acid and 70% methanol solution below -25℃ at 15V.

TEM observations were performed on a 300kV field emission TEM, Tecnai F30 G^2, equipped with a fully automated STEM tomography system. A single-tilt holder (Fischione model 2020) and the Xplore 3D software were employed to acquire several tilt series of HAADF-STEM images focusing on the S precipitates at dislocations from -70° to +70°, with an increment of 2° at low angle range (<50°) and of 1° at high angle range (>50°). The tomography data was aligned and reconstructed using Inspect 3D software. The 3D visualization was finally performed using AMIRA 5.2 software.

Results

Fig. 2a shows the microstructure of Al-Cu-Mg alloy after rapid quenching in water from solution temperature, which is characterized by uniformly distributed rod-like T ($Al_{20}Cu_2Mn_3$) dispersoids. Besides, lots of dislocations, especially helical dislocations, can be observed throughout the Al matrix. With further artificial ageing at 195℃ for 9h, high density of needle-like S precipitates aligning along $[001]_{Al}$ and $[010]_{Al}$ directions can be detected in Al matrix, and the helical dislocation lines seem much wider and clearer than their before-ageing state (Fig. 2b), indicating that the heterogeneous precipitation of the S phase has occurred along these dislocations.

Fig. 3 shows a representative HRTEM image of S precipitates at a helical dislocation

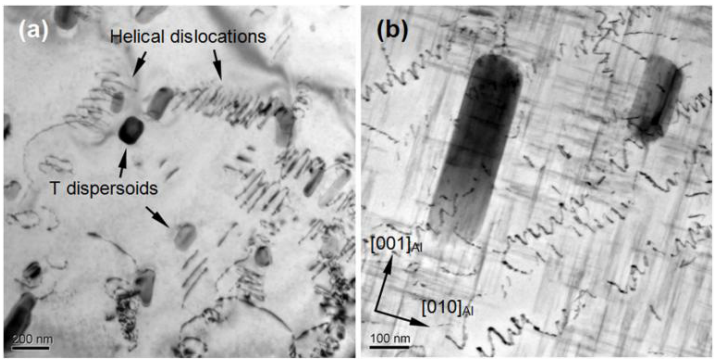

Fig. 2. TEM images showing the microstructure of Al-Cu-Mg alloy (a) before and (b) after artificial ageing at 195℃ for 9h.

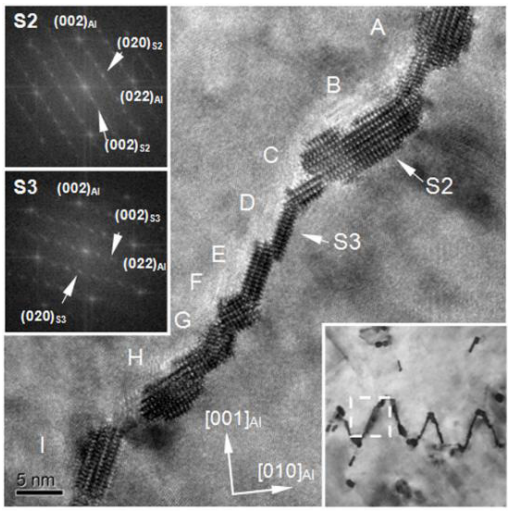

Fig. 3. HRTEM image corresponding to the rectangular region in the bottom-right inset, showing the distribution of S precipitates along a helical dislocation segment. S precipitates A, D, E, G and I belong to variant S3, while B, C, F and H belong to variant S2.

segment, corresponding to that within the rectangular region of the bottom-right inset. The S precipitates A~I, with different cross-sectional shapes but a common $[100]_S$ growth direction, arrange side by side along the original dislocation line. As indicated in the corresponding fast Fourier transformation (FFT) patterns, these precipitates belong to variant S2 or S3, and the only variant pair is S2 & S3.

To further reveal the spatial distribution characteristics from a 3D perspective, HAADF-STEM tomography was performed on several precipitate helices, both perfect and imperfect, to reveal the 3D configurations of the S precipitates along helical dislocations. In the tilt series of HAADF-STEM images of a perfect 'precipitate helix', we can see that the 'precipitate helix' seems like a bandolier-like wavy folded ribbon, in which the S precipitates line up parallel and side by side along the original helical dislocation line (Fig. 4a and 4b). Despite of a little extra diffraction contrast in some HAADF-STEM images, the wavy precipitate bandolier folds can still be seen remarkably in the corresponding 3D reconstruction. Nonetheless, the individual S precipitates can not be clearly distinguished (Fig. 4c), probably due to the poor contrast of such precipitate with a thickness of a few nanometers especially at high tilt angles. In the tilt series of HAADF-STEM images of an imperfect 'precipitate helix' (Fig. 4d and 4e) and the corresponding 3D reconstruction (Fig. 4f), separate S phase precipitates can be observed at several sites as labeled by arrows. All

these S precipitates show needle-like morphology and have a common elongation direction. Based on HRTEM observation (Fig. 3) and HAADF-STEM tomography, a schematic drawing showing the distribution of needle-/lath-like S precipitates along helical dislocations is illustrated in Fig. 4g.

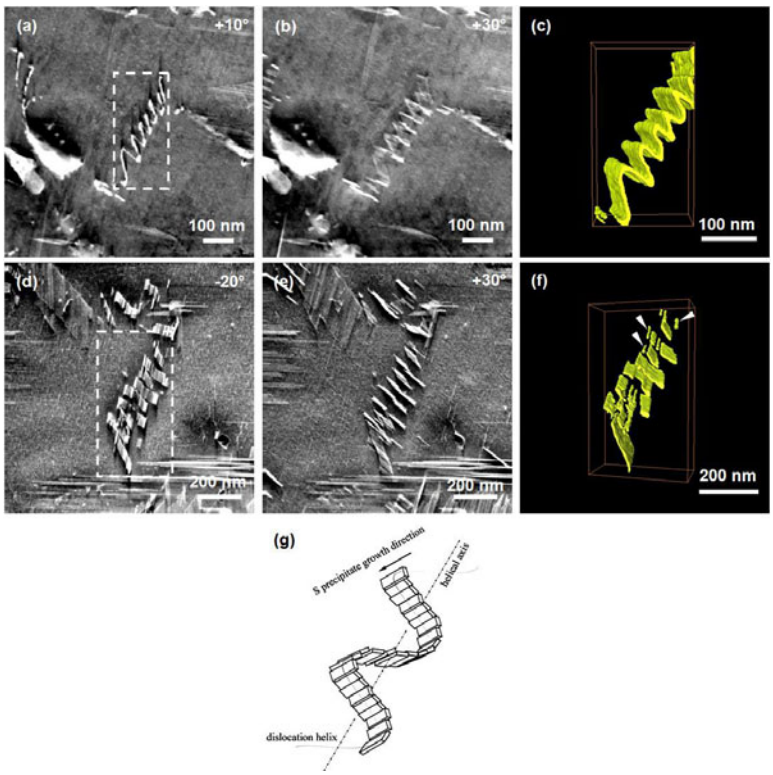

Fig. 4. Two tilt series of HAADF-STEM images and the corresponding 3D tomographic reconstructions showing the distribution of S precipitates along helical dislocations. (a,b) and (d,e) are representative HAADF-STEM images from the respective tilt series while (c) and (f) are tomographic reconstructions of the full dataset corresponding to the rectangular regions in (a) and (d). Note that the needle-like S precipitates all point in a $<100>_{Al}$ direction with the individual precipitates labeled by arrows. (g) Schematic illustration showing the distribution of S precipitates along helical dislocations.

Discussion

As representatively shown in Fig. 3, S precipitates along a dislocation line always have a common $[100]_S$ growth direction, and the only favorable variant pair is S2 & S3 or their counterpart S1 & S4, with relevant $(001)_S$ planes having a relative angular separation of 36.87° (Fig. 1). Such phenomenon has been proved by many previous investigations [2-4]. To elucidate why the variant pair of S2 & S3 or their counterpart S1 & S4 is the most favorable for S precipitates along dislocations, former researchers tried to relate the intrinsic characteristics of dislocation (line direction, Burgers vector) with those of precipitates (habit plane, maximum misfit vector) [2,3,8]. However, these selection criteria of variant pairs are still in dispute, mainly because neither the morphology or the Burger vector of the original dislocation on which the S precipitate forms can be observed or determined any more after long time elevated ageing and precipitate nucleation. In fact, the variant pair of S1 & S4 or their counterpart S2 & S3 is prefered not only for S precipitates along dislocations, but for

those at grain boundaries and phase interfaces [4]. Accordingly, the selection criterion for favorable variant pair of S precipitates needs to be revisited with consideration of the nucleation resistance and the inherent characteristic of the crystal structure of the S phase.

Generally, to form an energetically favorable variant pair, two conditions should be satisfied as much as possible: (i) each S variant keeps the classic OR and coherent interfaces with the Al matrix, i.e. $(001)_S//\{021\}_{Al}$, and (ii) S variants in the same pair share an interface with the lowest energy to utmostly reduce the nucleation resistance. Fig. 5 schematically illustrates the spatial distribution and crystal structure of three possible S variant pairs in $[100]_{Al}//[100]_{S1,3}//[\bar{1}00]_{S2,4}$ direction (edge-on view) according to the classic OR between S precipitate and Al matrix. Every S variant contains a 2×2 unit cell of the S phase. From the perspective of crystallography, when looking down the $[100]_S$ direction, several pentagonal subunits can be observed within the unit cell of the S phase (black line pentagons). The adjoining pentagons share the same edge and are centrosymmetrical about the center of the sharing edge. To our knowledge, regular pentagon always goes together with the 36° angle. The twinning operation to a regular pentagon is actually equivalent to a 36° rotation. As shown in Fig. 5a, for S1 and S4 (equivalent to S2 and S3) with classic OR with Al matrix, theoretically we can calculate that the angle between $(001)_{S1}$ and $(001)_{S4}$ is 36.87°, which is very close to the rotation angle required to form a twin of a regular pentagon. In this sense, S1 and S4 can be considered as twins. With a slight rotation (0.87°), the adjoining pentagonal subunits can share the same edge and form a coherent twin interface, which can significantly reduce the nucleation energy of the correlative S variants. However, for variant pair of S1 and S3 (equivalent to S2 and S4), to form such a coherent twin interface, at least a 18° rotation is required but the coherent relationship of $(001)_S//\{021\}_{Al}$ will be destroyed (Fig. 5b), indicating the nucleation resistance increases for S precipitates. The variant combination of S1 and S2 (equivalent to S3 and S4) is not common since a much larger rotation angle (54°) is necessary to make the adjacent pentagons edge-sharing and form a coherent twin interface (Fig. 5c), thus the nucleation resistance to form this variant pair of S precipitates will be even larger. In a word, the variant pair of S1 and S4 or their counterpart is energetically favorable, and the inherent characteristic of the crystal structure of the S phase, i.e. the symmetry of the

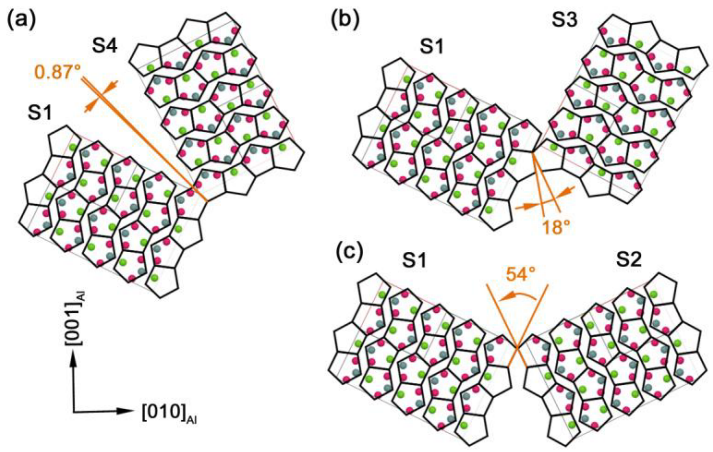

Fig. 5. Schematic illustration showing the spatial distribution and crystal structure of three possible S variant pairs in $[100]_{Al}//[100]_{S1,3}//[\bar{1}00]_{S2,4}$ direction. Every S variant contains a 2×2 unit cell of the S phase, and the black line pentagon outlines the subunits in the S phase structure. (a) S1 & S4; (b) S1 & S3; (c) S1 & S2.

pentagonal subunit, may be the fundamental factor determining the preference of variant pair.

With the help of HAADF-STEM tomography, we successfully obtained 3D reconstructions of the S precipitates along helical dislocations, in which both the wavy feature of these S precipitate groups and the needle-like morphology of an individual S precipitate can be clearly observed (Fig. 4c and 4f). This, together with the HRTEM observations, fully reveals the spatial distribution of the S variants along helical dislocation lines. HAADF-STEM tomography was proved to be a promising technique for studies of nanoscale precipitates, or their assembly, with complex morphology or configuration in metallic alloys.

Conclusions

HRTEM and HAADF-STEM tomography was applied to systematically investigate the variant distribution and 3D configurations of the heterogeneously formed S precipitates at dislocations in an Al-Cu-Mg alloy. The favorable S variant pair along dislocations was revealed and the underlying selection rule was discussed from the crystallographic perspective. In the 3D reconstruction of the S precipitates formed at helical dislocations, both the morphology of individual S precipitates and the overall configuration of the S precipitates nucleated at these dislocations can be clearly observed, which provided new evidence for variant distribution of S precipitates along dislocations.

Acknowledgements

Financial support from Excellent Doctorate Foundation of Northwestern Polytechnical University and the 111 Project (B08040) of China is gratefully acknowledged.

References

1. S.C. Wang and M.J. Starink, “Precipitates and intermetallic phases in precipitation hardening Al-Cu-Mg- Li alloy,” *International Materials Reviews*, 50 (2005),193-215.
2. R.N. Wilson and P.G. Partridge, “The nucleation and growth of S' precipitates in an aluminium-2.5% copper-1.2% magnesium alloy,” *Acta Metallurgica*, 13 (1965), 1321-1327.
3. Z.Q. Feng et al., “Variant selection and the strengthening effect of S precipitates at dislocations in Al-Cu-Mg alloy,” *Acta Materialia*, 59 (2011), 2412-2422.
4. Z.Q. Feng et al., “HRTEM and HAADF-STEM tomography investigation of the heterogeneously formed S (Al_2CuMg) precipitates in Al-Cu-Mg alloy,” *Philosophical Magazine*, 93 (2013), 1843-1858.
5. P. Ratchev et al., “Precipitation hardening of an Al-4.2wt% Mg-0.6wt% Cu alloy,” *Acta Materialia*, 46 (1998), 3523-3533.
6. A. Tolley, R. Ferragut and A. Somoza, “Microstructural characterisation of a commercial Al-Cu-Mg alloy combining transmission electron microscopy and positron annihilation spectroscop,” *Philosophical Magazine*, 89 (2009), 1095-1110.
7. Z.Q. Feng et al., “Precipitation process along dislocations in Al-Cu-Mg alloy during artificial aging,” *Materials Science and Engineering A*, 528 (2010), 706-714.
8. A. Kelly and R.B. Nicholson, “Precipitation hardening,” *Progress in Materials Science*, 10 (1963), 151-391.

2nd International Congress on 3D Materials Science
Edited by: Dominique Bernard, Jean-Yves Buffière, Tresa Pollock, Henning Friis Poulsen, Anthony Rollett, and Michael Uchic
TMS (The Minerals, Metals & Materials Society), 2014

METROLOGY OF THREE-DIMENSIONAL TECHNIQUES IN FOCUSED ION BEAM MICROSCOPY

H G Jones[1], K P Mingard[1], D C Cox[1,2], B Winiarski[3], A Gholinia[3]
[1] National Physical Laboratory, Hampton Road, Teddington, Middlesex, TW11 0LW, UK
[2] Advanced Technology Institute, University of Surrey, Guildford, Surrey, GU2 7XH, UK
[3] School of Materials, University of Manchester, Grosvenor Street, Manchester, M1 7HS, UK

Keywords: focused ion beam, 3D reconstruction, slice geometry

Abstract

The use of focused ion beam (FIB) microscopes to characterise the microstructure of materials in three dimensions, by reconstruction of serial sections, has rapidly grown during the last decade. This is due to improved capabilities in material characterisation and more effective control of the ion beam to cut cross sections in a wide range of materials. It is easy to assume that a visual reconstruction of a stack of images produced by FIB is a fairly accurate representation of the true 3D structure and subsequently carry out measurements based on these data. However, it will be shown that this is not straightforward and in practice, errors or uncertainties in the sectioning, imaging or mapping, and reconstruction can combine to produce misleading results. This paper discusses the metrological challenges faced, but often disregarded, in measurement of the errors and uncertainties that occur throughout FIB 3D characterisation of materials. This was done by studying image stacks and 3D reconstructions from purpose-made structures of known geometries and composition.

Introduction

In dual beam microscopes with ion and electron columns, electron images of the FIB milled cross sections are acquired, building a stack of image data. These images are reconstructed into a volume to recreate the milled away volume in three dimensions. Consecutive slice alignment in X and Y directions can be made either manually or using automated software routines. In the Z direction, correcting for the real slice thickness over the whole volume is much more challenging. The programmed slice thickness is commonly taken as the depth to be used with the XY pixel size to create the voxels in 3D reconstruction.

The use of the set slice thickness for Z ignores the possibility of errors in the actual slice thickness achieved. Inaccuracies could arise from errors in calibration, giving a constant error in all slices, or from variations between slices, caused by effects such as charging, beam heating, stage movements, or instabilities in the ion beam. Measurement of slice thickness can be difficult, even at the top surface; therefore slice thicknesses are often reported as a nominal value, taken as the programmed value eg: [1] or an average of total material removed eg: [2]. However in [3], extensive corrections were made to account for slice tilt and during 3D data acquisition and distortion in mapping, as well as fidicual lines on the top surface.

This paper describes the direct measurement of slice thickness variation and misalignments for the full depth the slices during FIB milling on artificial reference structures, and considers the accuracy and repeatability of measurements taken. The examples shown are for the case of standard image slice and view routines as supplied by the microscope manufacturer only to illustrate the measurement method, but are being translated to 3D EBSD geometry and 3D EDX and EBSD mapping in further work.

Experimental method

Fiducial lines to measure slice thickness

Full details of the slice thickness measurements using this technique are described in [4]. The principle of using diagonal fiducial lines is based on the geometry shown in Figure 1. When a slice of thickness *t* is milled away, the markers on the milled face are imaged. If the patterned lines are at 45° to the milled surface, the difference between the two x positions of the lines in two sequential images will equal the slice thickness (*b*-*a*). To check the parallelism and allow for measurement of drift, tramlines were milled perpendicular to the milled surface. This was done for the markers on each slice and averaged across the layer. Repeating this pattern over a multilayer stack enabled thickness measurements to be taken at different heights on the milled section, enabling more accurate measurement of the slice profile.

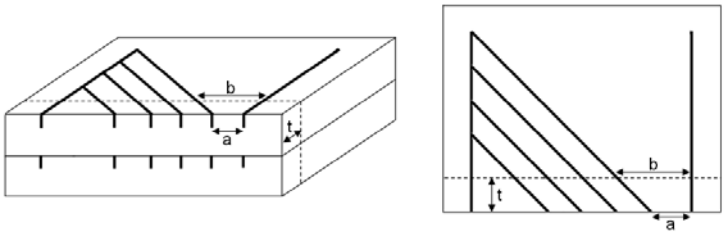

Figure 1: Diagram of the structure with fiducial lines, with markers in cross section.

To make the artefact, alternate layers of carbon and platinum approximately 14×14×1 μm in dimension were deposited on a silicon substrate. The fiducial lines were milled between each deposition. Figure 2 shows the initial flat face before the slices were carried out, showing the markers in cross section on each layer. For slicing, the stack in Figure 2 was milled using a 30 kV: 4 nA ion beam using the standard slice and view program (with no drift corrections) supplied with the microscope software. Slice thickness was set at 100 nm and the milling depth was 10 μm (for silicon), but a depth of ~15 μm was actually obtained. This depth was intentionally set to attempt to only just mill to the bottom of the stack, so that the full geometry of the slices could be studied. For reconstruction of real samples, a much larger depth should be milled and only the top few microns imaged; this means the acquired images are as flat as possible.

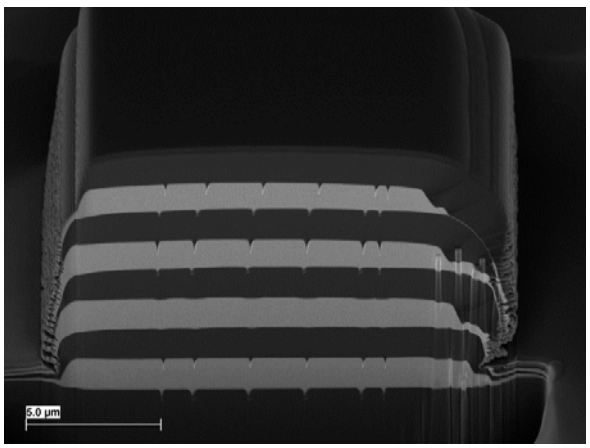

Figure 2: Cross section through stack and markers before slices were taken.

Secondary electron images were taken after each slice. The images were taken at 3 kV and corrected for specimen tilt to enable accurate vertical as well as horizontal measurements. At the magnification and resolution used this gave a pixel size of 7.19 nm.

Metallic spheres to measure distortions in reconstruction

A second structure was made using metallic powder copper and nickel spheres ranging between approximately 1 and 10 microns in size (Figure 3a) suspended in polystyrene (Figure 3b). This creates contrast between the two phases, which can be used for calibration of slice and view routines, with or without EDX mapping. Using spherical particles allows visualisation of any elongation in the reconstruction when using the assumed voxel size, due to real slice thickness variation, drift between slices, or effect of the interaction volume of the electron beam. Figure 3b shows an SEM image of a milled section through the sample. It can also be used in 3D EBSD routines, where only the spheres will be indexed. This will show distortion or drift in the EBSD maps due to slower map acquisition times and stage movements.

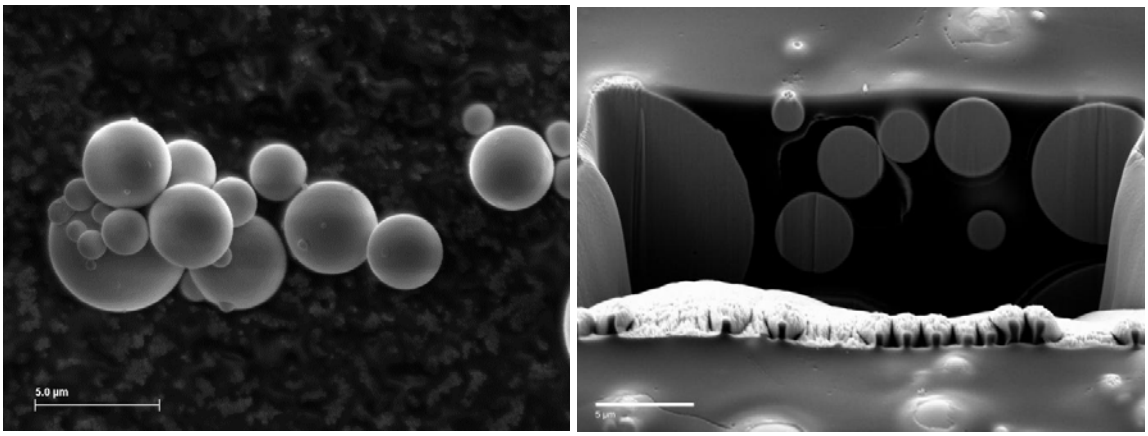

Figure 3: Secondary electron image of metallic spheres a) loose and b) in polystyrene matrix

A 30 kV: 2 nA ion beam current was used to mill slices at an arbitrary position in the bulk sample. Material was removed in front of the cross section before the sequential slicing commenced to avoid shadowing due to redeposition or sample geometry. SEM images of the slices were captured with an acceleration voltage of 3 kV, the slice thickness was 100 nm and the image pixel size was 16.9 nm.

Results and analysis

Slice thickness using fiducial lines

Figure 4a shows the results for the average slice thickness of the stack for slice and view. Not all the layers were measured, due to poor markers on some layers; layer 1 corresponds to the markers nearest to the top of the stack and layer 8 to those on the substrate.

The average slice thickness for each height was used to construct a slice by slice representation showing how the slices would appear if viewed from the side. Figure 5 shows that the initial few slices were relatively uniform and perpendicular to the top surface. However, it can be seen that the milling accelerates at the top, producing a significant taper from top to bottom. This is also observed in SEM images of the slices, where the milling

leaves an un-milled ledge at the bottom of the slice, which then is removed in the next slice. Subsequently, the milling proceeds in a relatively consistent manner, but the milled surface is always at a small angle to the perpendicular and the thickness variation of the bottom layer is greater than the upper layers but with the same general periodicity, reflecting the effect of dwell time on the amount of material milled at greater depths.

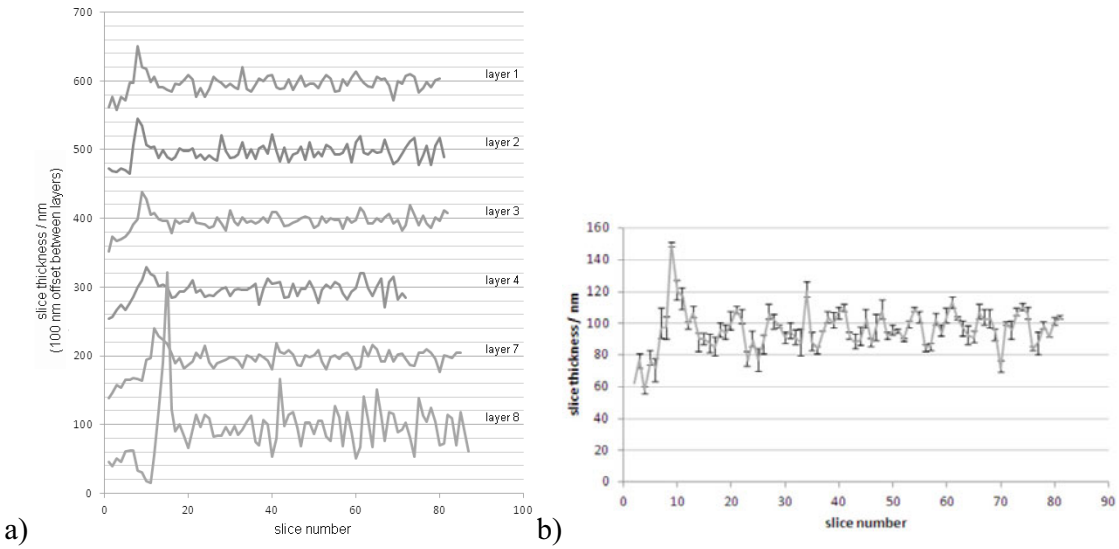

Figure 4: a) Average slice thickness at different heights on the stack during slice and view, b) slice thickness of a single layer with error bars showing measurement range for each slice.

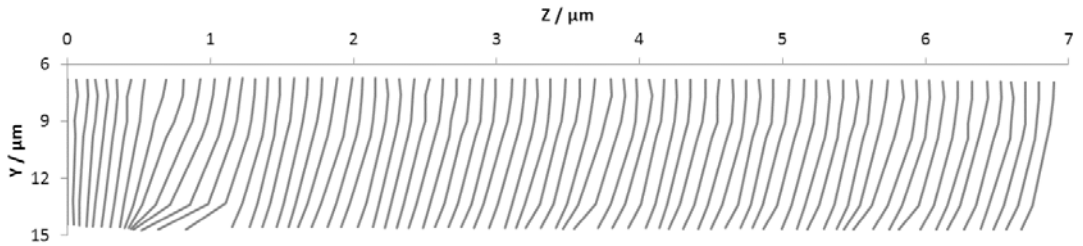

Figure 5: Side view of slices in milled stack (stretched in Z direction to show shape)

The maximum deviation of the average total slice thickness from the target of 100 nm was +50%/-43% at the top of the stack and +221%/-85% at the bottom. The variation was largest at the start of the run but even when the slice shape and thickness became more consistent later in the run, as shown in Figures 4 and 5, variation of up to 20% of the slice thickness was still present. Figure 4b shows that the measurement error for individual slices was much less than the overall slice thickness variation.

Distortions in reconstruction using spheres

Using the 100 nm slice thickness and 16.9 nm pixel size, secondary electron images were used to reconstruct the 3D volume of the metal powders in polystyrene. A number of slice registration routines were performed in Avizo Fire 6 software to attempt to align the slices. The resultant volume was cropped on each side to view the particular region shown in Figure 6. The axes are labelled such that the XY planes are the original image slices and the Z direction views the slices from the side.

The distortion of the sphere at the corner in the middle of Figure 6 shows the automated registration is still not correct. It shows there is still drift in the +Y direction, where the sphere appears to be pulled upwards. There is also some elongation in the +Z direction, implying the slice thickness was lower than the target value on average. The region circled in white on the XZ face is a pore in the polystyrene, causing brighter contrast.

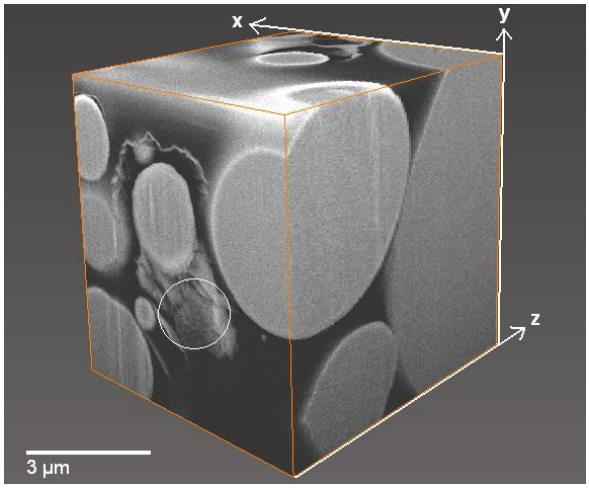

Figure 6: Reconstruction of images from routine with spheres sample (cube side approximately 10 µm)

Discussion

In the fiducial marker method, confidence that the measurement produces realistic values is seen in Figure 4b where there is excellent agreement between the four slice thickness measurements across the width of each slice; therefore the measurement range averages 1.1 pixels, or 8 nm. This is much less than the slice to slice variation, which even after the initial 20 slices varied by up to 5 pixels.

From top to bottom of the stack there is a consistent variation with the deviation from the vertical, increasing towards the base of the stack after the first few slices. This type (but not necessarily magnitude) of profile or taper is expected and is due to the effects of significant beam tails from the Gaussian beam profile. For the majority of the milling process, the overall taper from top to bottom of the measured stack is approximately 300 nm or 2.5°, but the geometry and depth of focus of the SEM means this taper is not visible in the images.

A possible explanation for the cause of the initial transient and continued slice thickness variation is that initially there may be a build-up of positive charge from the Ga ion beam on the sample; Ga ions are implanted, which will initially deflect the beam from the milled surface. Eventually the electron imaging occurring between milling and charge leakage from the milled region will reduce the positive charge build up and lead to a steady state. Arguing against this, is that similar behaviour to the reduced milling at the base followed by a rapid removal has been observed to repeat itself [4].

Conclusion

The use of fiducial lines milled in layers with high contrast between them enables measurement of individual slice thicknesses during a sequential “slice and view” operation in

focused ion beam microscopes. The imaging pixel size and resolution must be chosen to be sufficiently small relative to the slice thickness. By making a 3D artificial structure of fiducial lines it is possible to reconstruct the actual slice profile from measurements of the thickness across the width of the stack.

The slice thickness variation in this study, even under relatively stable conditions close to the top of the stack, was up to 20% from the target, except at the base of the stack where it was even greater, at up to 60%. The largest variation was seen in the first 20 slices, where a large taper was introduced and persisted throughout the milling sequence with an overall slope from the vertical of about 2.5°. Reasons for the variation of thickness and the change in geometry of the taper are unclear. It is possible that charging of the sample by the ion beam causes deflection of the ion beam until a charge balance is established.

Finally it is apparent that great care needs to be applied to any results carried out with 3D reconstructions of FIB produced image stacks, and that effort should be made to state likely errors associated with these types of operations. A simple surface fiducial marking system should be employed as a minimum as it is clear that without such a system the errors can be both large and undeterminable, and only the very top part of a milled surface should be used for the reconstruction to minimise the effect of taper in the region of interest.

This slice thickness uncertainty is confirmed in the spheres reconstruction, where the spherical particles appear slightly stretched in the Z direction of the assembled volume. It should also be noted that drift corrections and slice registration is not trivial, and alignment issues, if not done correctly, also contribute to distortion of the structure. This may not be as noticeable in real samples, such as steel or other metallic alloys, with more irregular or less well defined grain boundaries; therefore any artificial distortions cannot necessarily be detected. Using the spheres as a calibration or illustrative sample means that at least the most obvious errors can be identified beforehand and this knowledge applied to the procedure with real structures.

Further work to follow is 3D EDX of the spheres structure to measure distortions due to interaction volume and noise, and 3D EBSD of the layered structure to measure the slice thickness and the spheres to measure distortions in EBSD mapping and stage movements.

Acknowledgements

Thanks to the National Measurement System (NMS), a programme within the Department of Business Innovation and Skills (BIS), for their financial support of the project.

References

1. J. S. Earl et al. "Characterization of dentine structure in three dimensions using FIB-SEM," *Journal of Microscopy*, 240 (2010), 1-5
2. A. Gholinia, Presentation at Royal Microscopy Society Meeting, Derby, UK, 2010
3. P.A. Shade et al. "Experimental measurement of surface strains and local lattice rotations combined with 3D microstructure reconstruction from deformed polycrystalline ensembles at the micro-scale," *Integrating Materials and Manufacturing Innovation*, 2013, 2:5
4. H. G. Jones, K. P. Mingard and D. C. Cox. "Investigation of slice thickness and shape milled by a focused ion beam for three-dimensional reconstruction of microstructures," *Ultramicroscopy*, 139 (2014), 20-28

Dynamic Processes

2nd International Congress on 3D Materials Science
Edited by: Dominique Bernard, Jean-Yves Buffière, Tresa Pollock, Henning Friis Poulsen, Anthony Rollett, and Michael Uchic
TMS (The Minerals, Metals & Materials Society), 2014

HOW MUCH DOES AN INDIVIDUAL GRAIN BOUNDARY JUNCTION TELL US ABOUT THE GROWTH KINETICS OF ITS POLYCRYSTALLINE MICROSTRUCTURE?

Dana Zöllner, Peter Streitenberger

Otto von Guericke University Magdeburg, 39106 Magdeburg, Germany

Keywords: grain growth, boundary junctions, individual growth kinetics, analytic theory, Potts model simulation.

Abstract

In the present work we analyze the growth history of individual grains and grain boundary junctions. Based on a mean-field theory this enables us to calculate from stochastic fluctuations of individual junctions during grain growth the average growth law of the ensemble of grains, which we find to be in very good agreement with the growth law simulated by the Monte Carlo Potts model.

Introduction

It is well-known that the temporal evolution of a polycrystalline microstructure of a three dimensional bulk material during curvature driven grain growth (compare Fig. 1a) can be characterized by a parabolic growth law, where the average size $\langle R \rangle$ of all grains of the polycrystal increases with time t according to

$$\langle R \rangle^{1/n} - \langle R \rangle_0^{1/n} = b \cdot t \,. \tag{1}$$

Here the grain size R is defined as the radius of a grain volume equivalent sphere and the growth factor is given by b. The growth exponent n has a theoretical value of 0.5 (see, e.g., [1, 2] and the literature within). It can be shown that three-dimensional grain microstructures simulated by the Monte Carlo Potts model follow this theoretical prediction after an initial period of time very well yielding a growth exponent of nearly exactly 0.5 and a growth factor of b = 0.2417 MCU^2/MCS as it is shown in Figure 1b. Details on the actual implementation of the simulation can be found in, e.g., [3].
On the other hand, grain growth is first and foremost a consequence of the migration of individual grain boundaries and their junctions. In recent years new experimental techniques, such as high voltage transmission electron microscopy, hot stage microscopy in a scanning electron microscope and 3D X-ray diffraction [4, 5] permit a direct measurement of the growth kinetics of individual grains in situ during recrystallization and grain growth revealing, in particular, also the stochastic nature of the motion of triple and quadruple grain junctions.

In the present paper, we show that the stochastic motion of individual boundary junctions can be linked to the average growth law of the ensemble of grains, which opens up not only a further possibility to test stochastic formulations of grain growth but also a new way to determine the average growth law solely from the measurement of the stochastic behavior of individual grains.

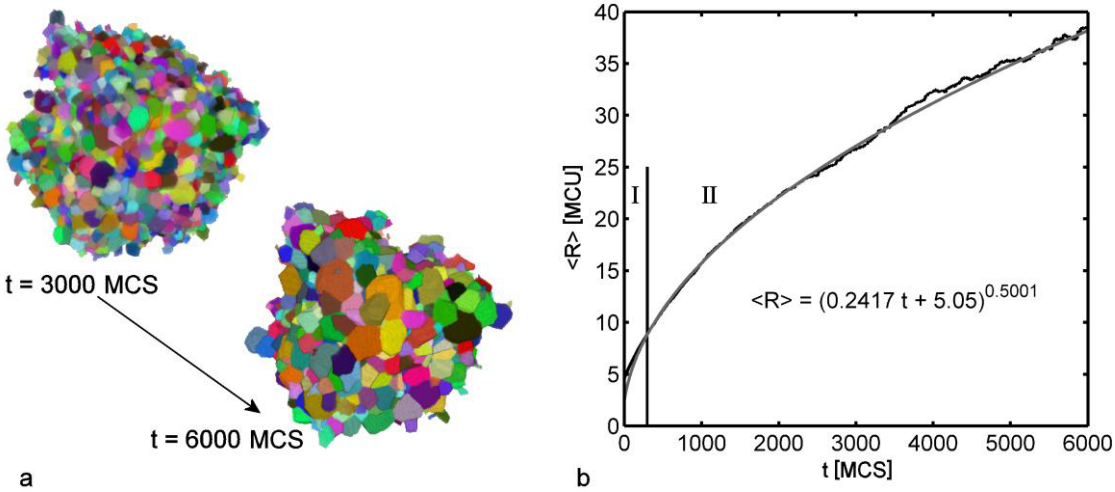

Figure 1. a – Image sequence of the coarsening of a simulated grain microstructure; b – Average growth law: simulation results (black) showing initial period (I) and quasi-stationary regime (II) for long time annealing together with analytic fit of Eq. (1) (grey curve).

Growth history of individual grains

Basically, grain growth is driven by one principle: while the mean grain size increases according to Eq. (1), small grains of an ensemble shrink and large grains grow. For a more quantitative analysis we can use the self-similar growth rate $R\dot{R}(x = R/\langle R\rangle)$ as described by [2]

$$R\dot{R}(x) = \gamma \cdot x \cdot \left(-\frac{3}{a(x_0)} \cdot \frac{(x_0 - x)^2}{x} + x \right), \tag{2}$$

where γ is a growth constant, x_0 is a free size parameter in correspondence with the Lifshitz-Slyozov stability conditions (cf. [1, 2]), the parameter $a = a(x_0)$ is defined implicitly [2].

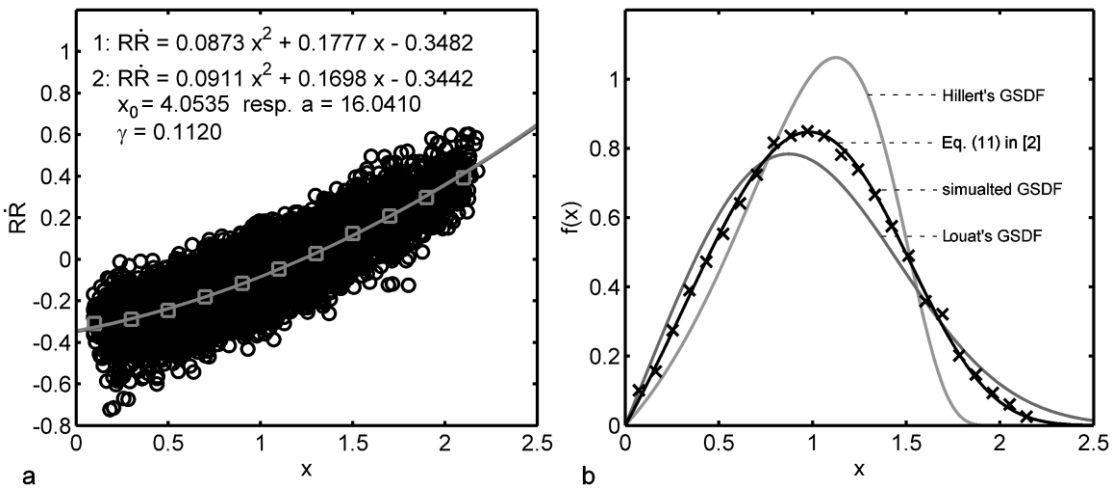

Figure 2. a – Simulated self-similar growth rate (circles: all data; squares: data divided into size classes) with quadratic least-squares fit (light grey curve no. 1) and fit of Eq. (2) (dark grey curve

no. 2); b – Simulated grain size distribution (crosses) together with analytic solutions from Hillert, Louat and Zöllner and Streitenberger (compare, e.g., [1, 2] and the references within).
The Potts Model simulation shows that the analytic function Eq. (2) (dark grey curve no. 2 in Fig. 2a) is just as good as a direct least-squares fit of a quadratic function to the simulation data (light grey curve no. 1 in Fig. 2a). However, Eq. (2) has the advantage that it yields values for γ, x_0, and a that can be used in further theoretical considerations enabling, e.g., to calculate an analytic grain size distribution ([2, 3], see also Fig. 2b) that is in very good agreement with the simulation results, which are in clear contradiction to Hillert's (light grey curve) and Louat's (dark grey curve) classical solutions.

In a previous work the authors derived an analytic expression describing the growth kinetics of individual grains by a parametric representation of the relation between grain size and time [6]:

$$R(x,x_i) = \langle R\rangle_0 \cdot x \cdot \sqrt{\tau(x,x_i)+1} \tag{3a}$$

$$t(x,x_i) = \frac{\langle R\rangle_0^2}{2\gamma} \cdot \tau(x,x_i) + t_0 \tag{3b}$$

$$\tau(x,x_i) = \left(\frac{x_0 - x_i}{x_0 - x}\right)^{2a/3} \cdot \exp\left(\frac{2a}{3}\frac{x_0(x_i - x)}{(x_0 - x_i)(x_0 - x)}\right) - 1. \tag{3c}$$

$x_i = R_i / \langle R\rangle_0$ is the initial relative grain size of each considered grain i at the chosen initial time.

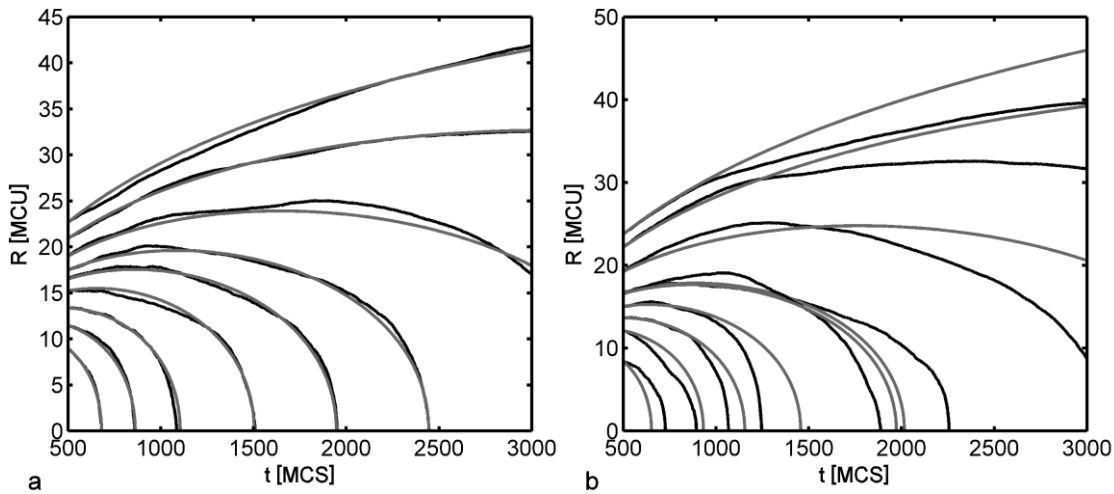

Figure 3. Temporal development of the grain size for simulation data (black) and parametric representation (grey): a – randomly selected grains that are well represented by Eqs. (3) for long times; b – grains that show only poor long-time agreement with Eqs. (3).

For the Potts model simulation of normal grain growth we find at t_0 = 500 that $\langle R\rangle_0 = 11.2109$ and from a least-squares fit of the growth law Eq. (2) to the simulation data it follows x_0 = 4.0535, a = 16.0410 and γ = 0.1120 (Fig. 2a). Hence, according to Eqs. (3), for each grain of given initial size $x_i(t_0 = 500)$ its growth history can be predicted, which is shown for 18 randomly selected grains in Figure 3. While in Fig. 3a the simulation data (black) are in very good agreement with the analytical functions (grey) for all times, the grains in Fig. 3b are represented correctly by Eqs. (3) only for short time spans showing deviating long-time behavior. These deviations are related to the scatter evident in Fig. 2a, which are related to the variations in the environment of each grain.

Growth history of individual boundary junctions

Sudden variations in the environment of a grain caused by rearrangement events are reflected by a stochastic motion of individual grain features leading to a diffusion-like behavior of evolving grains [7]. This is demonstrated on the examples of triple and quadruple junctions of a three-dimensional polycrystal that can be monitored easily during simulation of the coarsening. In Figure 4a the location of a triple junction in a 2D section as it changes with time is shown. The same highly discontinuous motion can also be found by in-situ real-time SEM observations as has been shown in Fig. 8 of [4] (compare also [5] page 505, [6, 8]). Figure 4b shows the temporal development of the three-dimensional coordinates of two associated quadruple points (marked by circles and squares, respectively) joined by a triple line plotted in projections.

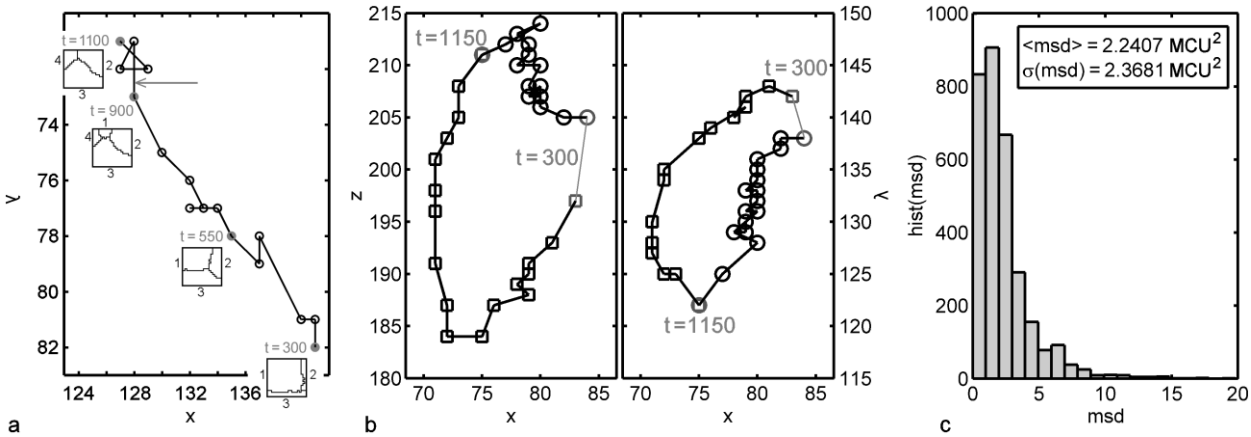

Figure 4. a – Location of a triple junction in a 2D section changing with time; b – Motion of two quadruple points (circles and squares) connected by a triple line showing x-z-coordinates (left) and x-y-coordinates (right); c – Distribution of mean square displacement for all quadruple junctions of the microstructure calculated after 50 time steps.

Considering the quadruple junction motion in Figure 4b as a type of Brownian-like motion, the diffusivity-like stochastic parameter D of this random walk process can be calculated from the measurement of the mean square displacement msd according to Einstein's equation [9]

$$D = \frac{msd}{6 \cdot \Delta t} = \frac{1}{3} \sum_{i=1}^{3} \frac{\langle \left(l_i - \bar{l}_i \right)^2 \rangle}{2 \cdot \Delta t}, \tag{4}$$

where l_i with $i = 1, 2, 3$ are the coordinates of the quadruple junctions and $\Delta t = t - t_0$.
The distribution of the mean square displacement msd for all grains at t_0 = 500 MCS for $\Delta t = 50\,\mathrm{MCS}$ is shown in Figure 4c, where the majority of the values lie between zero and approximately seven yielding an average value of $\langle msd \rangle = 2.2407\,\mathrm{MCU}^2$. Hence, the diffusivity follows from Eq. (4) to D = 0.007469 MCU^2/MCS.

Linking diffusivity and average growth rate

According to the stochastic treatments of grain growth in Refs. [7, 10, 11] the diffusivity should be related to the average growth law Eq. (1), in particular, to its growth parameter b, because

both the smooth mean-field part and the stochastic part of the grain evolution equation contribute to the grain size distribution. Although b has also the dimension of diffusivity, both quantities D and b differ numerically—as shown by the Potts model simulation with D = 0.007469 MCU^2/MCS (Fig. 4c) and b = 0.2417 MCU^2/MCS (Fig. 1b)—by more than an order of magnitude. In the following we derive a relationship between b and D by applying the Einstein relation Eq. (4) of individual stochastic grain motion in an analogue manner to the statistical coarsening process of the whole grain ensemble (cf. Fig. 5a). We assume that the deviation of the time development of individual grains from that of an average grain can be approximated as a three-dimensional stochastic process in real space, which is characterized by the same diffusivity as in Eq. (4). This implies that the average difference between the individual grain size R and the average size $\langle R\rangle$ at time t can be described by the mean square deviation

$$\langle R^2\rangle - \langle R\rangle^2 = 6D\cdot t\,, \tag{5}$$

where the diffusivity D is the same as determined by Eq. (4) from grain boundary motion. The average values in Eq. (5) are defined by

$$\langle R^n\rangle = \int R^n F(R,t)\mathrm{d}R \Big/ \int F(R,t)\mathrm{d}R\,. \tag{6}$$

With $R = x\langle R\rangle$, $F(R,t) = g(t)f(x)$ and $\langle R\rangle^2 = bt$ according to Eq. (1) for long-time annealing we obtain the following relationship between the growth rate b and the diffusivity D [6],

$$b = \frac{6}{\langle x^2\rangle - 1} D = \frac{6}{\sigma^2} D\,, \tag{7}$$

where $\langle x^2\rangle = \int_0^\infty x^2 f(x)\mathrm{d}x$ is the second moment of the normalized scaled grain size distribution $f(x)$ and $\sigma = \sqrt{\langle x^2\rangle - \langle x\rangle^2} = \sqrt{\langle x^2\rangle - 1}$ is its standard deviation.
Eq. (7) is verified by using the second moment of the simulated grain size distribution $f(x)$ in Fig. 2b, $\langle x^2\rangle = 1.1856$, yielding the standard deviation $\sigma = 0.4309$. Together with D = 0.007469 MCU^2/MCS as calculated from the stochastic motion of individual quadruple junctions (cf. Eq. (4) and Fig. 4c) Eq. (7) yields for the average growth rate b = 0.2414 MCU^2/MCS. This value is quasi identical compared to the b-value of the simulation (Fig. 1b: b = 0.2417 MCU^2/MCS) yielding a perfect agreement between simulation and theory!

If we consider according to [10, 11] three-dimensional grain growth as a stochastic process in the reduced one-dimensional parameter space of grain size R Eq. (5) corresponds a Gaussian random walk with drift, where the mean-square deviation is given by $\langle R^2\rangle - \langle R\rangle^2 = 2D_{eff}\cdot t$ with an effective diffusivity D_{eff} = 3D. This approximation is well confirmed by comparison of the corresponding one-dimensional scaled Gaussian grain size distribution [9]

$$f(x) = \frac{1}{\sqrt{2\pi}\sigma}\cdot\exp\left(-\frac{(x-1)^2}{2\sigma^2}\right). \tag{8}$$

with the simulation results as shown in Fig. 2b for $\sigma = \sqrt{2D_{eff}/b} = 0.4309$ from Eq. (7) with $D_{eff} = 3D = 0.022407$ MCU^2/MCS (compare Fig. 5b). Eq. (8) is normalized to one, fulfills the scaling requirement $\langle x \rangle = 1$ (cf. [1, 2]) and has the second moment $\langle x^2 \rangle = 1 + \sigma^2$.

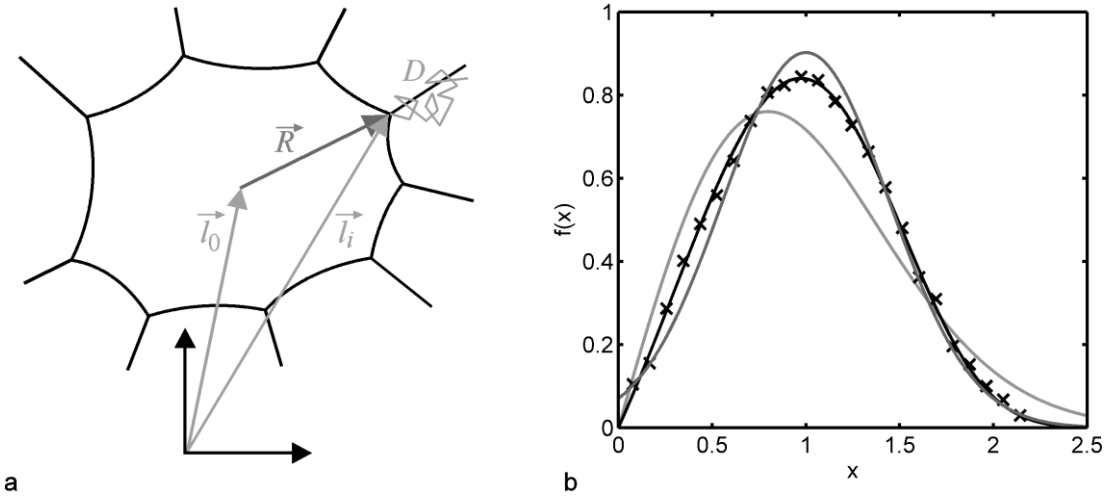

Figure 5. a – Scheme of a grain with junction motion; b – Grain size distribution (crosses: simulation data; black curve: least-squares fit of Eq. (11) in [2]; dark grey curve: Gaussian distribution Eq. (8); light grey curve: Louat's grain size distribution [10]).

Conclusions

In the present paper the growth history of individual grains and the stochastic motion of boundary junctions have been analyzed by means of Monte Carlo Potts model simulations and analytical results. A relationship between the average grain growth rate and the diffusivity of stochastic boundary junction motion was established and numerically verified.

References

[1] W.W. Mullins: Acta Mater. 46 (1998) 6219.

[2] D. Zöllner, P. Streitenberger: Scripta Mater. 54 (2006) 1697.

[3] D. Zöllner: Monte Carlo Potts model simulation and statistical mean-field theory of normal grain growth, Shaker Verlag Aachen, 2006.

[4] I.M. Fielden: Mater. Sci. Forum 467-470 (2004) 875.

[5] N. Hansen, D. Juul Jensen, S.F. Nielsen, H.F. Poulsen, B. Ralph (Eds.): Challenges in materials science and possibilities in 3D and 4D characterization techniques, Risø DTU National Laboratory for sustainable energy, 2010.

[6] D. Zöllner, P. Streitenberger, I. Fielden: Pract. Metallogr. 49 (2012) 7.

[7] K. Barmak, E. Eggeling, M. Emelianenko, Y. Epshteyn, D. Kinderlehrer, R. Sharp, S. Ta'asan: Phys. Rev. B 83 (2011) 134117.

[8] D. Zöllner, P. Streitenberger: Mater. Sci. Forum 715-716 (2012) 877.

[9] N.G. van Kampen: Stochastic processes in physics and chemistry, North-Holland, 1992.

[10] N.P. Louat: Acta Metall. 22 (1974) 721.

[11] C.S. Pande, G.B. McFadden: Acta Mater. 58 (2010) 1037.

AUTHOR INDEX
2nd International Congress on 3D Materials Science 2014

T

U

V

W

Y

Z

SUBJECT INDEX
2nd International Congress on 3D Materials Science 2014

X